ANALYSIS AND DESIGN OF COLD-FORMED THIN-WALLED ROOF SYSTEMS

PhD Dissertation

ATTILA LÁSZLÓ JOÓ

Budapest University of Technology and Economics

Supervisor:

László DUNAI, PhD

Professor

Budapest University of Technology and Economics

Budapest, 2009

CONTENTS

Acknowledgement

The research work is conducted in the framework of the following projects and co-operations:

- OTKA T049305 project of the Hungarian Scientific Research Fund, supervisor: Dr. László Dunai,
- OTKA K62970 project of the Hungarian Scientific Research Fund, supervisor: Dr. Sándor Ádány,
- TÉT PORT-5/2005 (OMFB-01247/06), BME – Instituto Superior Technico, Lisbon, supervisor: Dr. Sándor Ádány,
- OM ALK 00074/2000 Ministry of Education R&D project: Lindab light gauge building system, supervisor: Dr. László Dunai.

The author would like to express his especial gratitude to his supervisor Professor László Dunai who has elevated and supported him by their advice to improve the presented research.

The author would particularly like to thank to Professor László Kollár and Dr. Sándor Ádány with who have had esteemed corporate projects in the recent years.

He expresses his gratitude to thank László Kaltenbach, Dr. Miklós Kálló and the staff of the Structural Laboratory who, with their huge experiences and committed work, have helped the author to execute experimental tests.

The author has a claim to tender his thanks for all kind of help and support to the members of the Department of Structural Engineering.

Special thanks are due to his parents and grandfather who have emotionally supported him to choose teaching profession.

Abstract

Cold-formed thin-walled Z-purlins and cladding systems are widely used in steel industrial type buildings. In my research work I analysed the various components of cold-formed roof systems by experimental and numerical methods with the aim to define the behaviour modes of structural elements and details, and determine the test based design resistances in the lack of standardized methodology. The main details of my research are presented as follows.

In the first phase I designed and executed an experimental test program for compressed cold-formed thin-walled Z-section members, which I did not find in the investigated literatures. As the results of the experimental tests I determined the failure modes and the resistances of single and double Z-section members and Z-section members with trapezoidal sheeting lateral restraint, respectively. Special load introduction to the web is applied for the tests which has no standardized design resistance calculation. The new results are the failure modes and test based design resistances of this type of structural members.

I worked out a shell finite element model of the compressed Z-section members and I carried out numerical simulations on imperfect model including material and geometrical nonlinearities in the model. The equivalent geometrical imperfections are defined on the bases of the eigenmodes of the members. The experiences of finite element modeling shows that it is hard to classify the eigenmodes of a shell finite element model into the basic instability modes – local, distortional and global buckling – due to the presence of interacted modes. I worked out an algorithm which can classify the complex eigenmodes of a shell finite element models based on the deformation of the cross-section nodes along the member. The eigenmodes of a shell finite element model under compression can be classified on the basis of the constrained Finite Strip Method. I carried out a parametric study on C- and Z-section members with various discretization and boundary conditions and I proved that the method is applicable to classify the eigenmodes of FE models.

I carried out an imperfection sensitivity analysis to determine the effect of various buckling modes as equivalent geometrical imperfection to the ultimate load and the failure mode of the shell finite element model. The experiences are used illustratively in the modeling of experimental tests of compressed Z-section members. Complex geometrical imperfections are used in nonlinear simulations which are able to follow the behaviour of the experimental tests. I concluded the necessary imperfections to model the behaviour of compressed Z-section members.

In the next phase, I designed and executed an experimental test program on the joints of a continuous Z-purlin system. Three various details are analysed: (i) end of overlap for bending moment and shear force interaction, (ii) overlap support for bending moment and transverse force interaction and (iii) end support for transverse force. The overlap design resistance and the overlap stiffness can be determined by experimental tests only according to the proposal of the Eurocode 3. In my research, I determined the test based design resistances of the various details, and based on the results I determined the bending moment – shear force interaction curves for the end of overlap region. In case of overlap support tests, I proved that the standard design method is applicable for this type of structural details. Based on the end support test results, I proposed modification of the transverse force design resistance of the standard.

In the next phase of the research, I designed and completed an experimental test program on anti-sag elements of cold-formed thin-walled roof system. Various sag channels, peak elements and flying sag systems with tie rods are tested. The behaviour and the test based design resistances are derived from the tests. Shell finite element model of the sag channel is

developed and the necessary equivalent geometrical imperfections for nonlinear simulations are determined and calibrated to ensure same behaviour modes and ultimate load of the tests.

Based on my experimental and numerical research results I developed the bases and the algorithm of a complex design method of cold-formed thin-walled roof systems. The algorithm – called PurlinFED – can build the shell finite element model of a roof system: complex models with trapezoidal sheeting and supplementary cladding systems; control the analysis and evaluate the results. Three design methods are built in the algorithm that combines the results of beam and shell models at various analysis levels. The nonlinear simulation based design method is verified by full-scale experimental tests.

In the frame of the research, I executed altogether 180 experimental tests. I determined the test based design resistances for all cases and for end of overlap and end support I proposed the modification of the design resistance calculation. In all cases shell finite element models are developed and nonlinear analyses are carried out on imperfect models, where the imperfection size and distribution are determined on the basis of the experimental tests.

1. Introduction

The very close competition between the steel fabricators accelerates the continuous development of structural systems and design methods in the field of civil engineering. The cost of the secondary structural elements and the cladding system can be significant in the total price of an industrial type building; it can be reach the half of the total cost. So the development of roof and wall systems can affect remarkable savings to the steel fabricator. In my PhD dissertation I summarize my experimental and numerical research work on the fields of cold-formed thin-walled roof systems, which is inspired and supported by the industrial partners of the Department of Structural Engineering, BME.

The main components of an industrial type building are shown in Figure 1 and are as follows:

(i) the main frame which are typically produced by tapered welded I- or hot rolled section;
(ii) the secondary structural elements, usually cold-formed thin-walled Z/C-purlins and wall beams;
(iii) the cladding systems such as trapezoidal sheeting or floating panels and
(iv) supplementary elements such as anti-sag bars and flying sag systems.

Figure 1 shows a typical roof system: overlapped purlins with trapezoidal sheeting and anti-sag bars.

In my dissertation I introduce the structural problems of:

(i) compressed cold-formed thin-walled members, concentrated on Z- and C-section members in Chapter 2;
(ii) continuous Z-purlins in Chapter 3 and
(iii) supplementary elements of the roof system in Chapter 4.

The previous studies on these fields are reviewed and summarized by publications (and personal contacts with the main researchers of these topics) at the beginning of each chapter. Afterwards, the conclusions of previous studies are drawn and my applied research strategy – which leads to the new scientific results – is presented.

The structural problems are analysed in all cases by experimental tests:

(i) tests on compressed Z-section members in single and double arrangement and with or without trapezoidal sheeting;
(ii) overlap support, end of overlap, and end support details and
(iii) supplementary elements of roof systems such as various types of sag channels, peak elements and flying sag systems.

The experimental tests are evaluated, the behaviour modes and the test based design resistances are derived and new design methods are proposed.

Shell finite element models are built for all experimental tests and various analyses are carried out. The dissertation deals with the question of the classification of buckling modes by analysis of shell FE eigenmodes. As a summary of the research an algorithm and a computer program is developed, which is able to build, analyse and evaluate FE models of a whole roof system (Chapter 5).

Finally the new scientific results are summarized in Chapter 6.

In the introduction I emphasize the previous Hungarian studies on this field. The first book was published in 1965 by Csellár, Halász and Réti [1]. The book summarizes the fabrication technology, basic stability principals, design methods, connections and application. Experimental test are carried out on special Z-sections at the Department of Steel Structures of TU Budapest in 1983, and theoretical investigations are derived by P. Tomka in [2]. The research of thin-walled structures is extended by B. Verőci in [3] and [4] where experimental

tests and design methods are introduced for trapezoidal sheetings. By the spread of cold-formed thin-walled fabricators and products in Hungary a group of PhD students of L. Dunai [5] continued the research in this field.

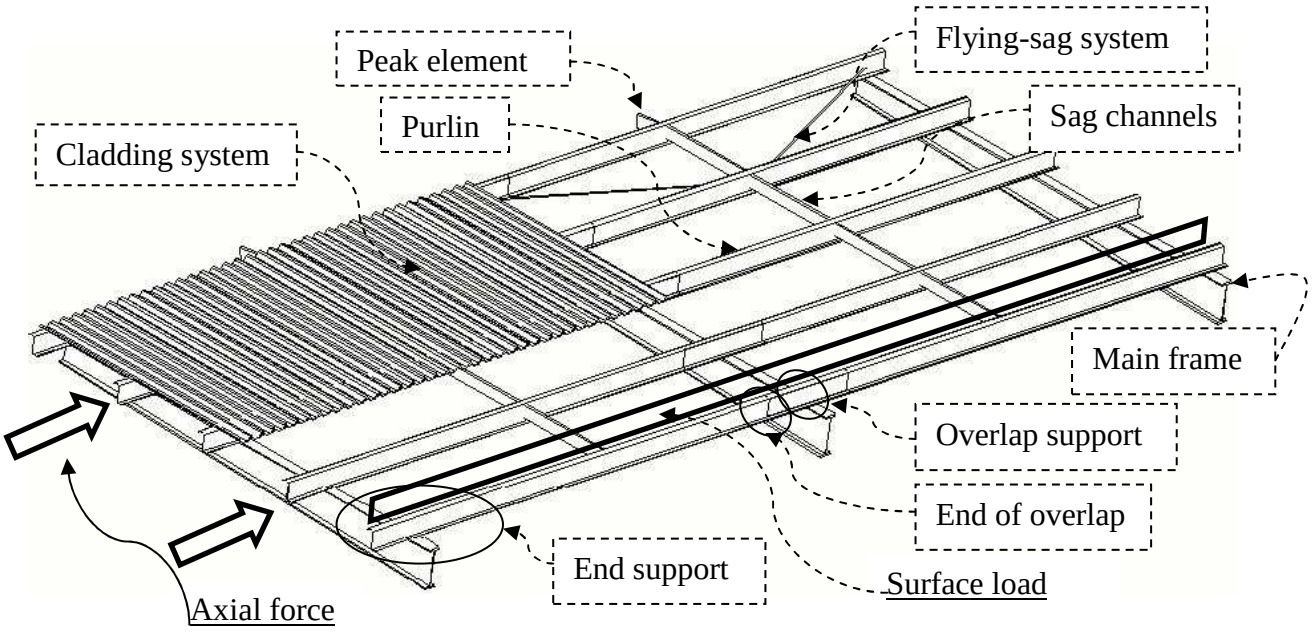

Figure 1. Typical cold-formed thin-walled roof system

2. Z/C cold-formed thin-walled members in compression

2.1 Introduction

2.1.1. Structural problems

The secondary structural elements – Z-purlins – carry surface loads from the roof such as self-weight or snow load and axial forces from the following effects:

- wind load on the end wall,
- compressed members of the wind bracing system,
- lateral support of the main frame,
- in plane forces of the roof from earthquake effect.

The usual structural arrangements of purlins and the presence of axial force leads to the following questions on the behaviour modes:

- local, distortional and global stability behaviour of compressed Z-section,
- interaction of compressed Z-section members and cladding system,
- local stability behaviour of the overlapped zones under compression.

The buckling modes of cold-formed thin-walled members (local, distortional and global) are usually demonstrated on C-sections which are widely used as a compressed member in light-gauge systems. In my research the focus is on Z-sections.

2.1.2. Previous studies

The behaviour modes of compressed cold-formed thin-walled members are widely analysed by both theoretical and experimental studies. According to the prevalent usage of compressed C-sections, its behaviour is deeply analysed comparing to the compressed Z-sections. Hardly any publications can be found in the literature on experimental analysis of Z-sections; [6] is focusing on the local buckling of the web only.

The buckling modes of cold-formed thin-walled members are the local, distortional and global modes as shown in Figure 2. These modes can be analysed by Generalized Beam Theory (GBT) [7], by Finite Strip Method (FSM) [8] or by Finite Element Method (FEM or FE). Figure 2 illustrates the result of a Finite Strip analysis. The horizontal axis represents the half-wavelength of the buckling of the member of its components while the vertical axis represents the critical load factors. The local minimums of the curves correspond to the local, distortional and global buckling modes. The distortional mode of Z-sections is described by GBT in [11], [12] to predict the critical stress. The GBT can handle only various end support conditions; while the FSM method is only able to take into consideration the rotational support of the cladding along the member and the end boundary conditions are pinned-pinned. The pure buckling modes are rarely occurs in a structural member, however an interacted mode decomposition can be determined in constrained Finite Strip Method (cFSM) [13], [14], [15], [16] and [8].

Both special end support conditions and partial or full rotational restraints can be handled in various analysis levels by the FE method [17]. The eigenmodes and eigenvalues of a member can be calculated by linear instability analysis; furthermore the behaviour can be followed by full nonlinear (material and geometrical) analysis on imperfect models. As one of the main questions in a nonlinear simulation there are several methods in the literature to define the real geometrical imperfections and the residual stresses of various thin-walled members: C-section in [18], and for Σ-profile in [19]. The measured data are applied on finite element models, the effect of distortional type imperfections is analysed in [20] for C-sections. The interaction modes on the behaviour of rack sections are predicted in [21].

Design method for compressed thin-walled members is included in European [60], American [62] and Australian [63] standards. The Eurocode supports the application of finite element models for the resistance calculation in case of plated structures [61] but there is no recommendation for cold-formed thin-walled members, especially the application of imperfections is an open question.

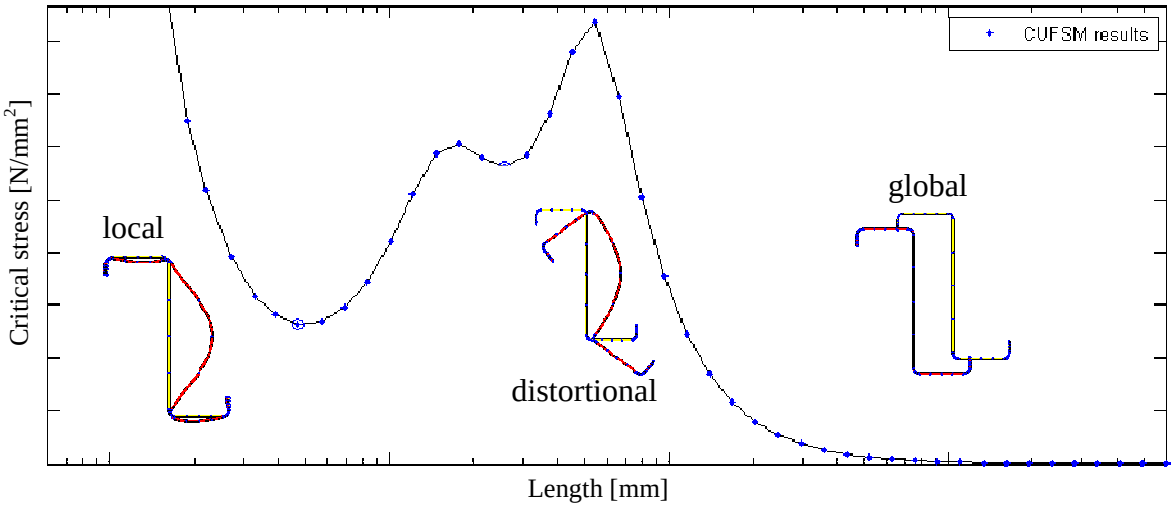

Figure 2. Local, distortional and global buckling modes of Z-section under compression

2.1.3. Conclusions on previous studies

On the basis of existing research studies the following conclusions can be drawn:

- analytical solution can be found in the literature for various buckling modes by different solution methods,
- in nonlinear finite element models the key point is the adaptation of imperfection, however there is no consensus exists on the distribution and the magnitude to be used.

In the investigated literature I did not find:

- experimental tests of compressed Z-section,
- behaviour modes of laterally supported Z-section members for compression,
- experimental analysis on the behaviour modes of the overlapped zone of Z-purlins under compression,
- finite element model, which can follow the behaviour modes by nonlinear simulation of compressed Z-section,
- geometrical imperfections are based on measured data, however it is more evident to apply the eigenmodes of the structures as equivalent geometrical imperfection, where equivalent geometrical imperfection means that all type of imperfections are replaced by geometrical imperfections that effect the same behaviour and ultimate load.

2.1.4. Purpose and research strategy

The aim of the current research is to identify the behaviour modes of compressed Z-section by experimental tests:

- various buckling modes of single and double section,
- laterally supported section on one flange by trapezoidal sheeting,
- compression test of the overlapped zone.

The test program and the test results are presented in Chapter 2.2.

Shell finite element model is developed which can follow the experienced behaviour modes. This model requires sensitivity analysis on various types of imperfections with different amplitudes based on the eigenmodes of the structure. The eigenmodes usually consists of interaction of pure buckling modes which cannot be identified by any methods in the literature. This fact inspired the research on the classification of the eigenmodes by finite element model.

The first classification method is based on geometrical definition (visual observation) of the pure buckling modes in Chapter 2.4. After the classification the effect of the different modes on the behaviour of the model are checked by parametric studies and the results are illustrated by the experimental tests (Chapter 2.5). The results showed the importance of the buckling mode shape imperfection in case of shell finite elements, so another method is proposed for buckling mode identification.

The second part of the research is based on constrained Finite Strip Method (cFSM) [13] developed by S. Ádány, where the interacted modes are decomposed as the linear combination of pure modes created in cFSM. A parametric study is carried out on C-section to analyse the accuracy of the proposed method in Chapter 2.6 and the method is applied on Z-section members.

2.2 Experimental tests

An experimental research program is completed on cold-formed Z-section compressed members in the Structural Laboratory of the Department of Structural Engineering of BME. The main purposes of the research are to investigate the different stability phenomena and to determine the test based design resistances under such conditions, which are not handled by standard methods. In the experimental program 24 specimens are studied having different lengths and supporting conditions. The obtained stability phenomena are the interaction of local, distortional and global buckling modes. The results are evaluated in details; the behaviour modes are identified and characterised, and the design resistances of the specimens are determined for practical application purpose. The test documentation can be found in [23].

2.2.1. Design of specimens

The experimental study aimed to investigate Z-section compressed members with special conditions, which cannot be handled by standard design procedures. These are related to the non-typical arrangement of the sections, the type of load introduction, and the structural solutions of the lateral supports. The general purpose of the research is to analyse the complex and interaction stability phenomena under such conditions. The more specific purpose is to find the test based design resistances of the structural solutions for practical applications. The specimens and the test program are designed on these purposes.

The specimens are fabricated from Lindab Z 150 and 200 profiles. The geometry of the specimens is as follows: length: 800, 2000 and 3600 mm; cross-section height: 150 and 200 mm; thickness: 1.0 and 2.0 mm. Both single- and double-profile-specimens are investigated, and overlap arrangements are also tested. The end supports are prepared by web gussets without warping restraint. The specimens are tested without lateral and with one-sided lateral supports (trapezoidal sheeting, LTP45/0.5).

The test specimens are designed on the bases of the investigation of the local, distortional and global stability phenomena. The preliminary buckling analysis is done by finite strip method [66] using the above detailed geometrical data and supporting requirements.

The results of the instability analysis (buckling modes, critical load factors) of the Z-sections with different lengths are illustrated in Figure 2. The main geometrical data of the

test specimens – global lengths, plate b/t ratios – are derived from the results of the instability analysis and supplementary standard checking [60].

2.2.2. Test specimens

The details of the 24 Z-section test specimens are summarized in Table 1. The Z-sections are fabricated with different width of flanges in order to combine and connect them together. The double Z-section members are arranged in an “overlap” position. No bolts are used to connect the two Z-section members to each other. The lateral supports are applied only on one flange of the members. The gusset plate type end supports are connected to the webs of the members by self-drilling screws; the numbers of the screws are determined according to the predicted ultimate load.

Table 1. Test specimens

Specimen #	Profile	Thickness	Length [mm]	Section	Lateral support
Z01	Z200	2.0	800	single	-
Z02	Z150	1.0		single	-
Z03	Z200	1.0		single	-
Z04	Z200	2.0		double	-
Z05	Z150	1.0		double	-
Z06	Z200	1.0		double	-
Z07	Z200	2.0		single	trapezoidal sheeting
Z08	Z150	1.0		single	trapezoidal sheeting
Z09	Z200	1.0		single	trapezoidal sheeting
Z10	Z200	2.0		double	trapezoidal sheeting
Z11	Z150	1.0		double	trapezoidal sheeting
Z12	Z200	1.0		double	trapezoidal sheeting
Z13	Z200	2.0	2000	single	-
Z14	Z150	1.0		single	-
Z15	Z200	1.0		single	-
Z16	Z200	2.0		single	trapezoidal sheeting
Z17	Z150	1.0		single	trapezoidal sheeting
Z18	Z200	1.0		single	trapezoidal sheeting
Z19	Z200	2.0	3600	single	-
Z20	Z150	1.0		single	-
Z21	Z200	1.0		single	-
Z22	Z200	2.0		single	trapezoidal sheeting
Z23	Z150	1.0		single	trapezoidal sheeting
Z24	Z200	1.0		single	trapezoidal sheeting

2.2.3. Test arrangement

The specimens are tested in vertical position in a loading frame, as it is shown in Figure 3. The load is introduced at the lower end of the specimens by a hydraulic system, through a vertically driven horizontal plate. The gusset plate supports at the lower end of the members are connected to this loading plate, as shown in Figure 4. The lateral supports (trapezoidal sheets) are connected to one side of the tested profile and to the columns of the loading frame, as illustrated in Figure 3.

The load, the shortening of the specimen and the horizontal displacements in the middle of the specimens are recorded continuously. The measured horizontal displacements are shown in Figure 5.

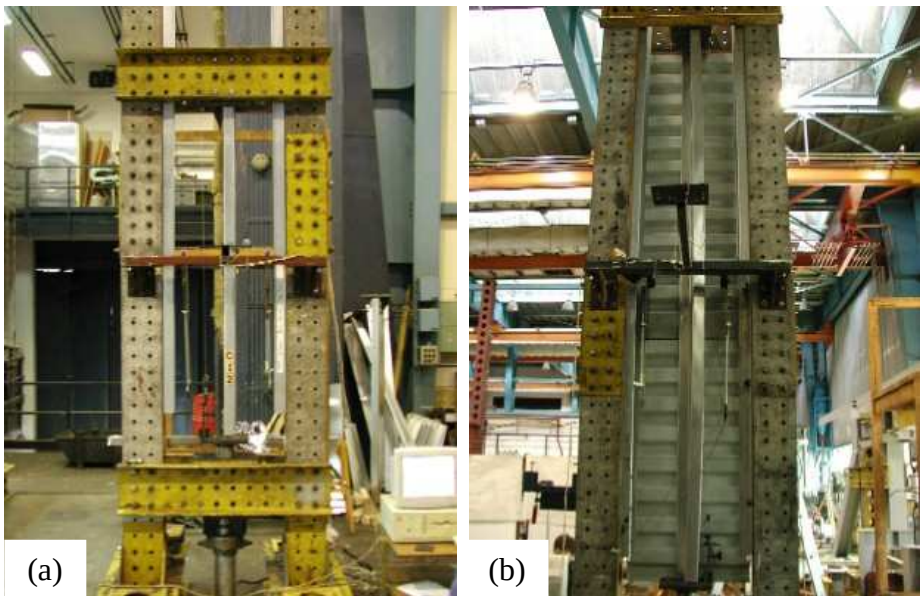

Figure 3. Test setup: (a) global test arrangement and (b) lateral supports by trapezoidal sheet on Z-section specimen

Figure 4. Load introduction: gusset plate and self-drilling screws

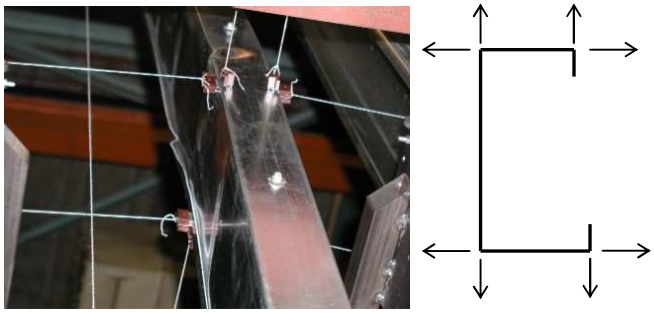

Figure 5. Measuring the displacements in the middle of the specimen

2.2.4. Typical behaviour modes

The typical – local, distortional and global – behaviour modes of single Z-section specimens are illustrated in Figure 6. Figure 7 shows the pertinent load – shortening relationships. In the behaviour the local plate buckling of the Z-section web always appeared in the elastic range. Other local phenomenon is the crushing of web near to the load introduction (Figure 6a) in cases of short specimens and when effective lateral supports are applied in longer specimens.

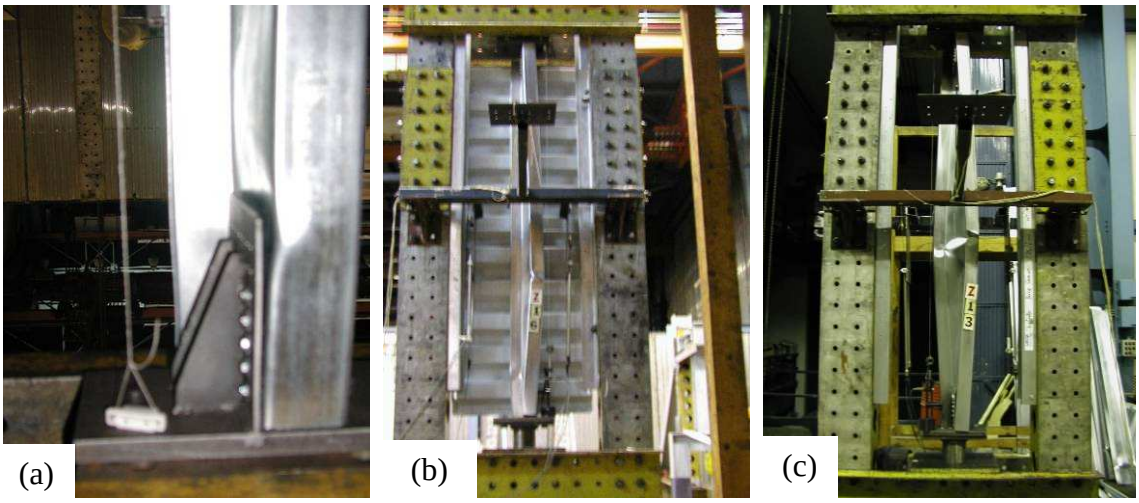

Figure 6. Behaviour modes: (a) local web crushing (Z01), (b) distortional buckling (Z16) and (c) global buckling (Z13)

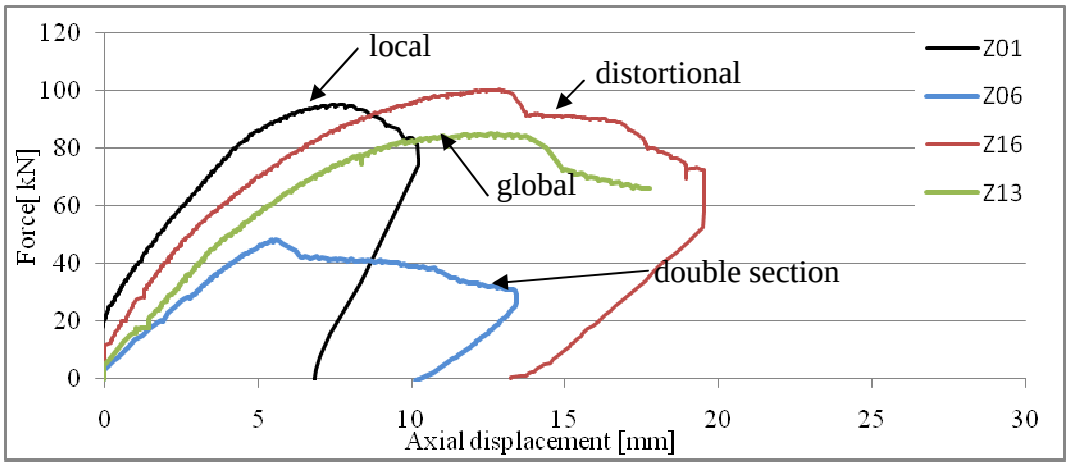

Figure 7. Load – shortening relationships

The most typical experimental behaviour is the distortional buckling of the laterally unsupported flange of the Z-section (Figure 6b and Z16 on Figure 7). The final failure is generally caused by the developing of a yield mechanism in the most bent position. The interaction of distortional buckling and web crushing is experienced when the buckling of the free flange is happened near to the ends (Z01 on Figure 7). The global buckling is observed in the cases of laterally unsupported, longer specimens. Despite the cross-section arrangement (Z-section with different sizes of flanges), almost pure torsional (Figure 6c) and pure flexural buckling modes are obtained beside the flexural-torsional modes (Z13 on Figure 7).

The measured load and shortening curves show the typical features of the limit point type stability behaviour. The rigidity changing after the linear part represents the effect of the local plate buckling of the webs. In case of double sections the two members fail separately and after the crushing of the first member there are residual load bearing capacity until the failure of the second member (Z06 on Figure 7).

2.2.5. Experimental behaviour and ultimate loads

The observed behaviour modes and the measured ultimate loads of Z-section specimens are collected in Table 2.

Table 2. Experimental behaviour, ultimate load and design resistances

Test code	Behaviour mode (failure location)	Ultimate load [kN]	Design resistance [kN]
Z01	Crushing of the web (at the lower and upper ends, near to the screwed connection)	95.32	65.29
Z02	Interaction of distortional buckling and crushing of the web (at the lower and upper ends, near to the screwed connection)	22.56	18.27
Z03	Interaction of distortional buckling and crushing of the web (at the lower and upper ends in the screwed connection)	14.19	11.50
Z04	Distortional buckling (in the middle of the specimen)	190.82	130.71
Z05	Distortional buckling (in the middle of the specimen)	42.39	34.34
Z06	Distortional buckling (near to the lower end)	48.41	39.21
Z07	Distortional buckling of the free flange (in the middle of the specimen)	95.32	65.29
Z08	Distortional buckling of the free flange (near to the lower end)	22.98	18.62
Z09	Interaction of distortional buckling of the free flange and crushing of the web (near to the lower end)	20.82	16.87
Z10	Distortional buckling of the free flange (in the middle of the specimen)	184.80	126.59
Z11	Distortional buckling of the free flange (in the middle of the specimen)	45.97	37.23
Z12	Distortional buckling of the free flange (near to the upper end)	53.02	42.94
Z13	Torsional buckling (in the middle of the specimen)	85.26	45.42
Z14	Flexural-torsional buckling (in the middle of the specimen)	16.17	10.19
Z15	Flexural-torsional buckling (in the middle of the specimen)	20.92	13.18
Z16	Distortional buckling of the free flange (in the lower part of the specimen and near to the lower end)	100.49	68.83
Z17	Distortional buckling of the free flange (in the lower part of the specimen)	20.16	16.33
Z18	Interaction of distortional buckling of the free flange and crushing of the web (at the lower end, near to the screwed connection)	27.03	21.89
Z19	Torsional buckling (near to the middle of the specimen)	68.10	36.28
Z20	Flexural buckling in the plane perpendicular to the web (in the middle of the specimen)	10.67	6.72
Z21	Crushing of the web (at the upper end in the screwed connection)	19.36	12.20
Z22	Distortional buckling of the free flange (in the lower part of the specimen and near to the lower end)	95.13	65.16
Z23	Interaction of distortional buckling of the free flange and crushing of the web (near to the lower end)	19.90	16.12
Z24	Int. of distortional buckling of the free flange and crushing of the web (at the lower end in the screwed connection)	22.10	17.90

It is noted, that the local, elastic plate buckling is experienced in the webs of all the specimens; this is not mentioned in the table in general, unless it has essential effect in the failure phenomenon. The detailed behaviour mode gives the stability phenomena which characterise the performance until the limit point; after the type and place of experienced failure is enclosed for all the specimens.

The measured ultimate loads are detailed for single Z-section specimens without and with lateral supports in Figure 8.

Figure 8 shows that in the case of lower web b/t ratio (Z 200/2, Z150/1) – due to the global behaviour – the typical column buckling curve points are obtained from the tests. When web b/t ratio is increased (Z 200/1) the local behaviour plays important role, keeping the ultimate load almost independent of the length of the member. Similar tendencies are experienced when lateral supports are used on one flange of the Z-section member. In those cases the behaviour is governed by the distortional mode and the interaction of the distortional and local modes resulting in the above findings.

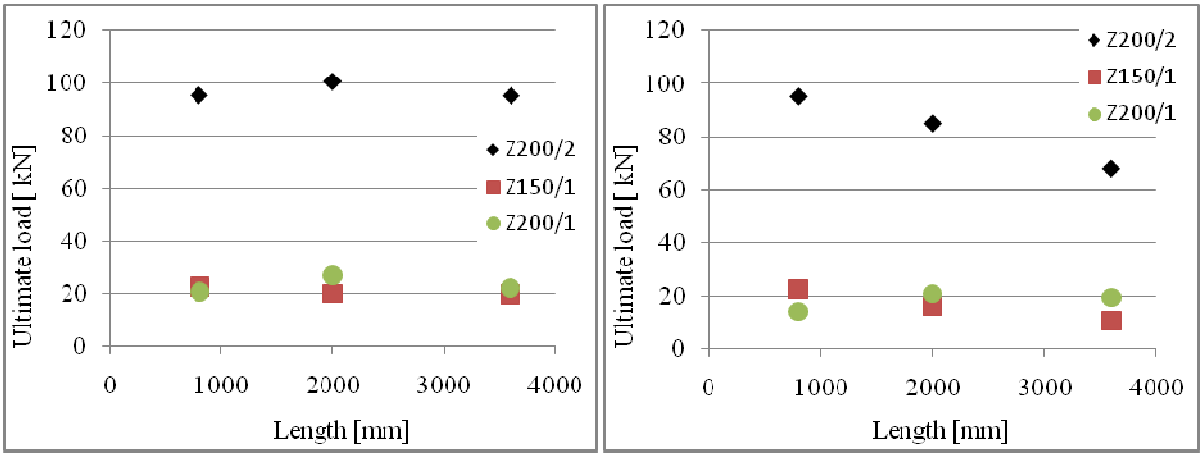

Figure 8. Ultimate loads in Z-section specimens: (a) without and (b) with lateral supports

2.2.6. Material tests

Tensile tests are carried out on specimens cut out from each different Z-section flanges and web. There were three different sections, and 6 or 10 specimens are tested according to Figure 9; altogether 26 tests are done. The test results are summarized in Table 3 for the Z200/2 profile, in Table 4 for the Z200/1 profile and in Table 5 for the Z150/1 profile.

If the measured stress-strain curves have significant plato the yield stress is marked as R_{eH}, in other cases the yield stress is defined as the stress corresponds to the 0.2% residual strain and marked as $R_{p0.2}$.

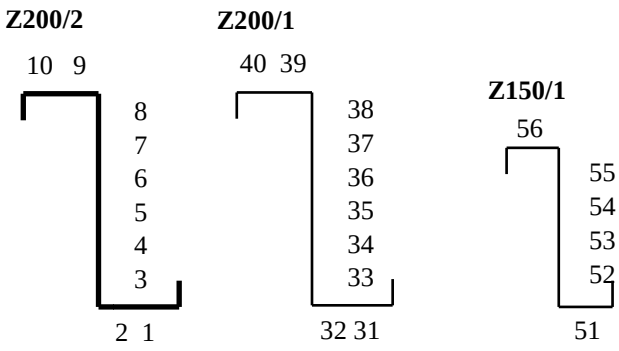

Figure 9. Tensile specimens' location in the cross-sections

Table 3. Material test results of Z200/2 section

Material test specimen	The specimen thickness [mm]	width	Yield stress $R_{p0.2}$ [N/mm^2]	R_{eH} [N/mm^2]	Ultimate stress [N/mm^2]	Ultimate strain [%]
1	2.04	20.5	419.6	-	481.46	10.7
2	2.04	20.2	421.2	-	484.90	10.5
3	2.04	20.1	381.7	-	490.30	10.5
4	2.04	20.1	420.4	-	487.06	11.1
5	2.04	20.0	427.5	-	490.75	11.2
6	2.04	20.0	423.7	-	489.75	10.2
7	2.04	20.1	420.1	-	487.31	11.7
8	2.04	20.1	426.8	-	490.30	10.5
9	2.04	20.0	426.7	-	489.25	11.5
10	2.04	19.9	430.9	-	490.95	11.8

Table 4. Material test results of Z200/1 section

Material test specimen	The specimen thickness [mm]	width	Yield stress $R_{p0.2}$ [N/mm^2]	R_{eH} [N/mm^2]	Ultimate stress [N/mm^2]	Ultimate strain [%]
31	1.03	19.8	353.5	-	417.68	13.6
32	1.03	20.0	352.3	-	415.00	13.5
33	1.03	19.8	357.3	-	418.69	13.2
34	1.03	20.1	349.9	-	411.44	12.6
35	1.03	20.0	348.8	-	414.50	12.6
36	1.03	19.9	349.1	-	417.59	13.8
37	1.03	20.0	352.2	-	416.00	13.8
38	1.03	19.9	355.0	-	419.10	12.8
39	1.03	20.1	352.7	-	415.92	13.1
40	1.03	20.0	347.7	-	414.50	12.3

Table 5. Material test results of Z150/1 section

Material test specimen	The specimen thickness [mm]	width	Yield stress $R_{p0.2}$ [N/mm^2]	R_{eH} [N/mm^2]	Ultimate stress [N/mm^2]	Ultimate strain [%]
51	1.05	20.3	340.8	-	413.79	14.1
52	1.05	20.2	337.5	-	414.85	13.0
53	1.05	20.3	349.6	-	411.33	13.0
54	1.05	20.4	346.6	-	409.31	13.1
55	1.05	20.4	345.6	-	406.86	14.4
56	1.05	20.4	340.8	-	404.41	14.1

The yield stress distribution of the various sections is shown in Figure 10. The measured values of the yield stress show hardly any hardening effect around the edges of the cross section. It can be explained by the fact that the specimens are cut out away from the edges due to the round corners. The maximum deviation from the average yield stress is 5%.

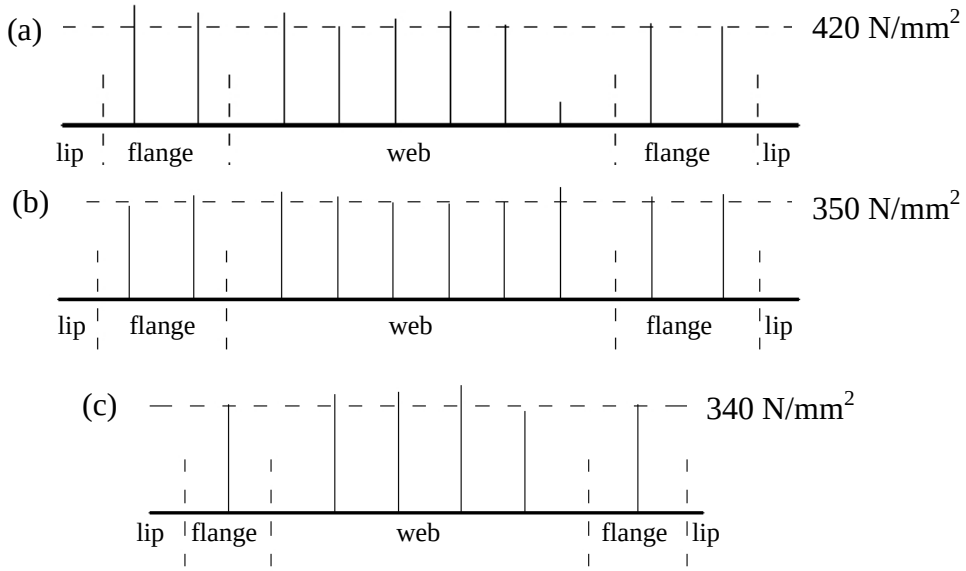

Figure 10. Yield stress distribution on the sections: (a) Z200/2, (b) Z200/1 and (c) Z150/1

2.2.7. Test based design resistances

The results of each test series are evaluated to define the standard design resistances according to the Eurocode 3 [60].

The standard design resistance can be calculated from one measured values as follows:

The measured test result is R_{obs}.

The adjusted value is:

$$R_{adj} = R_{obs} / \mu_R \tag{1}$$

where

$$\mu_R = \left(\frac{f_{yb,obs}}{f_{yb}} \right)^{\alpha} \left(\frac{t_{obs,cor}}{t_{cor}} \right)^{\beta} \tag{2}$$

$f_{yb,obs}$ is the measured yield stress,

f_{yb} is the nominal yield stress ($f_{yb} = 355$ N/mm^2),

$t_{obs,cor}$ is the measured value of the core material thickness,

t_{cor} is the nominal core material thickness,

$\alpha = 1$ if $f_{yb,obs} > f_{yb}$,

$\beta = 1$ if $t_{obs,cor} \le t_{cor}$, other cases can be found in [60].

The characteristic value of the resistance is:

$$R_k = 0.9 \times \eta_k \times R_{adj} \tag{3}$$

The observed failure is yielding failure so $\eta_k = 0.9$ is applied and $\eta_k = 0.7$ is used for overall instability failure. The design value is calculated as:

$$R_d = \eta_{sys} \times \frac{R_k}{\gamma_M} \tag{4}$$

$\eta_{sys} = 1$ because the test conditions followed the applied solution,

$\gamma_M = 1$ the partial factor (according to Eurocode [59]).

2.2.8. Conclusions on the design resistances

The test based design resistances are shown in Table 2. The design resistances follow the tendencies presented in Figure 8 due to the similar reduction in the test based design procedure. The conclusion of this research is the new behaviour modes of compressed Z-section members in various structural arrangements and the test based design resistances.

The results of the 800 mm members showed that the largest design resistance corresponds to the smallest web height/thickness ratio (100) and the design resistance decreasing by almost to 25% by increasing the web height/thickness ratio to 150 and 200. The design resistances of the 150 and 200 web height/thickness ratio are close to each other due to the 1 mm thickness in both cases. This proves that the thickness plays major role in the resistance. The design resistance of the double section is almost doubled. The tests of short elements with trapezoidal sheeting showed that it has no effect on the resistance due to the local failure mode. In case of 2000 mm length members where global failure is occurred the design resistance is increasing by 50% if trapezoidal sheeting is applied. Same tendencies can be observed on the results of the 3600 mm members. In both cases significant differences can be observed for the various plate thicknesses for global failure modes as well. The results of 1 mm thickness elements are close to each other while the resistance of the 2 mm thickness element is significantly higher.

2.3 Finite element modeling of compressed Z-section members

2.3.1. Introduction

In parallel with the experimental study a numerical model is developed by Ansys [64] finite element program using shell elements. The basis of the research is the experimental program on compressed Z-section members presented in Chapter 2.2, however a general method is worked out that is able to classify the eigenmodes of a shell finite element model.

It is well known that taking into consideration of geometric imperfections in modeling has primary importance in case of numerical simulations of thin-walled steel members. One possible method for modeling of geometrical imperfection is to apply the result of buckling analysis in the geometric model of the structure with the typical local, distortional and global buckling modes. Other suggestions can be found in [18], where measured geometric imperfections are applied as Fourier series and in [20] where eigenmodes by amplitudes of measured imperfections are applied in numerical models.

If the member consists of thin plates, such as cold-formed steel products or as in many welded applications, not only global buckling (e.g. flexural or flexural-torsional), but also local and distortional buckling, as well as various interacted buckling modes, may play major role in the ultimate behaviour of the member and therefore in the design philosophy, respectively. If local buckling occurs in a structural member it has post critical reserve while in case of distortional and global buckling there is no reserve. The analysis of these instabilities by numerical methods requires the consideration of more degrees of freedom than in classical analytical solutions.

Due to the advances of computational technology, and due to its infiltration into the everyday engineering life, the handling of various buckling modes can be done in the analysis, as far as the calculation of buckling modes and the associated critical forces are concerned. Several finite element codes are available, most of them having various shell or solid elements that are necessary to perform the buckling analysis with the required accuracy. The new facilities, however, bring new problems. An important one is that while shell finite element is an excellent tool for the calculation of buckling modes/forces, it produces a large number of buckling modes most of which are apparently interacted. Thus, it is the user who

has to manually identify those modes where the interaction seems to be weak, since the “pure” modes are the ones on which the classical design approaches are based. Therefore, an automatic buckling mode identification method would be certainly appreciated.

Two general numerical methods are developed which can recognize and classify the eigenmodes of thin-walled members. The first method based on the visual observation of the shell FE eigenmodes. The proposed method analyses the nodal displacements, the number of half-waves along the member of the buckling shape and the maximum deformation. This method is detailed in Chapter 2.4. The other method developed by S. Ádány is based on the approximation of the FE eigenmodes by the base functions of the Finite Strip Method. The participation of the pure modes in the shell FE eigenmodes are also obtained by the classification method. The details and the results of a parametric study are presented in Chapter 2.6.

The local, distortional and global buckling modes and their interactions classified by the automatic recognition method are applied as the distribution functions of equivalent geometrical imperfections for the numerical models. On the imperfect model nonlinear numerical simulations are carried out to analyse the stiffness, the failure mode and the ultimate load. By the application of the method a parametric study is completed. The results are used to predict the geometric imperfections of Z-section compressed members to apply it in numerical analysis (Chapter 2.5).

2.3.2. Finite element model

For the purpose of automatic generation of imperfect finite element models a research target program is developed. This tool – called “PurlinFED” – can build finite element shell models for Ansys program, and it can evaluate the results automatically of various analyses such as linear, buckling or nonlinear. The program is presented in Chapter 5.

The developed finite element models are corresponding to the Z-section test specimens: the web is divided into 12, the flanges into 4 and the lips into 2 elements. The model restraints follow the structural solution of the actual support conditions applied by gusset plate and self-drilling screws in the experimental program. Fix boundary conditions are applied at the centre of self-drilling screws. For linear and instability analysis concentrated forces are applied at the restrained nodes and kinematic load is used for nonlinear analysis. The mesh and the end detail of a single Z-section model are shown in Figure 11a. The FE model of purlin restrained by trapezoidal sheeting is shown in Figure 11b.

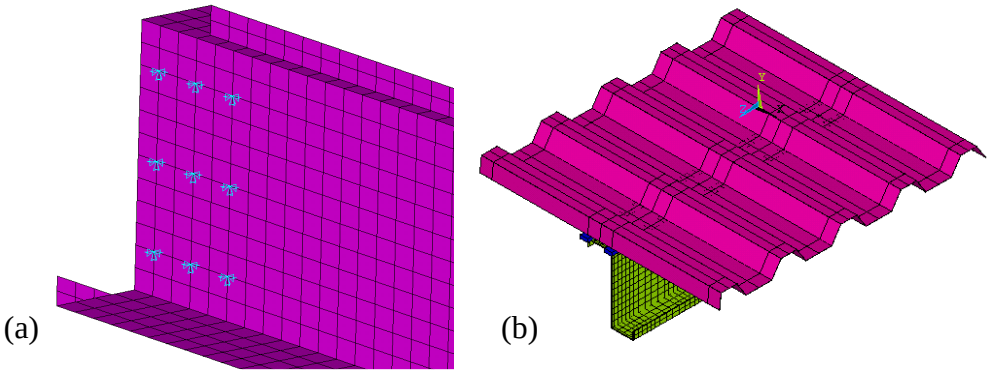

Figure 11. FE model: (a) mesh and support model, (b) purlin with trapezoidal sheeting

2.3.3. Analysis

In the first step instability analysis is carried out on the finite element model to calculate the eigenmodes of the compressed Z-section members. These eigenmodes and eigenvalues

can be used in standard based design to calculate the pertinent slenderness ratios, or can be used for the prediction of geometric imperfections for numerical simulations. In this research a method is developed to get imperfect model for numerical simulation using the classified buckling modes. Geometrical and material nonlinear analyses are carried out on imperfect models of the Z-section members. An increased intensity of the measured ultimate loads of the experimental tests is applied to the FE model and this load is divided at least 10 equal load steps. In some cases smaller load steps are applied for higher numerical accuracy. In each load step maximum 15 iterations are used to satisfy the equilibrium. The equilibrium in one load step is reached, when the Euclidian norm of the unbalanced forces is smaller or equal than 0.1%. If convergence is not reached by the 15 iterations the solution is continued by a reduced load step. The minimum load step is defined as 1% of the first load step. If the analysis cannot find solution by the reduced load step, the calculation stops. This load will be the ultimate load if the non-convergence is not caused by numerical instability of the model. In the nonlinear analyses the measured material properties are used which are obtained from tension tests.

2.4 Identification of FE buckling modes by automatic recognition method

2.4.1. Introduction

The results of shell FE instability analysis are usually contain interacting buckling modes. The most common evaluation of these modes is the visual observation where the decision of the classification – if it can made at all – highly dependent on the experience of the engineer. In the proposed method, an automatic recognition algorithm takes out the visual observation. The algorithm collects and arranges the nodal displacements in representative cross section points along the member, and by the analysis of ordered data classifies the eigenmodes into pure buckling modes.

2.4.2. Buckling modes

The typical pure local, distortional and global buckling modes of the numerical models are illustrated in Figure 12 in case of Z-section compressed members.

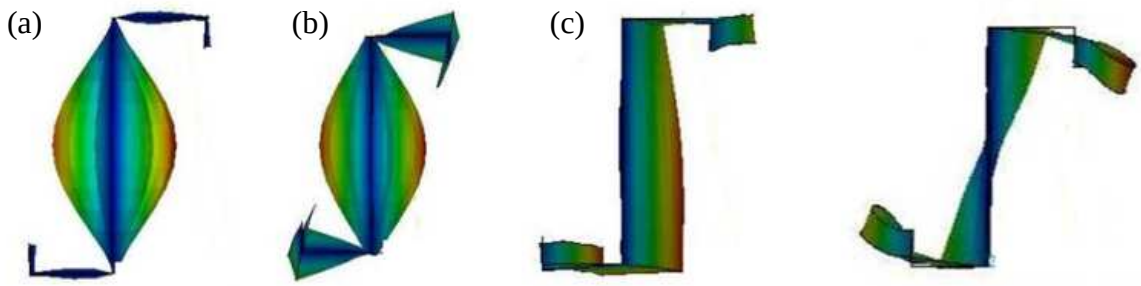

Figure 12. Buckling modes of numerical model: (a) local, (b) distortional and (c) global

The first task in the proposed procedure is to define the possible pure buckling modes of a structural element (in this case Z-section compressed members). The local modes are the buckling of the lip, the flange or the web, as it is illustrated in Figure 13a. The distortional buckling modes are shown in Figure 13b, where the buckling of a flange or a flange with the web can be observed. The global buckling mode is flexural-torsional buckling. Due to the applied geometry of the section, however, the experienced global behaviour can be defined as presented in Figure 13c, such as flexural buckling around the axes parallel or orthogonal to the web of the section or torsional buckling. In this research these modes are handled as “pure” global modes.

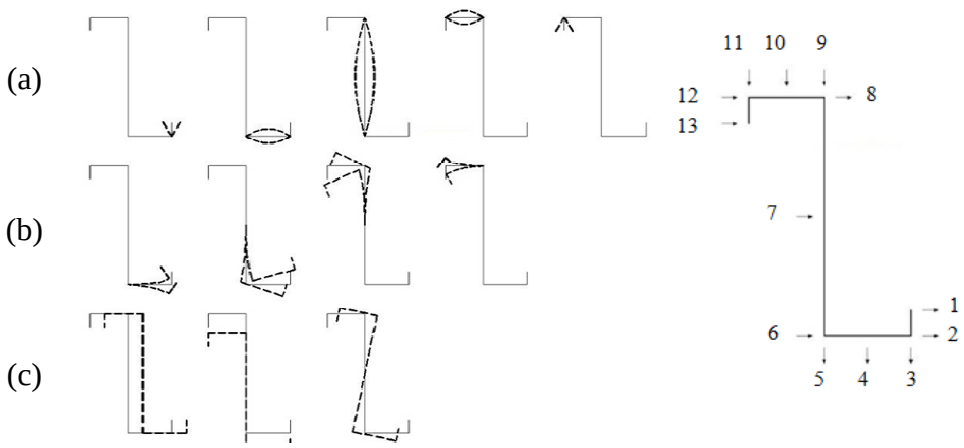

Figure 13. Definition of (a) local, (b) distortional, (c) global buckling modes and (d) analysed edges and directions of nodal displacements of the cross-section

2.4.3. Buckling shape recognition

To be able to recognize and classify buckling modes automatically the following method is developed which is built in the PurlinFED program, detailed in Chapter 5.

13 edge deformations of the Z-section – shown in Figure 13d – are collected into a database along the member in every node and for every eigenmode. The number of half-waves, the maximum and minimum values of the deformation and the co-ordinates of these extreme values are determined.

According to these ordered numerical data and preliminary analysis of the eigenmodes, the ratios of the maximum edge deformations can be obtained by the analysis of large number of buckling modes. These ratios can be used to classify the eigenmodes into the pure buckling modes independently of each other so the interacted modes also can be recognized. However there are other modes, where a complex interacted eigenmode neither by visual check nor by this proposed method can be classified properly. These approximate ratios and classification conditions can be defined according to local, distortional or global buckling modes.

The number of half-waves at the 1st, 4th, 7th, 10th and 13th edges and the ratios of the maximum deformation to the deformation of the whole member can describe the condition of local buckling. By the application of these conditions the local buckling modes, including web crushing or crippling can be excluded.

The evaluation and recognition program windows in PurlinFED are shown in Figure 14 and Figure 15. The presented deformations of the edges are marked with red arrow. In case of local buckling the deformation line of the middle of the web – 7th edge – can be seen in Figure 14a.

The four distortional buckling modes can be recognized by the analysis of four different edge pairs: 3-5, 6-8, 8-6 and 9-11, according to Figure 13b. By the differences in the deformations of these pairs the distortional buckling modes can be recognized. Both lower and upper flange distortional buckling can be seen in Figure 14b.

In case of global buckling the two flexural buckling modes can be identified by the analysis of the difference between the deformations of edge pairs 6-8 and 5-9. Further conditions are required for the ratio of the maximum deformation of these edge pairs and the maximum deformation of the whole member. The procedure is almost the same in case of torsional buckling; only the deformations of 6th and 8th edges have to have different signs. Flexural-torsional buckling can also be recognized if the two deformations are not equal (the deformation values are between the flexural and the torsional modes). The global buckling modes are illustrated in Figure 15.

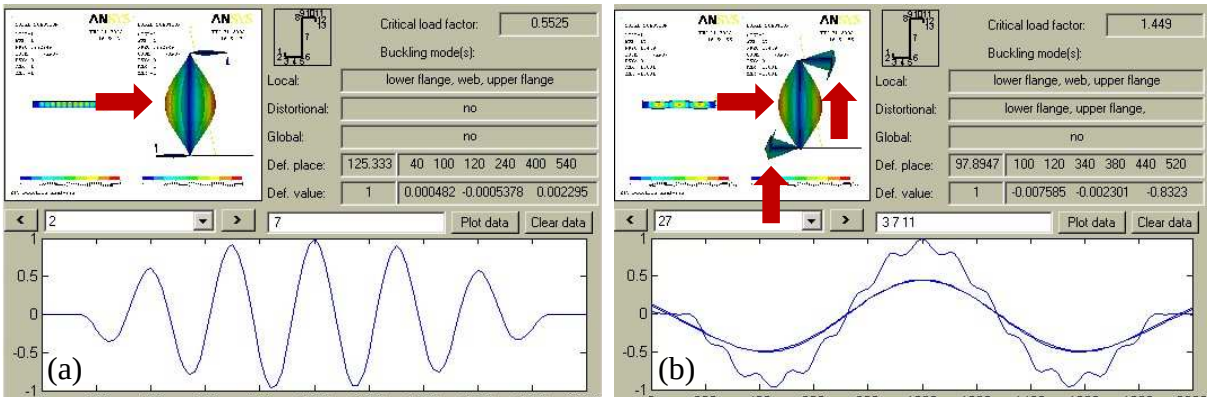

Figure 14. Deformations of the edges: (a) local and (b) distortional

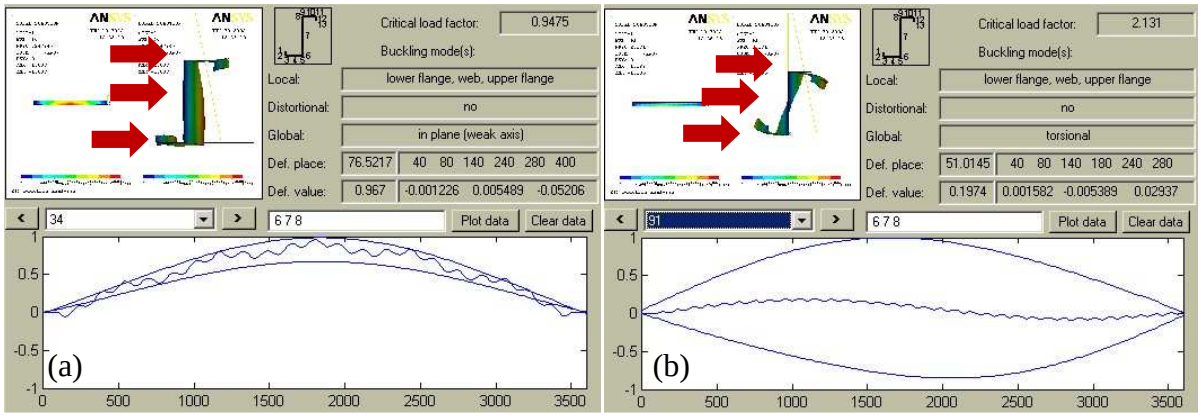

Figure 15. Global deformations of the edges: (a) flexural-torsional and (b) torsional

2.4.4. Imperfection generation

In the current study the first 100 buckling eigenmodes of the Z-section compressed members are calculated and analysed by the proposed method. In the first step the local, distortional and global buckling modes are determined; the maximum deformations and the positions of waves are calculated. In the next step the mesh of the numerical model is updated by one of the selected pure buckling shape as the distribution function of the geometrical imperfection. A constant multiplier is used to resize the normalized buckling shape deformations to get a specific sized imperfection. Furthermore on the imperfect numerical model nonlinear simulation is carried out. After the analysis of imperfections on the bases of pure buckling shapes, combined buckling modes are also applied as imperfections. In these cases two or more buckling shapes are selected and applied by various multipliers to result in multiple geometric imperfections. The results are detailed in Chapter 2.5.

The principals of the method can be extended to analyse other types of thin-walled sections, under different loading condition [24], too.

2.5 Parametric studies on various imperfections

The method, detailed in Chapter 2.4 is applied for the imperfection sensitivity analysis of Z-section compressed members. The effect of local, distortional and global type of imperfections are analysed on three various lengths (800, 2000 and 3600 mm) of a selected Z-section from the experimental tests with web height of 200 mm and thickness of 2.0 mm.

2.5.1. Effect of local imperfections

Buckling shapes according to Figure 14 are applied in each case with the maximum proposed deformations of [18] and [20]. In these cases the imperfections contains only local deformations according to local buckling modes, as it can be seen in Table 6.

In Table 6 the calculated ultimate loads of the virtual experiments are presented together with the differences compared to the perfect numerical model.

The ultimate behaviour of the perfect and the imperfect numerical models are described by the force – shortening diagram in Figure 16. As it can be seen the local imperfections have effect on both the initial stiffness of the member and on the ultimate load. The imperfection sensitivity relationship is almost linear (see Figure 17) in case of the three lengths, the maximum decreasing is 5% in the case of 2 mm web imperfection.

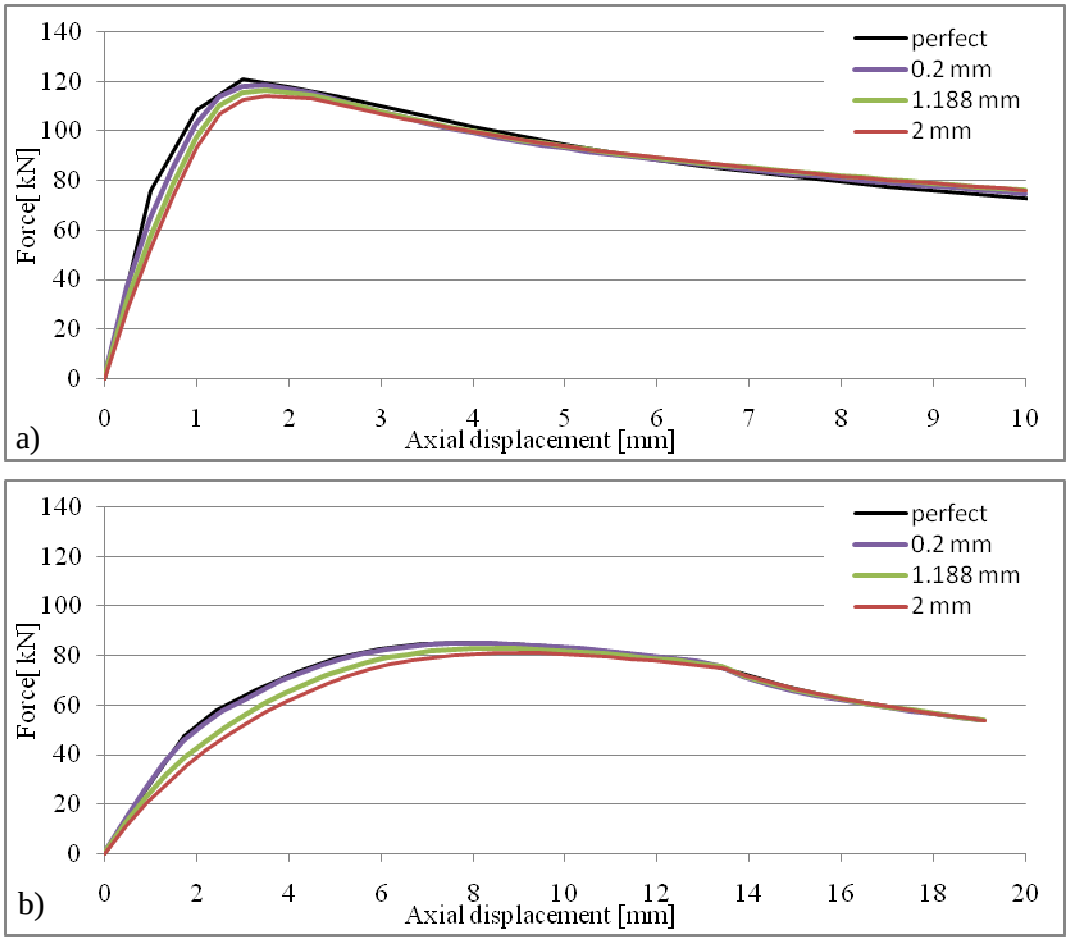

Figure 16. Force – displacement diagram of the (a) 800 mm and the (b)3600 mm Z200/2.0 element

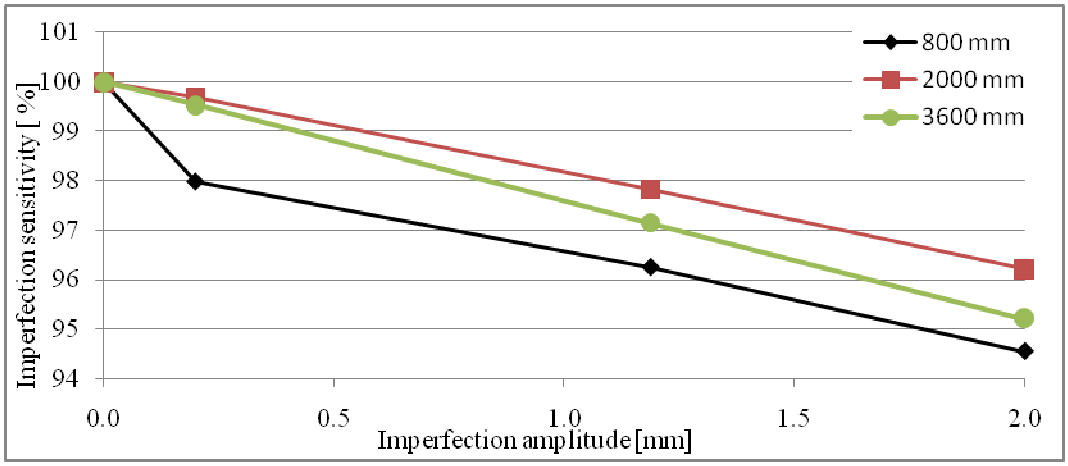

Figure 17. Ultimate load [%] – local web imperfection [mm] relationship

Table 6. Applied local imperfections

Section	Length [mm]	Imperfection type: local	distortional	global	Type and mark	Ultimate load [kN]	Ratio to the perfect model [%]
		Max. deformation [mm]					
Z200/2	800	-	-	-	perfect	120.99	100.00
		2.00	-	-	$e_{0.L1}$	114.40	94.55
		1.18	-	-	$e_{0.L2}$	116.45	96.25
		0.20	-	-	$e_{0.L3}$	118.55	97.98
	2000	-	-	-	perfect	108.62	100.00
		2.00	-	-	$e_{0.L1}$	104.50	96.21
		1.18	-	-	$e_{0.L2}$	106.26	97.83
		0.20	-	-	$e_{0.L3}$	108.27	99.68
	3600	-	-	-	perfect	85.34	100.00
		2.00	-	-	$e_{0.L1}$	81.25	95.21
		1.18	-	-	$e_{0.L2}$	82.91	97.15
		0.20	-	-	$e_{0.L3}$	84.94	99.53

$e_{0.L1}$=web thickness=2 mm,
$e_{0.L2}$=0.006×web height=1.188 mm,
$e_{0.L3}$=web thickness/10=0.2 mm

2.5.2. Effect of distortional imperfections

Distortional imperfections are applied by the magnitude detailed in Table 7. Note, that in these cases the distortional buckling shape contains local imperfections, too, that explains the increase of the ultimate load. Table 7 shows that the reduction in the ultimate load is not significant, between 1-3% and together with the local imperfections the increase can be 7%. This phenomenon calls the attention on the importance of distinction of the buckling modes.

Table 7. Applied distortional imperfections

Section	Length [mm]	Imperfection type: local*	distortional	global (Max. deformation [mm])	Type and mark	Ultimate load [kN]	Ratio to the perfect model [%]
Z200/2	800	-	-	-	perfect	120.99	100.00
		4.04	2.00	-	$e_{0.D1}$	117.33	96.97
		0.40	0.20	-	$e_{0.D2}$	118.62	98.04
	2000	-	-	-	perfect	108.62	100.00
		4.44	2.00	-	$e_{0.D1}$	116.09	106.88
		0.44	0.20	-	$e_{0.D2}$	108.26	99.67
	3600	-	-	-	perfect	85.34	100.00
		4.40	2.00	-	$e_{0.D1}$	82.85	97.09
		0.44	0.20	-	$e_{0.D2}$	85.23	99.87

$e_{0.D1}$=web thickness=2 mm,
$e_{0.D2}$=web thickness/10=0.2 mm
* these imperfections are included in the distortional mode

Difference can be found in the ultimate behaviour, as Figure 18 shows. The initial stiffness is the same, however, the yield mechanism appears at different deformation level and different positions, according to the places of maximum imperfection, as illustrated in Figure 18c. In case of shorter element this effect is not dominant.

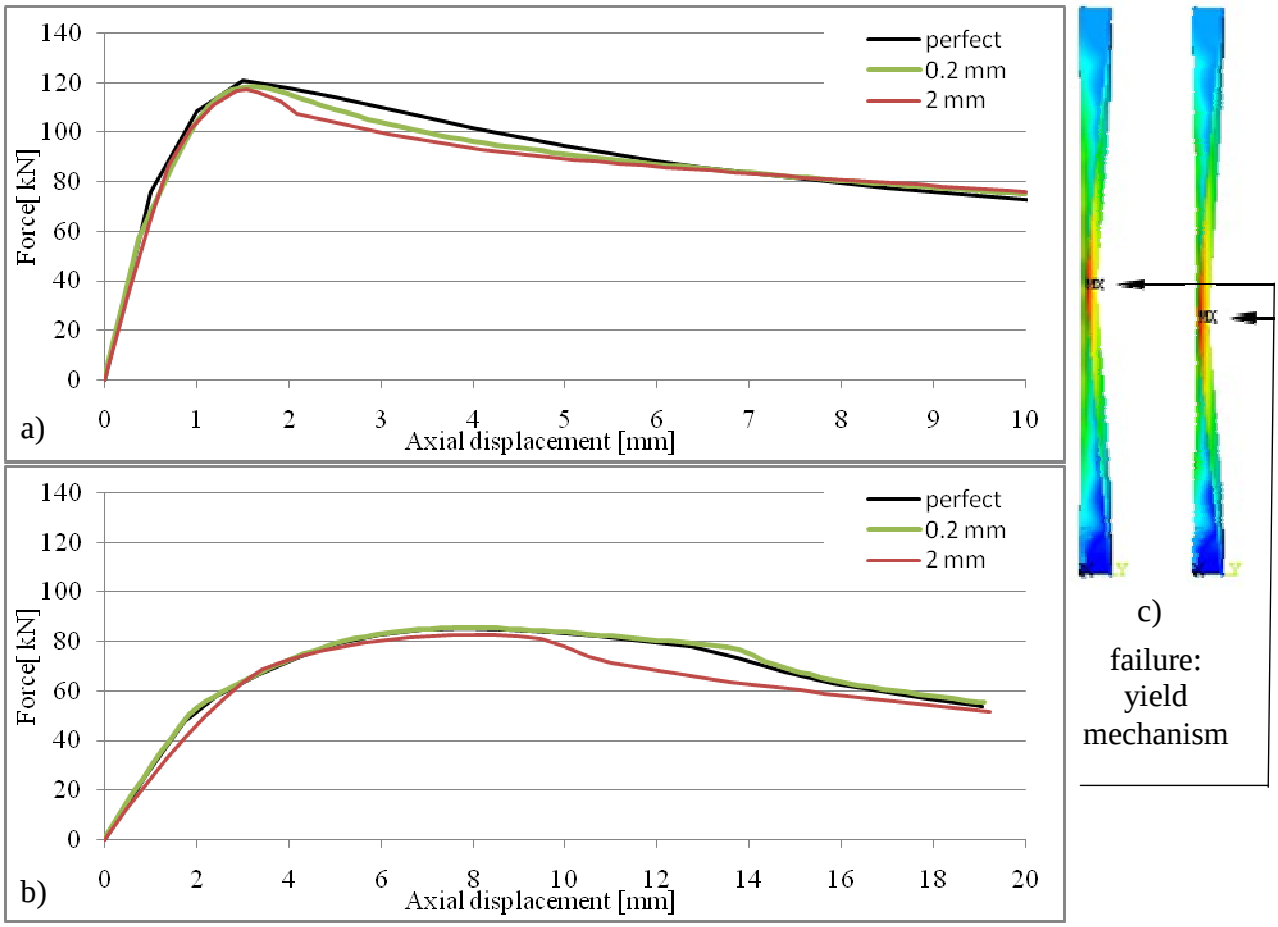

Figure 18. Force – displacement diagram of (a) an 800 mm and (b) a 3600 mm Z200/2.0 element and (c) the places of failure in 3600 mm element

2.5.3. Effect of global imperfections

Two types of global imperfections are analysed. In case of the 2000 and 3600 mm member the imperfections are according to Figure 15 flexural and torsional buckling mode, as it is detailed in Table 8. In case of 800 mm column, two torsional imperfections are applied by torsion in two opposite directions, clockwise and counter-clockwise. In these cases the imperfect geometry contains both local and distortional imperfections beyond the global imperfection, with the maximum deformations detailed in Table 8.

There are differences in the obtained ultimate behaviour in the stiffness of the member, the ultimate load and the post-buckling behaviour, too, as it can be seen in Figure 19 (perfect model is signed by solid line). The ultimate load of imperfect member can be higher than the perfect case, if the applied imperfection does not correspond to the failure mode, see the 2000 mm element in Table 8. In that case the minimum deformation where the yield mechanism can be occurred is not in the same place where the maximum deformation of the global buckling is. This phenomenon results higher resistance. If the imperfection corresponds to the experienced failure in the test program the reduction in the ultimate load is around 10%.

Table 8. Applied global imperfections

Section	Length [mm]	Imperfection type: local*	distortional*	global (Max. deformation [mm])	Type	Ultimate load [kN]	Ratio to the perfect model [%]
Z200/2	800	-	-	-	perfect	120.99	100.00
		1.17	0.99	4.00	$e_{0.G1}$=4 mm tors.	110.95	91.70
		0.39	0.33	1.33	$e_{0.G2}$=1.33 mm tors.	112.99	93.39
		1.32	1.11	4.00	$e_{0.G1}$=4 mm tors.	106.96	88.40
		0.44	0.37	1.33	$e_{0.G2}$=1.33 mm tors.	114.16	94.35
	2000	-	-	-	perfect	108.62	100.00
		15.90	6.28	10.00	$e_{0.G1}$=10 mm flex.	107.17	98.67
		5.30	2.09	3.33	$e_{0.G2}$=3.33 mm flex.	106.60	98.14
		2.48	7.08	10.00	$e_{0.G1}$=10 mm tors.	116.36	107.13
		0.83	2.36	3.33	$e_{0.G2}$=3.33 mm tors.	110.05	101.32
	3600	-	-	-	perfect	85.34	100.00
		17.65	1.02	18.00	$e_{0.G1}$=18 mm flex.	86.87	101.56
		5.88	0.34	6.00	$e_{0.G2}$=6 mm flex.	85.11	99.73
		3.55	10.42	18.00	$e_{0.G1}$=18 mm tors.	79.49	93.15
		1.18	3.47	6.00	$e_{0.G2}$=6 mm tors.	83.44	97.78

$e_{0.G1}$=l / 200,
$e_{0:G2}$=l/600
* these imperfections are included in the global mode

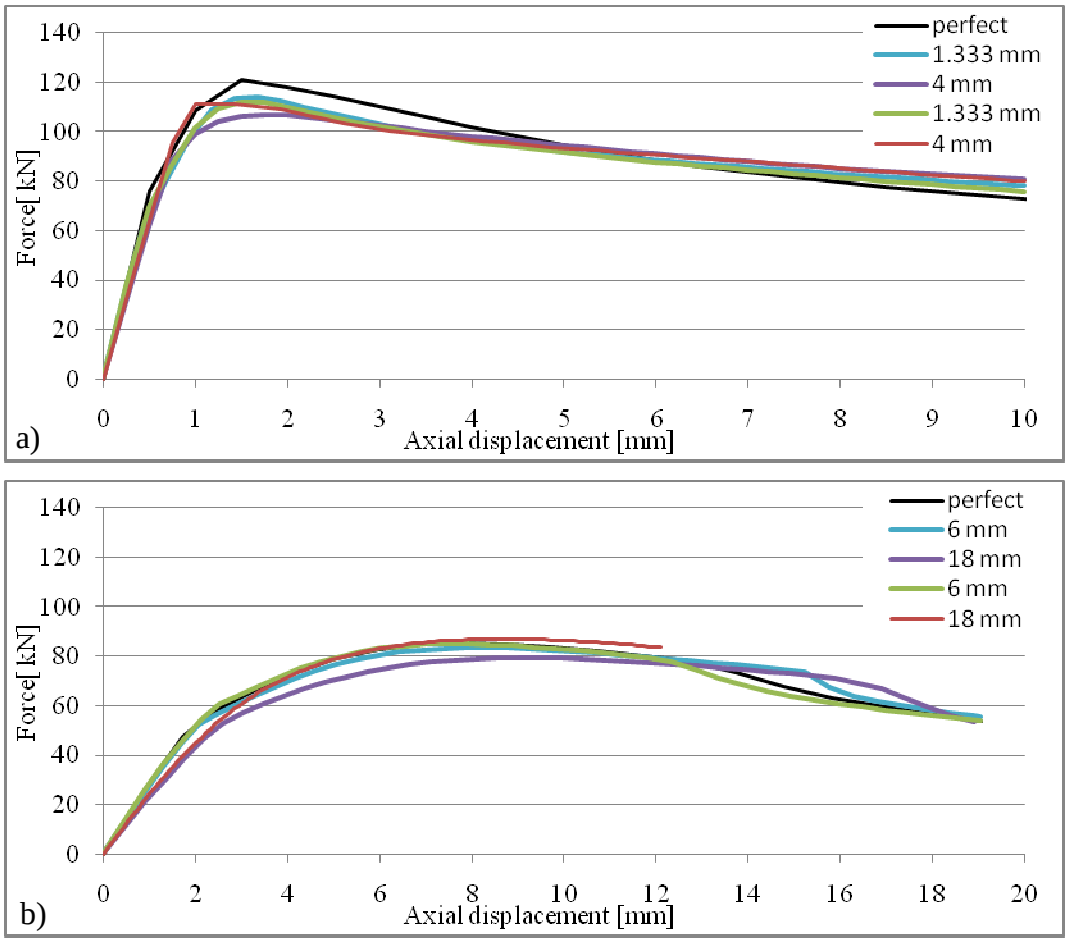

Figure 19. Force – displacement diagram of (a) an 800 mm and (b) a 3600 mm Z200/2.0 element with global imperfections

2.5.4. Illustrative example of the tests

The combination of imperfections is illustrated in the comparison of the measured and calculated nonlinear behaviour of Z13 and Z19 test specimens. In the numerical model three imperfections are applied, as follows: local with 2 mm, distortional with 2 mm and global imperfection with 9 mm maximum deformations. The applied imperfections are compared to the experimentally measured force – displacement diagram in Figure 20. The observed laboratory and calculated virtual test failure modes are the same, as shown in Figure 21.

Further study is concentrated on the extension of the virtual tests to the full test program.

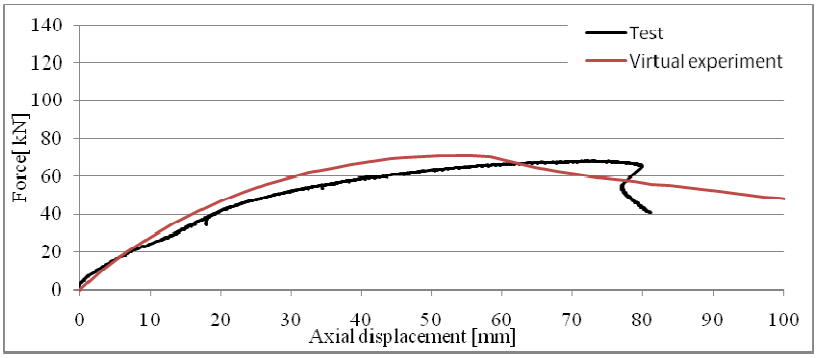

Figure 20. Force – displacement diagram of Z19 tests and virtual experiments

a) 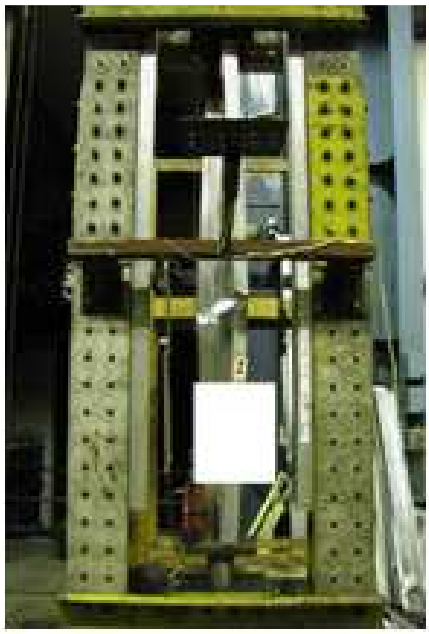 b) 

Figure 21. Failure of the (a) Z13 specimen and (b) the numerical model

2.6 Identification of FE buckling modes of thin-walled elements by using cFSM base functions

2.6.1. Introduction

A second possible approach to the FE buckling mode classification is presented in this chapter. The approach uses a system of modal base functions of Finite Strip Method (FSM) that has been recently proposed by S. Ádány [13], [14].

There are differences between the FE method and FSM disretization of a structural element. The FE method discretizes the model in the cross-section and along the member. The deformation and other parameters are calculated by local base functions of the FE method. The FSM uses local base function in the cross-section only while trigonometric (in this research sinusoidal) functions along the member. This type of discretization determines the limited application of the FSM method; however the pure buckling modes of a pinned-pinned thin-walled prismatic member can be generated. Furthermore these pure modes are available with various half-wavelength.

Mathematically, the proposed base functions are derived by an appropriate transformation of the regular finite strip base functions, by introducing a transformation matrix referred to as a constraint matrix. The definition of the constraint matrix is based on simple mechanical criteria, which ensures that the resulted modal base functions will be able to separate the global, distortional and local buckling modes. In other words the proposed functions can be regarded as possible deformation modes of global, distortional or local buckling. These modal base functions then are used to approximate displacements calculated by a shell-element based finite element buckling analysis, which provides approximate mode identification.

In this chapter the method is explained on a compressed C-section, and parametric studies are carried out and the most efficient parameters (cross-section discretization and number of half-wavelength) are applied on Z-section members.

2.6.2. Modal base functions

The modal base functions for all the typical buckling mode classes (global, distortional, local and other) are presented, which then can be used to approximately describe

displacement functions calculated by a regular finite element analysis. Determination of the modal base functions is in accordance with [13], [14], and can be generated by the following steps: (i) a displacement field identical to the one used in Finite Strip Method (FSM) is assumed, (ii) the characteristic buckling mode classes are defined by mechanical criteria, (iii) the mechanical criteria are implemented to separate the general FSM displacement field, and (iv) the resulting base system is orthogonalized and normalized. The base functions can be interpreted as vectors for matrix operations.

For the analysed member it is assumed that: (i) the analysed member is a column or a beam, (ii) the member is prismatic, (iii) it is supported by two hinges at its ends, (iv) it is loaded by a compressive force (uniformly distributed along the cross-section), (v) its material is linearly elastic, and (vi) it is free from imperfections (residual stresses, initial deformations, material inhomogenities, etc.). The applied global and local coordinate systems and displacements are illustrated in Figure 22.

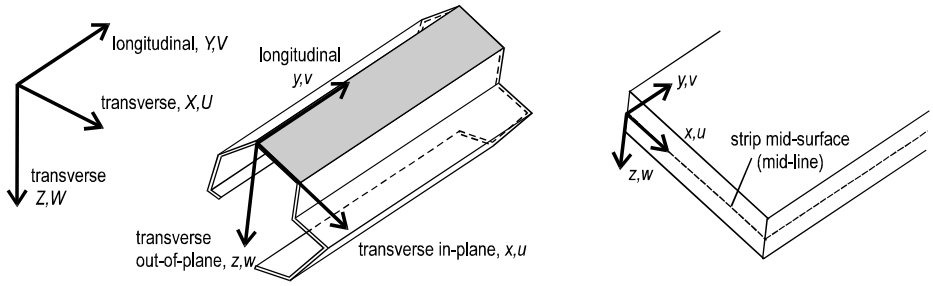

Figure 22. Coordinates, displacements of the FSM base functions [28]

2.6.3. Definition of buckling modes

In the literature and design standards for thin-walled members, it is common to distinguish three characteristic classes of buckling: global, distortional and local. Though there seems to be an agreement on the existence of these mode classes, there is no widely agreed upon definitions for these modes. It is also to mention that there evidently exist modes which neither can be categorized into any of the above three classes nor can be regarded as interaction of these three classes: these modes will be referred simply as other modes and include membrane shear and transverse extension.

Given the lack of commonly adopted mode definition, the one proposed by S. Ádány is applied here [13], [14]. Note this definition can be regarded as equivalent to the one which is implicitly used in Generalized Beam Theory (GBT), see [9], [10]. The separation between global (G), distortional (D), local (L) and other (O) deformation modes can be completed by the application of three mechanical criteria. Table 9 shows the criteria that must be satisfied by the different mode classes [13].

Criterion 1: (a) $\gamma_{xy} = 0$, i.e. there are no in-plane shear strains, (b) $\varepsilon_y = 0$, i.e. there is no transverse extensions, and (c) v is linear in x within a flat part.

Criterion 2: (a) $\nu \neq 0$, i.e. the warping displacement is not constantly equal to zero along the whole cross-section, and (b) the cross-section is in transverse equilibrium.

Criterion 3: $\kappa_{xx} = 0$, i.e. there is no transverse flexure.

Table 9. Mode definition in cFSM [13]

	G modes	D modes	L modes	O modes
Criterion 1	Yes	Yes	Yes	No
Criterion 2	Yes	Yes	No	-
Criterion 3	Yes	No	-	-

2.6.4. FSM assumptions

As it shown in [11], the above mechanical criteria can systematically be applied within the FSM, as it is implemented in the CUFSM software [66]. The application requires lengthy mathematical derivations, which finally lead to a base system where the various deformation classes are separated from each other. Since this separation can also be interpreted as application of appropriate constraints that enforce deformations according to the given criteria, this version of FSM is also termed the constrained FSM, or cFSM.

Since the above mechanical criteria are implemented in FSM, the basic assumptions of FSM are reflected in the resulted base functions/vectors. The implied assumptions can be summarized as follows: (i) the member is modeled by 2D surface elements, (ii) in-plane (membrane) and out-of-plane (plate bending) deformations are allowed, (iii) for the in-plane behaviour a classical 2D stress state membrane is considered, (iv) for the out-of-plane behaviour a classical Kirchoff plate is considered, (v) longitudinal displacement distribution is assumed in trigonometric form (sine-cosine), (vi) the transverse displacement functions are approximated by cubic polynomials, (vii) the displacement functions are expressed as the product of nodal displacements (collected in nodal displacement vectors) and shape functions [8].

2.6.5. cFSM base functions

The above mechanical criteria for mode definition unambiguously define sub-spaces of the original FSM displacement field, (also referred as G, D, L and O spaces), however, these spaces are typically multi-dimensional, and therefore various systems of base functions (that are represented by vectors of nodal displacements, referred simply as base vectors) are possible. Since our aim here is to linearly combine the base functions to approximate FE displacement functions, it is highly advisable to use an orthogonal base system as much as possible. Given the desired deformations a fully orthogonal system does not exist, but orthogonalization within each (G, D, L, O) sub-space is possible. Though orthogonalization can be performed in multiple ways, here one motivated by GBT is followed: the eigenvalue problem is solved for each sub-space one by one, and the resulting eigenmodes (i.e. buckling modes) will be used as orthogonal functions. The resulting modes are presented in Figure 23 for C-shape cross-section and in Figure 24 for Z-shape cross-section. Note, (i) the modes are in basic accordance with the ones used in GBT and (ii) though base functions from different sub-spaces are not fully orthogonal, they are nearly orthogonal.

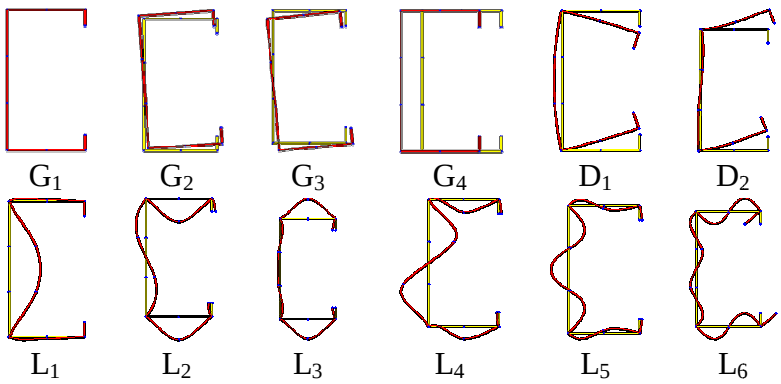

Figure 23. Base functions of C-section: four global, two distortional and first six local modes (displaced/deformed cross-sections)

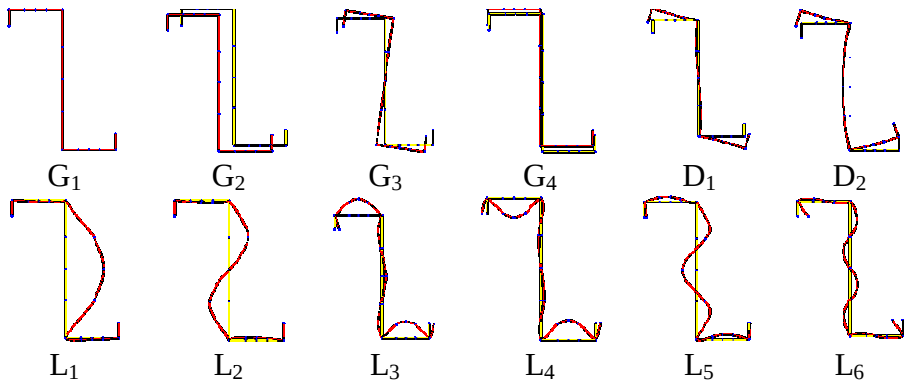

Figure 24. Base functions of Z-section: four global, two distortional and first six local modes (displaced/deformed cross-sections)

Any FSM displacement function, thus buckling modes too, can be written in the following forms:

$$\delta_{transv} = \delta_{CS,t} \sin\frac{m\pi y}{L} \text{ and } \delta_{longit} = \delta_{CS,w} \cos\frac{m\pi y}{L} \tag{5}$$

where L is the member length, m is the number of half-sine-waves considered, while δ_{transv} and δ_{longit} denotes (symbolically) the transverse and longitudinal displacement function, respectively, $\delta_{CS,t}$ and $\delta_{CS,w}$ stand for cross-section transverse and warping displacements, respectively. It is to be observed that (i) the above functions correspond to pinned-pinned and free to warp boundary conditions, (ii) transverse displacements have maximum values in the middle of the beam, and (iii) longitudinal displacement has its maximum value at the beam ends.

As it is proved in [16] the number of cross-section deformed configurations is dependent on the number of strips or nodes, and for an open unbranched cross-section it can be given as follows: G-modes: $n_{G,CS} = 4$, D-modes: $n_{D,CS} = nm - 4$, L-modes: $n_{L,CS} = nm + 2 \times ns + 2$, O-modes: $n_{O,CS} = 2 \times nm + 2 \times ns - 2$, where nm is the number of main cross-section nodes (at the corners) and ns is the number of sub-nodes (or intermediate nodes) located between main nodes.

As Eq. (5) suggests the total number of base functions depends also on the longitudinal shape function, namely: the m number of half-sine-waves considered. Theoretically, m can arbitrarily be selected. Practically, the number is limited to a certain $m_{\max}$ which provides reasonable accuracy for the approximation, and considers the wave lengths $m = 1...m_{\max}$. This means that the total number of base functions considered for a given mode is: $n_M = n_{M,CS} \times m_{\max}$, where subscript M stands for G, D, L or O. Considering that the displacement functions that are to be approximated come from a finite element analysis, they are strongly dependent on the applied discretization. This suggests that the shortest considered sine half-wavelength should be comparable to the size of the applied finite elements.

2.6.6. Normalization

A fundamental feature of eigenmodes is that they can be normalized arbitrarily. Various normalizations are possible. Here the simplest is used, the displacement vectors are normalized in a vector sense (taking advantage that displacement functions are expressed as the product of displacement vectors and shape functions).

$$\boldsymbol{\varphi}^{\mathrm{T}}\boldsymbol{\varphi} = 1 \tag{6}$$

where φ is a base vector. Though this normalization is not perfect (e.g. it is dependent on the applied discretization, the effect of rotations is under-represented, etc.) similar normalization is used in GBT [10] and cFSM [8] with reasonable results.

2.6.7. Approximation of FE displacements

Once the φ cFSM base functions are known, it is possible to approximate any δ_{FE} FE displacement function as a linear combination of the cFSM base functions. The error in this approximation may be expressed as follows:

$$\delta_{\mathrm{err}} = \delta_{\mathrm{FE}} - \sum c\varphi \tag{7}$$

where $\sum c\varphi$ denotes (symbolically) the linear combination. Following the logic used in normalization of the base functions, the minimization will be completed on the error vector (instead of error function), by minimizing the vector norm as follows.

$$\min \sqrt{\mathbf{d}_{\mathbf{err}}{}^{\mathbf{T}}\mathbf{d}_{\mathbf{err}}} = \sqrt{\left(\mathbf{d}_{\mathbf{FE}} - \boldsymbol{\Phi}\mathbf{c}\right)^{\mathbf{T}}\left(\mathbf{d}_{\mathbf{FE}} - \boldsymbol{\Phi}\mathbf{c}\right)} \tag{8}$$

where $\boldsymbol{\Phi}$ is the matrix of orthonormal cFSM base vectors and $\mathbf{c}$ is the vector of unknown combination factors. Expanding Eq. (8), the function to be minimized may be expressed as:

$$\min\ f(\mathbf{c}) = \mathbf{d}_{\mathbf{FE}}{}^{\mathbf{T}}\mathbf{d}_{\mathbf{FE}} - 2\boldsymbol{\Phi}^{\mathbf{T}}\mathbf{d}_{\mathbf{FE}}\mathbf{c} + \mathbf{c}^{\mathbf{T}}\boldsymbol{\Phi}^{\mathbf{T}}\boldsymbol{\Phi}\mathbf{c} \tag{9}$$

which leads to a linear system of equations to be solved for $\mathbf{c}$:

$$\frac{\partial f(\mathbf{c})}{\partial \mathbf{c}} = 0 \rightarrow \boldsymbol{\Phi}^{\mathbf{T}}\boldsymbol{\Phi}\mathbf{c} = \boldsymbol{\Phi}^{\mathbf{T}}\mathbf{d}_{\mathbf{FE}} \tag{10}$$

After calculating the combination factors (elements of $\mathbf{c}$), p_i participation of an individual buckling mode (or base function) can be calculated. Moreover, taking advantage that within the base functions the various buckling classes (i.e. global, distortional or local) are separated, the p_M participation of a class can be expressed as follows:

$$p_i = |c_i| \Big/ \sum_{\mathrm{all}} |c_i| \rightarrow p_M = \sum_{\mathrm{M}} |c_i| \Big/ \sum_{\mathrm{all}} |c_i| \tag{11}$$

where c_i is an element of $\mathbf{c}$ vector, while the M denotes that summation should be performed over all elements of a given mode class.

Once the FE displacement function is expressed by cFSM base functions, the error of approximation can conveniently be measured as the norm of the error vector relative to the norm of the displacement vector (i.e., a "normalized" version of the norm of the error vector)

$$err = \sqrt{\mathbf{d}_{\mathbf{err}}{}^{\mathbf{T}}\mathbf{d}_{\mathbf{err}}} \Big/ \sqrt{\mathbf{d}_{\mathbf{FE}}{}^{\mathbf{T}}\mathbf{d}_{\mathbf{FE}}} \tag{12}$$

2.6.8. Numerical studies on the proposed method

To illustrate the application and capabilities of the proposed identification method, a parametric study is completed on a symmetric lipped channel compressed C-section member. The member length is 1200 mm, the cross-section dimensions are as follows: web height is 100 mm, flange width is 60 mm, lip length is 10 mm, thickness is 2 mm, and the lips are perpendicular to flanges. (Note, the dimensions are for the mid-line, and sharp corners are employed.) Steel material is assumed with a Young's modulus of 210 000 MPa and Poisson's ratio of 0.3. For loading, a uniformly distributed concentric force is applied.

The FE calculations are conducted in Ansys [64], using 4-node, 24-DOF's shell elements in a regular (rectangular) mesh, as shown in Figure 25a. The longitudinal dimension of the

finite elements is constant along the member length, and is defined so that the aspect ratio of all the shell elements is close to 1.

In the numerical studies presented herein the following parameters are considered: (i) cross-section discretization, (ii) minimal wave-length of the base functions, and (iii) different boundary conditions.

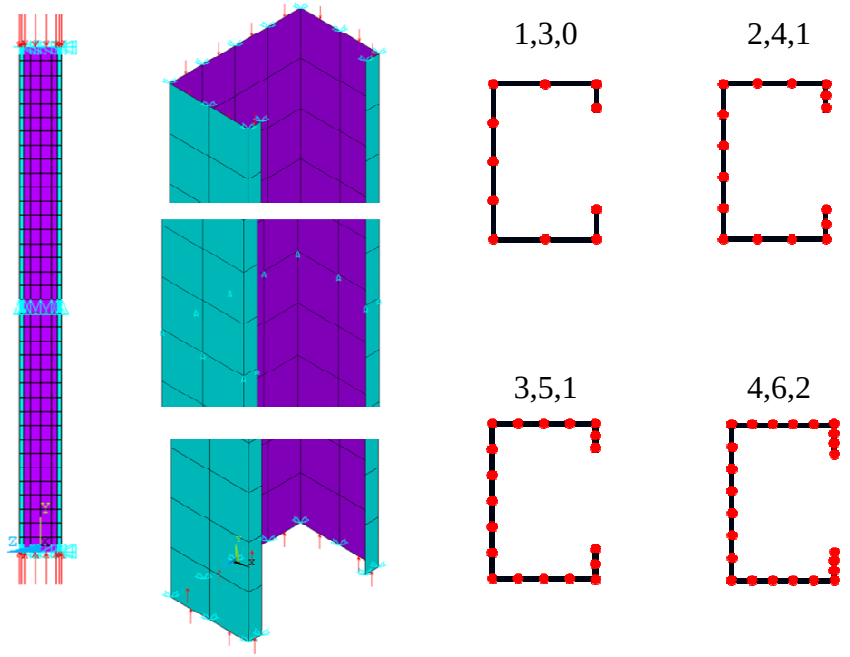

Figure 25. FE model (a) of compressed C-section member and FSM-like boundary condition and (b) cross-section discretization

Four different cross-section discretizations are used, denoted by the numbers of sub-nodes within the flanges, web and lips, respectively. For example, 2-4-1 means that there are 2 sub-nodes in each of the flanges, 4 in the web, and 1 in each of the lips, which totals to 16 nodes or 15 elements in the cross-section. The considered cases are: 1-3-0, 2-4-1, 3-5-1, and 4-6-2, as shown in Figure 25b. The number of cross-section nodes/elements defines the cross-sectional degrees of freedom (DOF's).

Theoretically, the longitudinal distribution of the cFSM base functions can be an arbitrary number of sine half-waves. Practically, the maximum half-wave length to be considered is obviously equal to the member length, while the minimal half-wave length (which must at least be small enough to allow local buckling to develop) is considered as a parameter, expressed as the ratio of the minimal half-wave length and the length of a finite element. In the presented study the following parameters are applied: 1×, 2×, … 6×. (Note, 1× means the smallest cFSM wave-length, hence, the largest number of considered cFSM base functions.)

Finally, five boundary conditions (BC) are investigated. In the case of 'FSM' boundary conditions, the nodes at the supports are restricted from translation, but rotation and longitudinal warping is left free. (Note, this BC exactly corresponds to FSM with a single half-wave along the length; for multiple half-waves FSM-like BC would be different.) The other boundary conditions include 'GF-LP' which represents globally fixed, locally pinned end restraints, 'GF-LF' which corresponds to both globally and locally fixed condition, while in case of 'LW' and 'LF' options only either the web or the flanges are globally fixed and locally pinned (i.e., restrained against translations but free to rotate). The special boundary conditions are shown in Figure 26, while the FSM-like boundary condition presented in Figure 25.

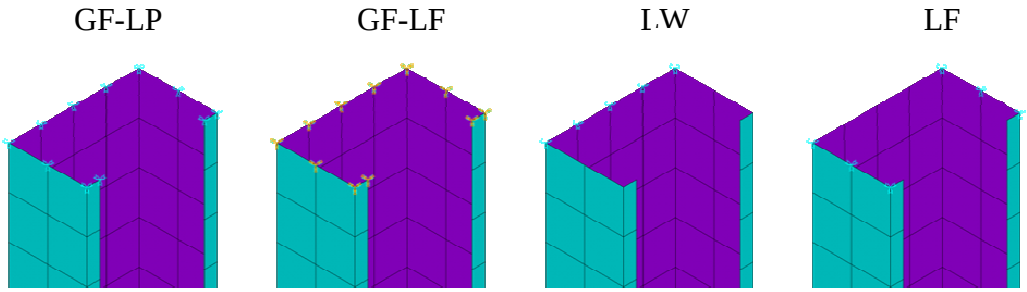

Figure 26. Boundary conditions

In the analysed cases the first 50 FE buckling modes are calculated which covers those modes where the buckling load is smaller than 3 times the minimal (first) buckling load.

The accuracy of the cFSM approximation is measured by means of the error defined by Eq. (12). Then, two more general indicators are determined: (i) the average error of the first n cases (n=1..50), and (ii) the number of cases (among the 50) with an error >5%. These two indicators have been applied to compare the various discretizations, boundary conditions, etc.

Results for selected modes are presented in Table 10: the G, D, L and O participations as well as the calculated error are given for 8 FE buckling modes, calculated by using FSM-like restraints, 3-5-1 cross-section discretization and option 3× for the cFSM minimal wave-length. It is to be noted that option 3× means maximum 21 half-waves in the cFSM base functions (along the member length). The corresponding deformed shapes are presented in Figure 27: both FE solutions and their cFSM approximations are shown. It can be seen there are modes the approximation of which are excellent, as both the deformed shapes and small errors show (e.g. modes #1, #5, #13, #17 and #20). Also, the GDLO participations are in accordance with the engineering expectations: mode #1 is clearly global (flexural-torsional), #17 is dominantly distortional, #13 is local, while #5 or #19 are mixed local-distortional modes. However, there also exist cases with significant errors marked by both the deformed shapes and error values. From the figures it is clear that both #18 and #20 are mixed local and distortional modes, but in neither case the cFSM approximation is not able to reproduce the small local waves. This is even more evident in mode #24, which is clearly a local buckling with 24 longitudinal half-waves, therefore the applied maximum 21 longitudinal waves in the cFSM base functions are simply not enough to properly handle this buckling mode.

Figure 28a shows the effect of FE mesh as well as of the minimal cFSM wave-length. It is clear that (i) finer cross-section discretization significantly enhances the accuracy of approximations, and (ii) higher modes tend to be approximated with larger errors. Considering that higher modes typically include buckling modes with smaller wave-lengths, it can be conlcuded that in some cases the error is caused by the not accurate enough FE displacements. It is obvious, however, that the required minimal mesh density highly depends on how many buckling modes are required to be identified.

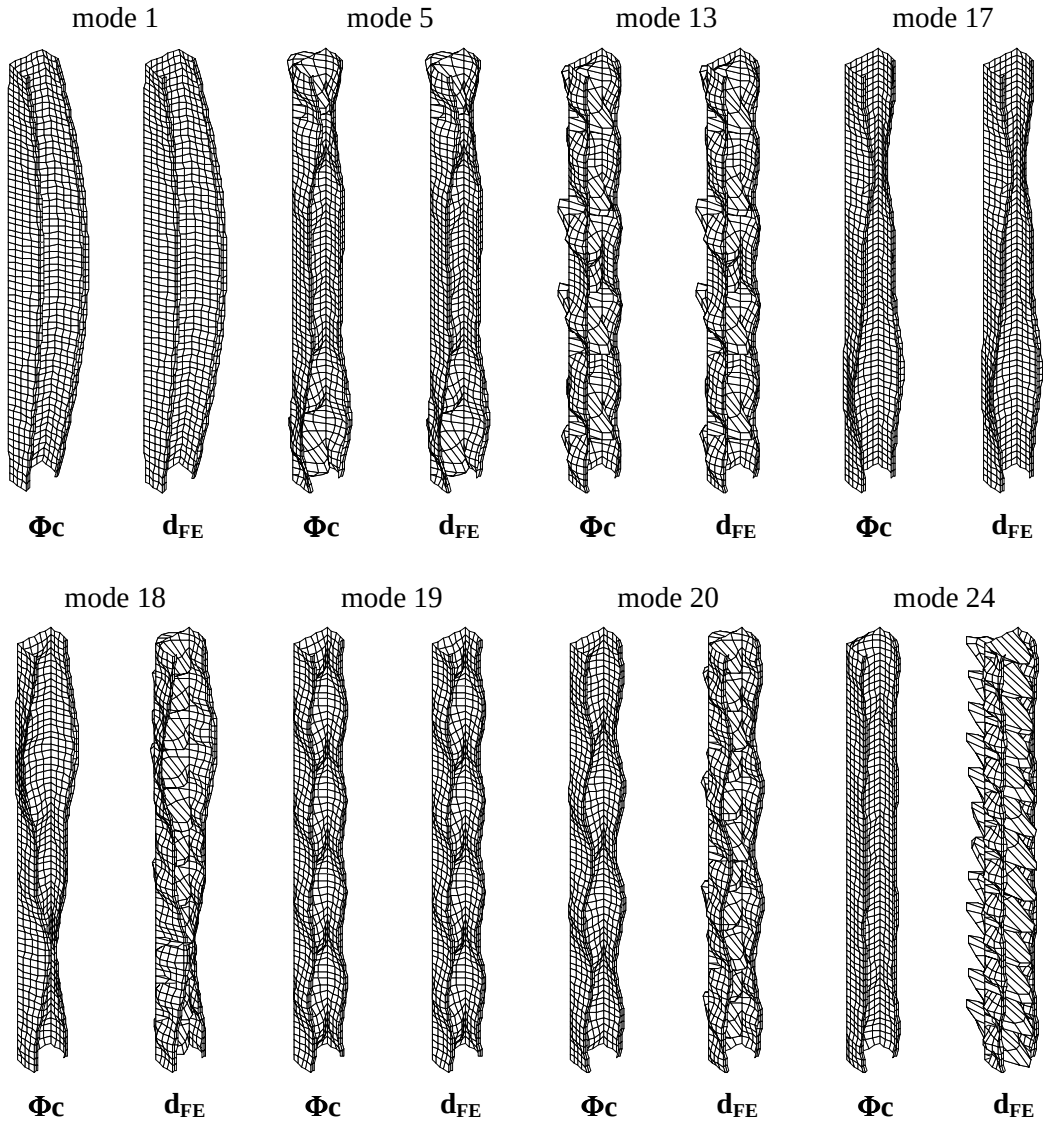

Figure 27. cFSM approximation $\mathbf{\Phi c}$ of FE eigenmodes and $\mathbf{d_{FE}}$ for FE modes [30]

Figure 28b highlights the importance of the number of cFSM base functions considered: allowing for smaller wave-length base functions, the number of erroneous cases decreases, especially in the higher buckling modes where small wave-length-modes likely occur. The results suggest that the minimal wave-length of considered cFSM base functions should not be longer than that of the buckling wave-length of the modes to be identified.

Table 10. GDLO participations in the selected modes

FE mode number	1	5	13	17	18	19	20	24
G	85.9 %	0.5 %	0.2 %	1.3 %	1.1 %	0.6 %	1.1 %	3.3 %
D	5.5 %	38.4 %	8.6 %	82.5 %	64.1 %	26.7 %	36.8 %	28.8 %
L	0.2 %	58.2 %	88.7 %	12.7%	31.4 %	68.1 %	56.8 %	62.3 %
O	8.4 %	2.9 %	2.5 %	3.5 %	3.4 %	4.6 %	5.4 %	5.5 %
error	0.0 %	2.7 %	1.0 %	0.7 %	74.9 %	1.8 %	89.0 %	99.5 %

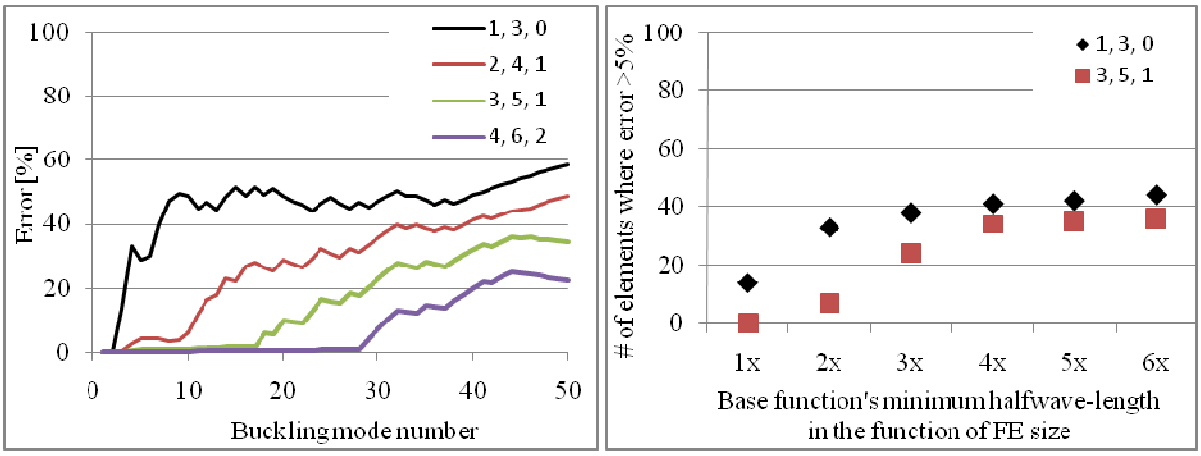

Figure 28. Effect of (a) mesh density and (b) minimal halfwave-length in case of FSM-like boundary condition

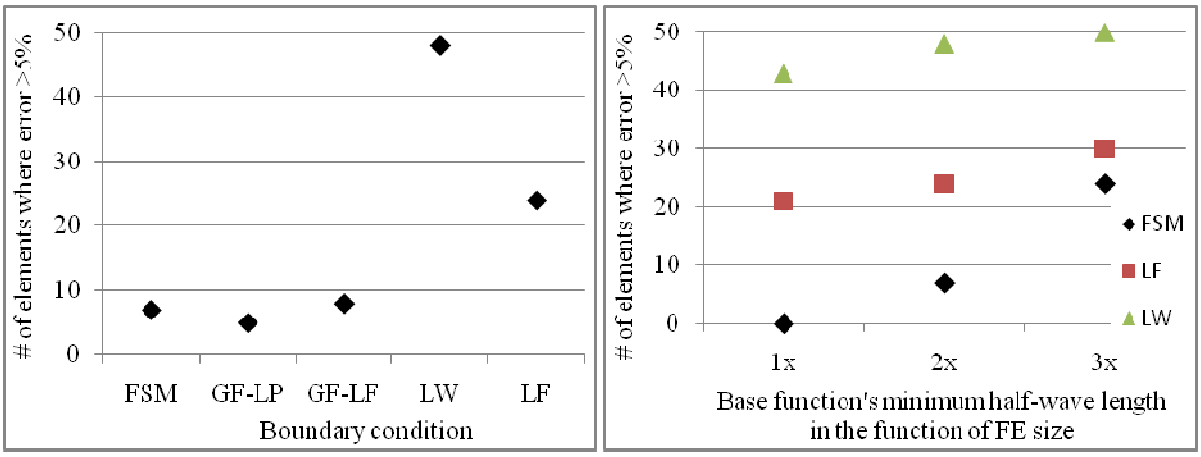

Figure 29. Results of various boundary conditions: (a) error and (b) mesh density

Figure 29 shows that (i) mode identification works properly for various boundary conditions, with the definite exception of LW option where only the web is supported, and (ii) minimal wave-length of cFSM base functions have significant effect on the accuracy. It must be mentioned, however, that increasing the number of cFSM functions (by decreasing the minimal wave-length) may lead to "parasite" solutions: a relatively small error may be achieved while the identification is clearly unrealistic. This phenomenon occurs frequently in the combination of LW and 1×.

Finally, in Figure 30 the proposed approximate identification of the FE solution is compared with the cFSM solution itself (as implemented in CUFSM [8]). Here the model with FSM-like boundary conditions, 3-5-1 discretization, and 3× minimum half-wavelength is employed. A buckling half-wavelength is manually assigned to each of the 50 modes: for some modes e.g. #1, #19 this is readily apparent, for other modes, e.g. #5, more judgment is required and in some cases, no single half-wavelength can be assigned. Buckling stresses and dominant half-wavelengths predicted by the FE and the FSM models are nearly identical, see Figure 30a. Modal participation plot (Figure 30b) highlights some of the additional information contained in the FE models. In the FSM model only one buckling mode can exist at a given half-wavelength, but FE models may have different half-wavelengths superposed (e.g. mode #18), thus the modal participation shows some scatter about the traditional cFSM predictions.

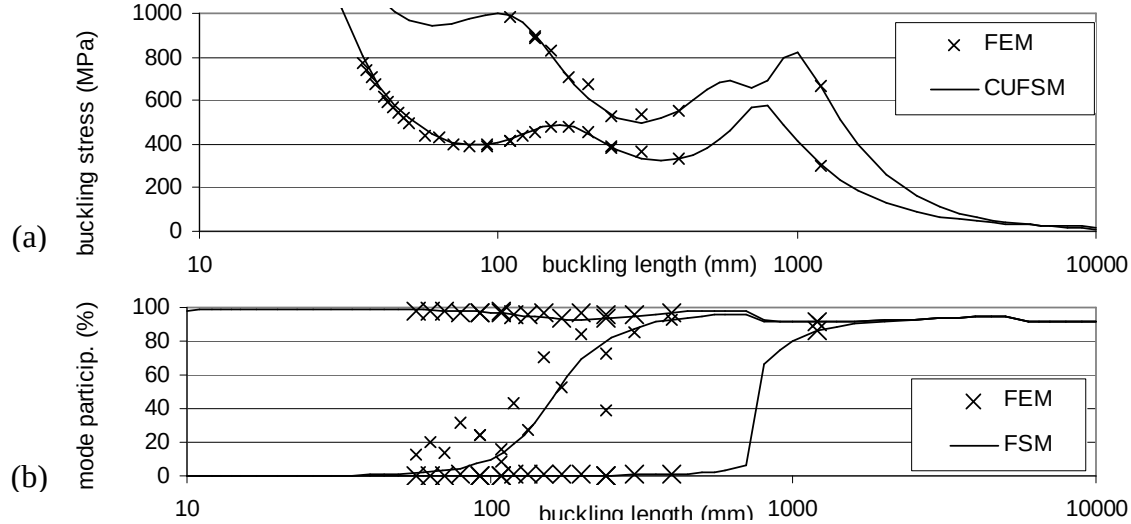

Figure 30. Comparison of (a) buckling stress and (b) mode participation as a function of half-wavelength [30]

An arbitrary buckling mode of a thin-walled member predicted using a shell finite element model may be quantitatively identified in terms of global, distortional, local, or other deformations (mode classes) through the use of the approximate base vectors defined by the cFSM. Through a parametric study of a cold-formed steel lipped channel compressed member the resulting modal identification is shown to be excellent, even for modes with different wavelengths and cross-section deformations (e.g. local and distortional) superposed. Sensitivity to end restraints, finite element (FE) mesh discretization, and the minimum half-wavelength employed for the cFSM base vectors is explored. FE mesh discretization must be fine enough, and the cFSM base vectors must employ a small enough half-wavelength, to adequately resolve the buckling deformations. The identification works with the least error for FSM-like (locally simply supported) boundary conditions, but can be applied to different end restraints, too.

2.6.9. Application of the method on Z-section members

The numerical studies on C-shaped cross sections proved the applicability of the proposed method for compressed C-sections. In this chapter the method is extended to Z-section members with the following specialties: unsymmetrical Z-section, axial force and bending moment and rotational spring support along the member. The examined cases are summarized in Table 11. Three member lengths are analysed: 800, 2000 and 3600 mm according to the test specimens in Chapter 2.2; the cross-section is Z200/2.0: web height is 200 mm, flange widths are 66 and 74 mm, lip lengths are 22.8 mm; thickness is 2 mm, and the lips are perpendicular to flanges. (Note, the dimensions are for the mid-line, and sharp corners are employed.) Steel material is assumed with a Young's modulus of 210 000 MPa and Poisson's ratio of 0.3. Two types of load are applied: a uniformly distributed compression stress at the end sections as concentric compression force and linearly distributed tension-compression stress as bending moment.

Two cross-section discretizations are applied 3-5-1 and 2-4-1 (flange/web/lip) according to Figure 25. In the longitudinal direction various densities are tested. In the first step nearly square finite elements are used. The accuracy of the method can be increased by applying more elements along the member. The numerical examples contain cases where the number of

elements is doubled along the member. However, computational efficiency explains the necessity of less DOF's which leads to the application of longer elements along the member.

Table 11. Numerical example of Z-members

Case	Length [mm]	N	M	Boundary condition	Cross-section division (flange/web/lip)	Number of elements long.	Rotational spring
1	800	Yes	-	FSM	3-5-1	52	-
2	800	Yes	-	FSM	3-5-1	26	-
3	800	Yes	-	LW	3-5-1	26	-
4	800	-	Yes	FSM	3-5-1	26	-
5	800	-	Yes	FSM	3-5-1	52	-
6	800	-	Yes	FSM	3-5-1	78	-
7	2000	Yes	-	FSM	3-5-1	66	-
8	2000	Yes	-	FSM	2-4-1	108	-
9	2000	-	Yes	FSM	3-5-1	66	-
10	2000	-	Yes	FSM	2-4-1	108	-
11	3600	Yes	-	FSM	3-5-1	118	-
12	3600	-	Yes	FSM	2-4-1	54	-
13	3600	-	Yes	FSM	2-4-1	54	Yes

FSM-like and LW boundary conditions are applied as it is shown in Figure 31a, b. To model the restraining effect of trapezoidal sheeting as a usual application of the Z-purlins, rotational restraints at the web-flange intersection are applied (Figure 31c).

In all cases the minimum half-wavelength of the base functions was two times longer of the actual finite element length.

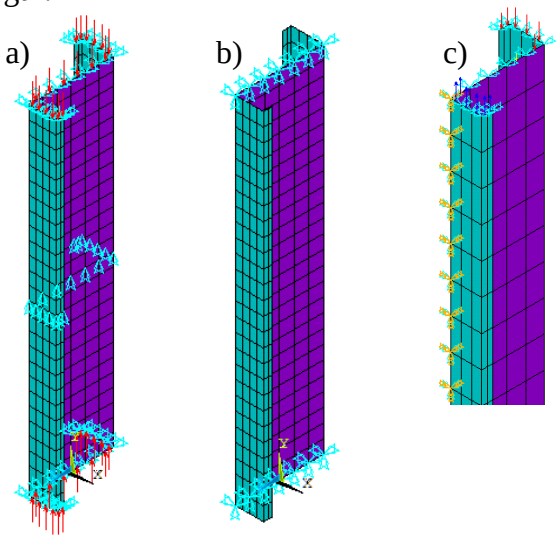

Figure 31. Supports: (a) FSM like, (b) constraints on web and (c) rotational restraints

Using the above-described finite element models, the critical stresses and associated buckled shapes are calculated. The element numbers used in the models varied from 468-2124. Usually the first 100 modes are determined and several are selected for further analysis. These modes are shown in Figure 32-Figure 34 for member lengths 800, 2000 and 3600 mm.

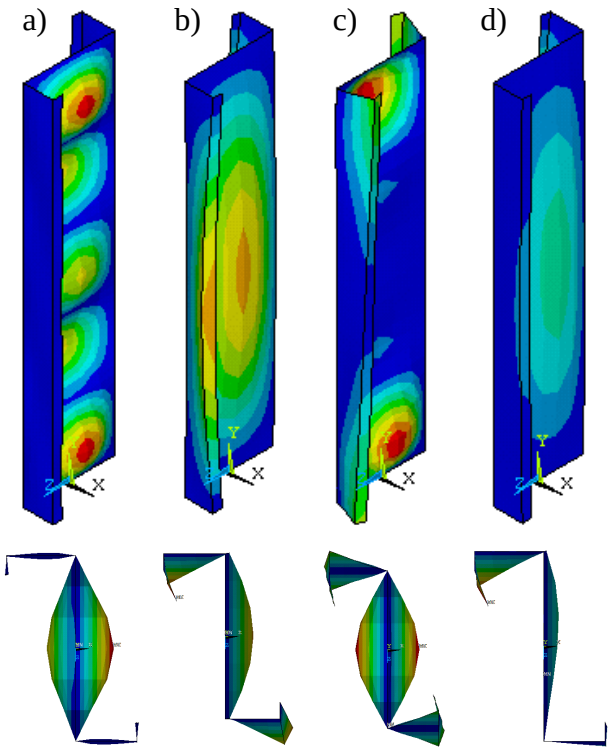

Figure 32. Selected buckling modes of member length 800 mm (top: 3D view, bottom: cross-section deformation): modes 1, 11 of case 1, mode 1 of cases 3 and 6

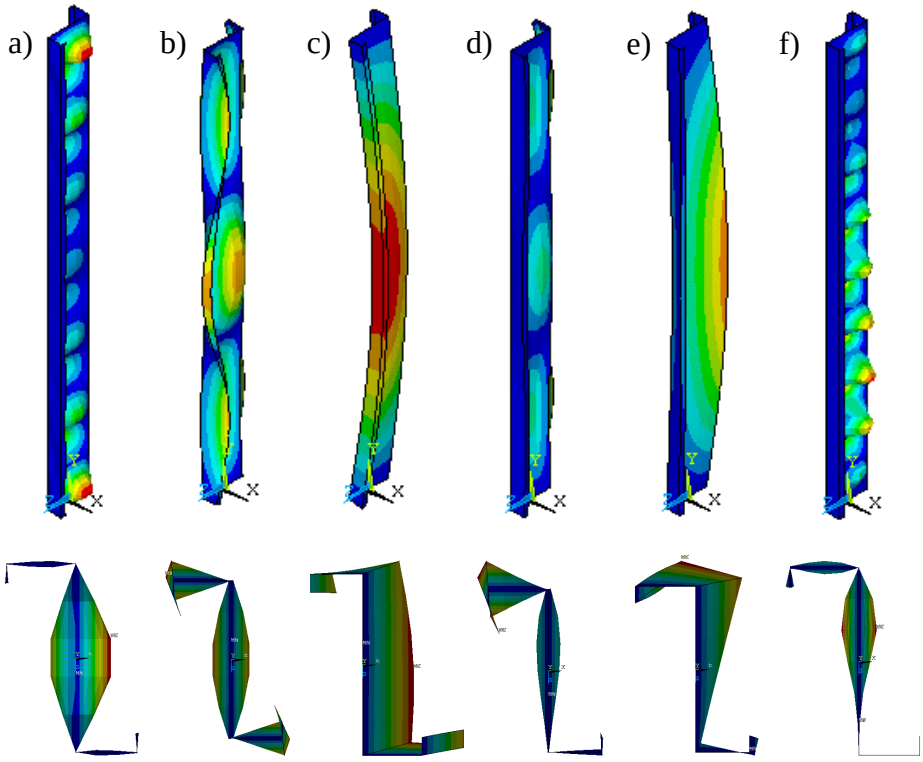

Figure 33. Selected buckling modes of member length 2000 mm (top: 3D view, bottom: cross-section deformation): modes 1, 26, 28 of case 8 and modes 1, 2, 6 of case 9

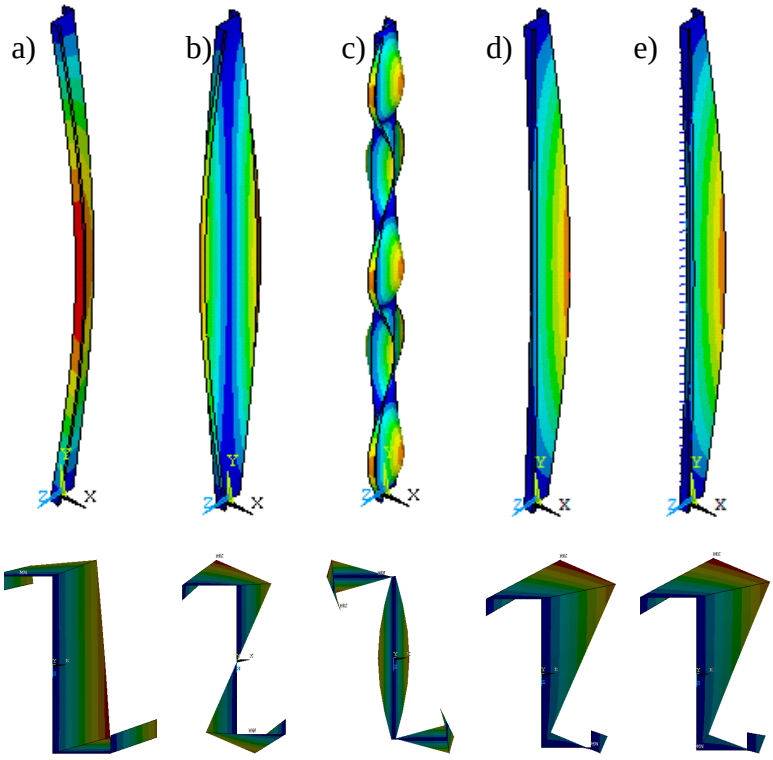

Figure 34. Selected buckling modes of member length 2000 mm (top: 3D view, bottom: cross-section deformation): modes 1, 39, 50 of case 11 and mode 1 cases 12 and 13

By visual inspection of the selected modes one could categorize them as follows. In case of 800 mm member length seemingly local and distortional mode occurs for compression (Figure 32a, b). If supports are applied only on the web nodes the first buckling mode seems to be an interaction of local and distortional modes with high flange deformation at the ends (Figure 32c). The first buckling mode under bending moment is distortional (Figure 32d). The other modes which are not presented here are mainly local modes.

In case of 2000 mm member length some selected modes are presented under compression (Figure 33a, b, c): local, distortional and flexural-torsional global buckling. Under bending moment the selected modes are seemingly distortional, lateral-torsional and local modes (Figure 33d, f, e).

Flexural-torsional and torsional global modes and distortional modes occurs on 3600 mm length member under compression (Figure 34a, b, c). Two cases are analysed for bending moment. Figure 34d shows the first mode without rotational spring and Figure 34e shows the first mode with rotational spring at the tensioned web-flange intersection. The two modes seems to be identical, the critical load factor however is higher for the restrained member.

Performing the mode participation calculation the contribution of G, D, L and O modes can be determined. The results are summarized in Table 12.

The error of approximation is small in the selected cases and matches the preliminary expectations, which means that FSM base functions are able to approximate the analyzed Z-section members with axial force, bending moment and rotational restraints with reasonable accuracy. Only those cases cannot be predicted where deformation occurs at the end sections due to the lack of restraint of the web or the flanges. As far as participations are concerned, it is interesting to notice that even the seemingly pure modes exhibits some coupling.

Table 12. Summary of the results

Length [mm]	Case	Mode	G [%]	D [%]	L [%]	O [%]	Error [%]
800	1	1	0.36	6.68	91.86	1.11	0.01
	1	11	6.08	79.79	10.65	3.49	0.00
	3	1	0.38	3.92	27.88	67.82	36.04
	6	1	1.04	93.43	3.28	2.24	0.01
2000	8	1	0.55	5.38	92.83	1.23	0.02
	8	26	6.08	74.91	14.13	4.88	0.01
	8	28	74.71	13.31	1.79	10.19	0.01
	9	1	1.03	90.62	4.04	4.31	0.01
	9	2	84.56	5.16	1.02	9.26	0.00
	9	6	0.69	6.82	91.28	1.21	0.38
3600	11	1	59.81	1.22	0.25	38.73	0.03
	11	39	27.35	0.65	0.37	71.64	0.09
	11	50	5.49	75.33	12.31	6.87	0.03
	12	1	90.74	0.43	0.09	8.74	0.00
	13	1	89.66	1.55	0.15	8.63	0.00

Based on the results of C-and Z-section members it is proved that the FE buckling mode identification by cFSM base functions works for special conditions of thin-walled prismatic members, such as axial force, bending moment and rotational restraints along the member (effect of trapezoidal sheeting).

The method is capable to distinguish the buckling modes of thin-walled members. As it shown in the previous chapter it is important if pure modes are applied as equivalent geometrical imperfections for nonlinear finite element modeling. The proposed method helps to choose between the interacted buckling modes.

Other application of the method is if the design resistance of a thin-walled member is calculated by the Direct Strength Method (DSM) [22]. The basis of the DSM is the pure buckling modes which can be determined by Finite Strip Method or GBT. The proposed method extends the application of DSM by the analysis of more complex FE models such as discrete boundary conditions along the member or holes in the member that can not be modeled in FSM [31].

The further direction of the research is a development of a user friendly computer program which helps the application of this method.

3. Continuous purlins with overlap

3.1 Introduction

3.1.1. Structural problems

From fabrication and design point of view an optimized solution for continuous purlin systems is that where the length of the purlin is not much higher than the bay space of a steel building and the system is prepared to contain elements with different thicknesses. In this structural arrangement the continuity of purlins is ensured by overlaps over the supporting frames.

There are several structural details at the overlap but the common effect of different details is that the stiffness of the continuous system is disturbed. This means that the structural arrangement significantly effects the distribution of internal forces and deflections, respectively.

Sample overlap zone is shown in Figure 35, where the various components are presented.

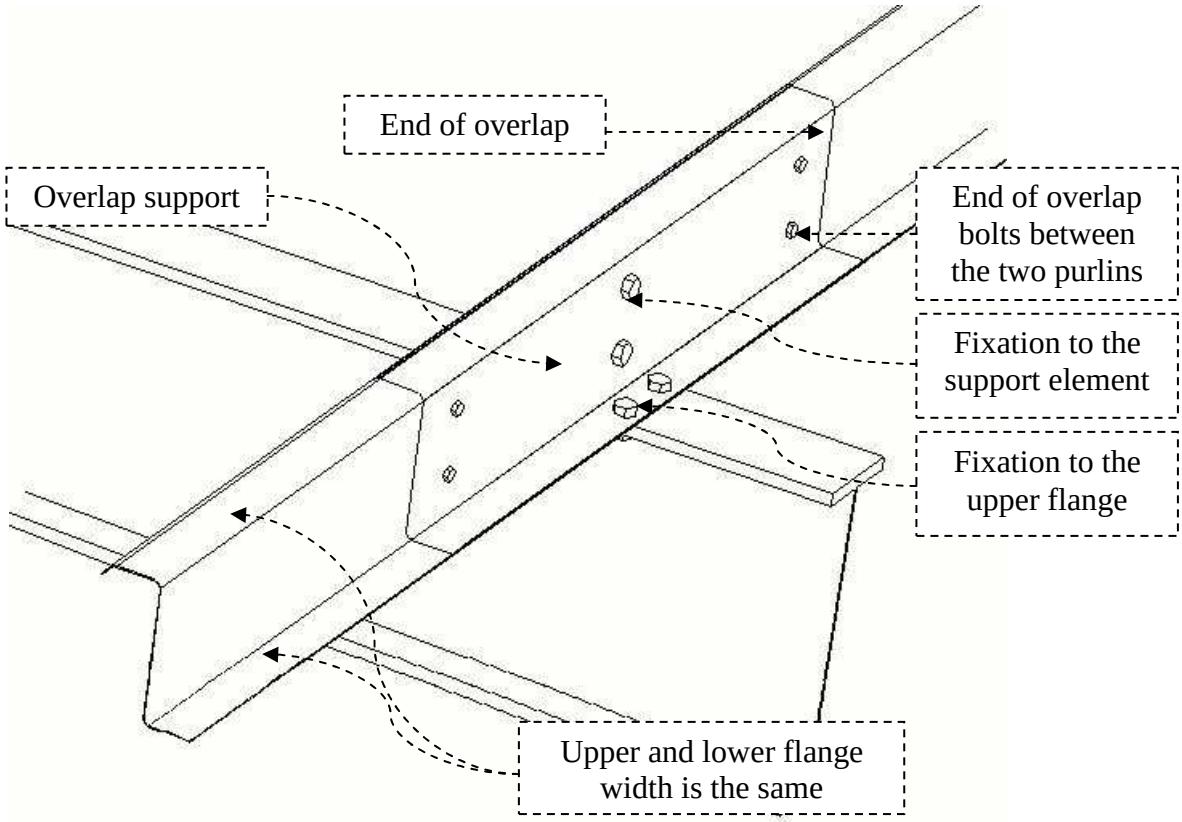

Figure 35. Structural detail of overlap zone

Due to the complex detail of the overlap the design resistance can be defined only by experimental tests according to Eurocode 3 [60], there is no design method to calculate the resistance of the overlap. A series of test is needed for checking (i) the end of overlap due to the different bending moment and shear force ratios, (ii) the middle of the overlap due to the different bending moment and transverse force ratios and (iii) the stiffness of the overlap. The last member of a continuous purlin at the end wall can also be critical for transverse force due to the lack of double section and continuity.

3.1.2. Previous studies

Previous papers on the research of different buckling behaviour modes of single Z-sections due to bending can be found in the literature. These results are used to validate the design methods and to verify finite element models [32], [33]. Nowadays, the published papers are focusing on the connection zone of continuous purlins, especially on the end of the overlap behaviour. Wide range of tests is carried out on overlapped purlins with different overlap length and bolt numbers presented in [34], [35]. The experienced failure modes are followed by finite element analysis in case of end of overlap behaviour [36] and the deformation characteristics of the overlap are also determined in [37] for the specified cases.

The design of single section is handled by standards while the design of the overlap region must be based on experimental tests.

3.1.3. Conclusions on previous studies

On the basis of the existing research studies the following conclusions can be drawn:

- behaviour and design of single Z-sections are well established,
- the overlap region is tested for specific sections and connection types: purlins with different flange widths and bolts at the middle of the overlap (purlin web to the support element on the top flange of the main frame),
- the effect of various overlap length is tested on same spans.

In the investigated literature I did not find:

- experimental results on overlap joints: (i) purlin with same flange widths which results prestressed and tight connection; (ii) bolts between the two purlins in bigger diameter holes; and (iii) connection without bolts at the middle of the overlap,
- design recommendation for the bending moment-shear force interaction at the end of overlap in case of specific overlap length,
- design recommendation for the bending moment-transverse force interaction at the overlap support,
- design recommendation for the transverse force resistance of the last member of the continuous system over the last support,
- finite element model of the specific structural details: end of overlap and overlap support.

3.1.4. Purpose and research strategy

The purpose of the research is to analyse the overlap behaviour of a continuous purlin system in specific cases by experimental tests and calculate the design resistance and interaction curves in the following cases:

- at the end of the overlap the resistance of bending moment and shear force interaction,
- at the middle of the overlap (overlap support) the resistance of bending moment and transverse force interaction,
- at the end support the resistance of transverse force.

Furthermore the overlap rigidity is also intended to be determined from the test results.

The experimental test arrangements and the results are presented in Chapters 3.2 and 3.3. After the evaluation of the results new design methods are proposed in Chapter 3.6.

3.2 Test arrangement and test program

The tests are completed in the laboratory of the Department of Structural Engineering, BME. Altogether 84 experimental tests are completed on Astron Z-purlins [39], [40]. Figure 36 shows the investigated details of a continuous purlin system.

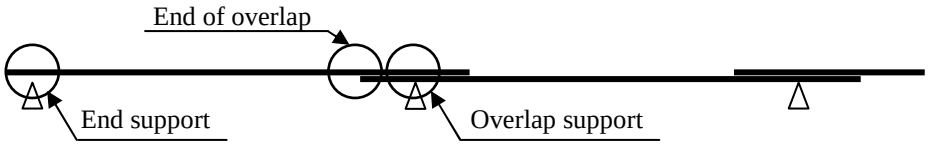

Figure 36. Continuous purlin system and the studied details

A special loading frame is built for the three-point bending tests of the built-up specimens. Four M12 8.8 bolts are used to connect the purlins to each other (in Ø16 mm holes) at the end of overlap. Four purlins (two overlapped) are used for each overlap test. Special element is used for the support which allows the rotation of the end of the Z-sections. A gusset plate (U-channel diaphragm) is used at the support to avoid the web crippling and the distortion of the end of the specimens, as shown in Figure 37. Hat sections on the upper and lower flange of the specimen are used as Vierendeel-type bracing to avoid lateral torsional buckling and distortion of the Z-sections. The hat sections are connected to the purlins by self-drilling screws. The load is applied by MTS hydraulic jack at midspan at the middle of the overlapped zone. I-sections are used as loading members and the load is measured by load cell. Figure 37 and Figure 38 show the load application elements for each test. The load application elements for each test are summarized in Table 14. The deflection at midspan and the relative displacement at the end of the overlap are measured by inductive transducers.

The test programs for the three structural details can be found in Table 13 and Table 14. Two purlin heights, three thicknesses and three spans are tested, to analyse the effect of various bending moment/shear force ratios of the overlap tests. Altogether 72 tests are carried out on overlap zone and 12 tests on the end support. The half-overlap length is strictly 324 and 400 mm in case of 203 and 254 mm height purlins. Each test is repeated two times.

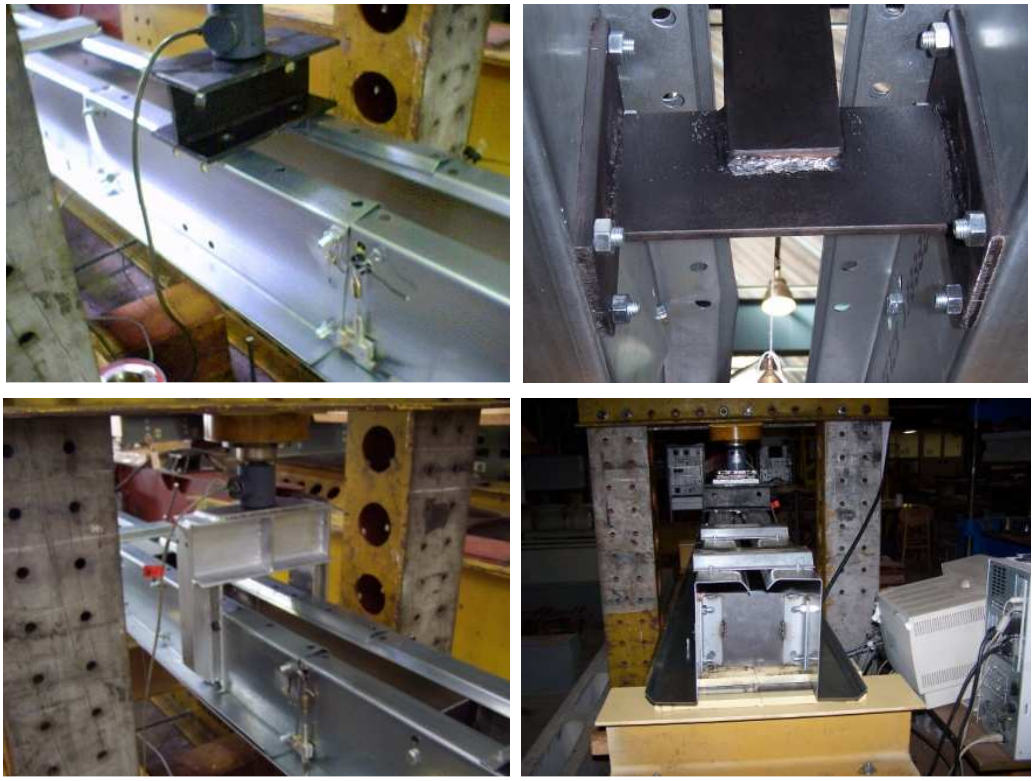

Figure 37. Details of the test: load application elements LA1, LA3, LA4 and end support

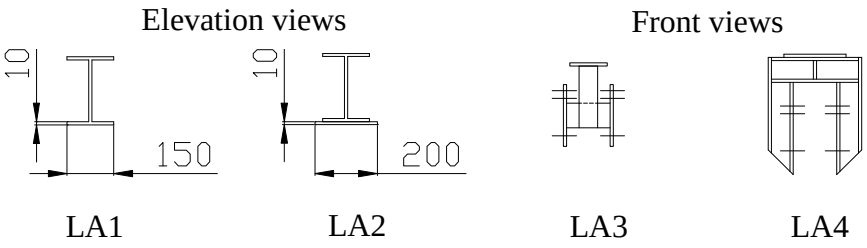

Figure 38. Load application elements

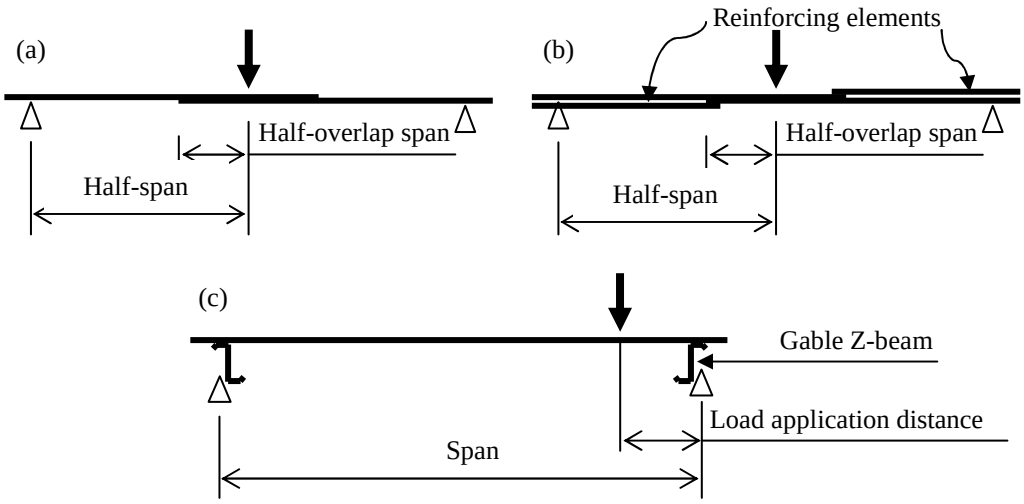

Figure 39. Test arrangements of (a) end of overlap, (b) overlap support tests and (c) end support tests

Figure 40. Test arrangements: reinforced section at the end of overlap and end support tests

Two configurations are used in the overlap tests, as it is shown in Figure 39a and b. The so called normal configuration (Figure 39a) is used to determine the end of overlap resistances. The reinforced configuration (Figure 39b) is used for the overlap support test. In this case reinforcing Z-purlins are applied over the end of overlap to avoid the bending moment and shear force interaction failure at the end of the overlap. The end of the reinforcing element is bolted to the original section at the end of the overlap with the overlap bolts; further connections are solved by self-drilling screws along the member. The stiffness of the overlap joint is determined in the case of normal configuration from the measured deflection and the relative displacement at the end of overlap, respectively.

Table 13. Test program for end of overlap and overlap support test

Test code	Purlin height [mm]	Purlin thickness [mm]	Half-span [mm]	Half-overlap length [mm]	Configuration and load application elements	
					normal (end of overlap)	reinforced (overlap support)
1	203	1.50	2324	324	LA1	LA1
2	203	1.50	1324	324	LA1	LA1
3	203	1.50	574	324	LA3	LA1
4	203	1.90	2324	324	LA1	LA1
5	203	1.90	1324	324	LA1	LA1
6	203	1.90	574	324	LA3	LA1
7	203	2.67	2324	324	LA1	LA1
8	203	2.67	1324	324	LA1	LA1
9	203	2.67	574	324	LA4	LA1
10	254	1.70	2324	400	LA1	LA1
11	254	1.70	1324	400	LA1	LA1
12	254	1.70	574	400	LA4	LA1
13	254	2.00	2324	400	LA1	LA1
14	254	2.00	1324	400	LA1	LA1
15	254	2.00	574	400	LA4	LA1
16	254	2.67	2324	400	LA1	LA1
17	254	2.67	1324	400	LA1	LA1
18	254	2.67	574	400	LA4	LA1

Table 14. Test program for end support tests

Test code	Purlin height [mm]	Purlin thickness [mm]	Span [mm]	Load application distance [mm]	Number of tests and load application elements	
1	203	1.50	1148	148	2	LA2
2	203	1.90	1148	148	2	LA2
3	203	2.67	1148	148	2	LA2
4	254	1.70	1148	148	2	LA2
5	254	2.00	1148	148	2	LA2
6	254	2.67	1148	148	2	LA2

Figure 39c shows the configuration of end support tests. In this case no overlap is applied, the resistance is determined on two purlins connected by hat sections on the upper and lower flanges. The test program for end support test is shown in Table 14. Altogether 12 tests are completed on the six various sections.

3.3 Test results

3.3.1. Failure modes

In the first step the pure failure modes of a continuous purlin system are defined as detailed in Table 15. The observed failure modes are mainly interacted failures of those pure modes; these are presented in Table 16. The main results are the ultimate loads and the ultimate behaviour which are identified by photos and the measured force-displacement curves in

Figure 41 - Figure 51. The failure modes are observed at the limit point of the force-displacement curves.

The overlap stiffness results are evaluated in Chapter 3.5.4 from the end of overlap tests where reinforcing elements are not used.

The typical failure is plate buckling (yield mechanism) at the end of the overlap (Mode 1). In several cases distortional buckling is experienced in the case of large spans (Mode 2) while pure web crippling failure is experienced in the case of the overlap support tests (Mode 3). Pure shear failure of the bolts at the end of the overlap is occurred only for overlap support tests where reinforcing elements are used (Mode 4). In the case of short specimens shear failures are also occurred in the interaction with plate buckling (Mode 9).

Table 15. Pure failure modes

Mode description
Plate buckling (yield mechanism) at the end of the overlap
Distortional buckling
Web crippling at load application point
Lip plate buckling
Shear buckling
Shear failure of the bolts at the end of the overlap
Web crippling at the end support
Failure of the gable Z-section beam

In most cases pure modes did not observed, instead interacted modes are evolved which resulted the ultimate behaviour. After the limit point is reached in the descending branch of the behaviour plastic plate buckling (yield mechanism) in the case of end of overlap tests (Mode 6 and Mode 8) and web crippling in the case of overlap support tests (Mode 7) are observed.

Table 16. Definition of observed failure modes

Failure mode #	Mode description
Mode 1	Plate buckling (yield mechanism) at the end of the overlap
Mode 2	Distortional buckling
Mode 3	Web crippling at load application point
Mode 4	Shear failure of the bolts at the end of the overlap
Mode 5	Interaction of plate buckling at the end of the overlap and web crippling at the load application point
Mode 6	Interaction of plate buckling at the end of the overlap and distortional buckling
Mode 7	Interaction of distortional buckling and web crippling at load application point
Mode 8	Interaction of plate buckling at the end of the overlap and lip plate buckling
Mode 9	Interaction of plate buckling at the end of the overlap and shear buckling
Mode 10	Web crippling at the end support
Mode 11	Interaction of web crippling at the end support and failure of the gable Z-section beam

In the case of overlap support test the web crippling failure at overlap support could not be reached for long specimens even though the reinforcing at the end of the overlap. In those cases end of overlap failures are experienced.

The typical failure of end support test is web crippling (Mode 10). For small web height and large thickness the failure occurred in the gable Z-section beam by large deformation.

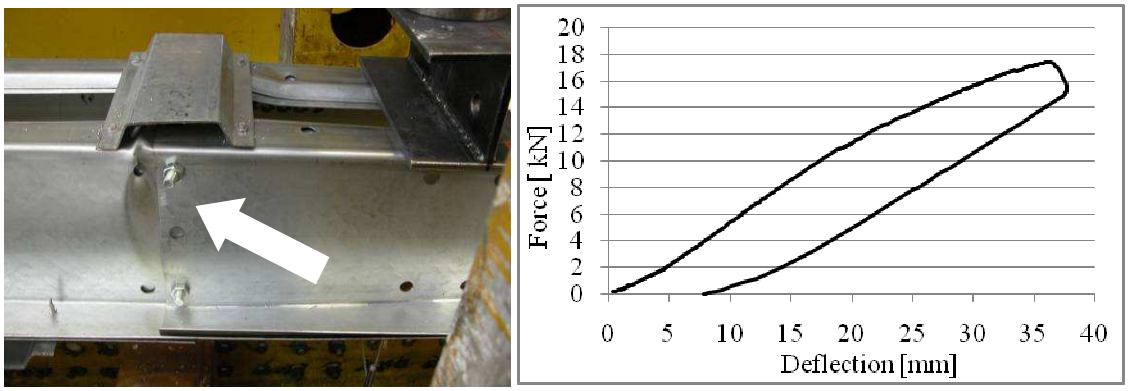

Figure 41. Plate buckling (yield mechanism) at the end of the overlap (Mode 1)

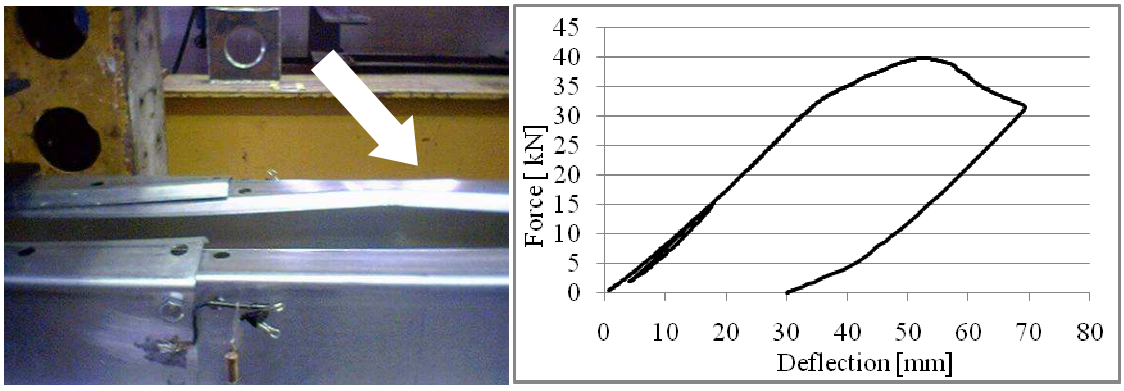

Figure 42. Distortional buckling (Mode 2)

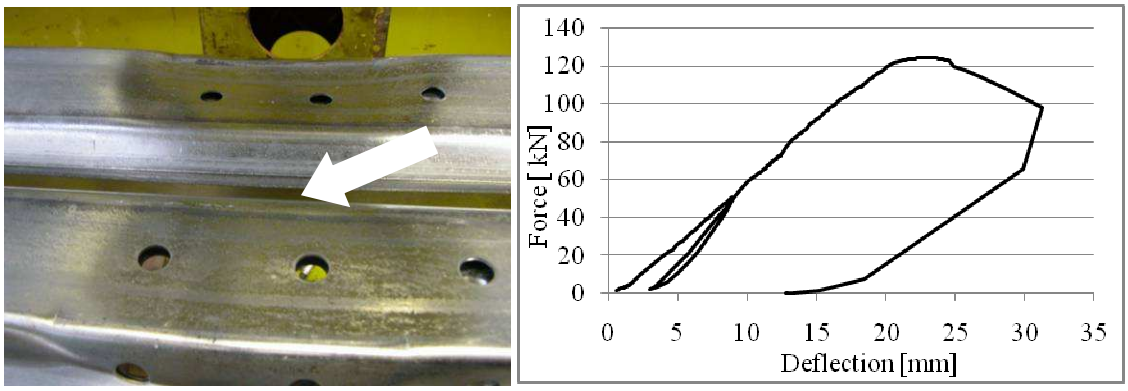

Figure 43. Web crippling at load application point (Mode 3)

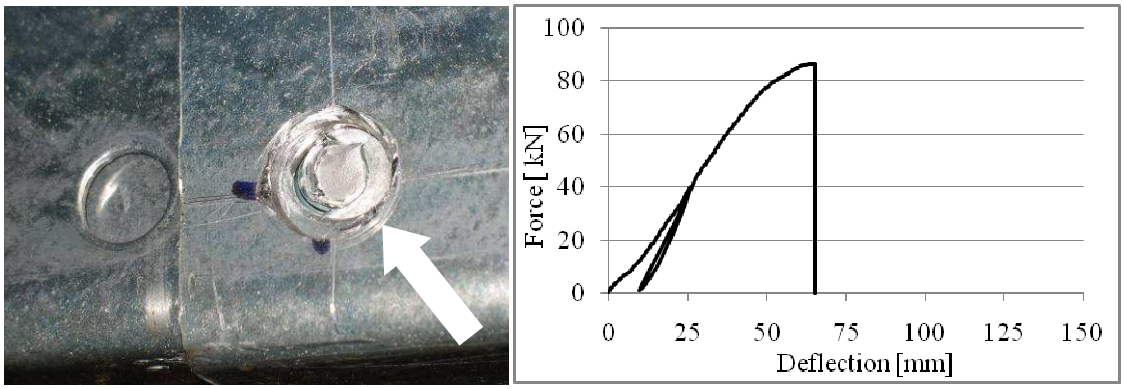

Figure 44. Shear failure of the bolts at the end of the overlap (Mode 4)

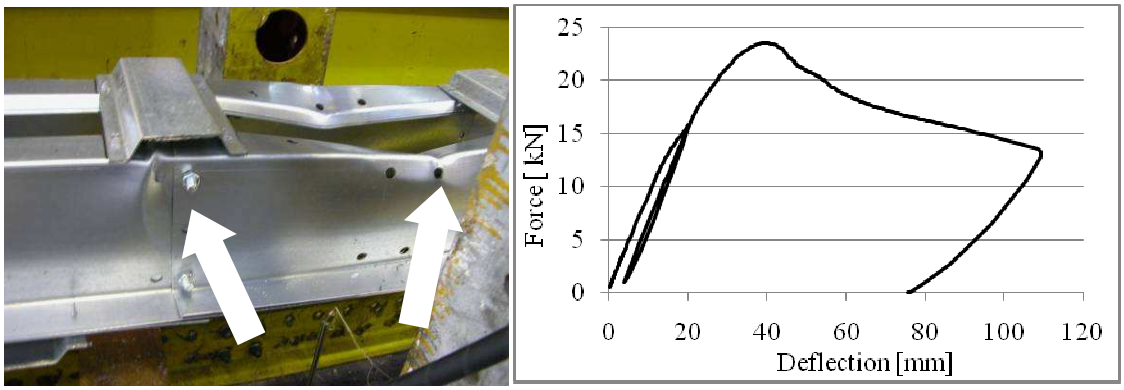

Figure 45. Interaction of plate buckling and web crippling (Mode 5)

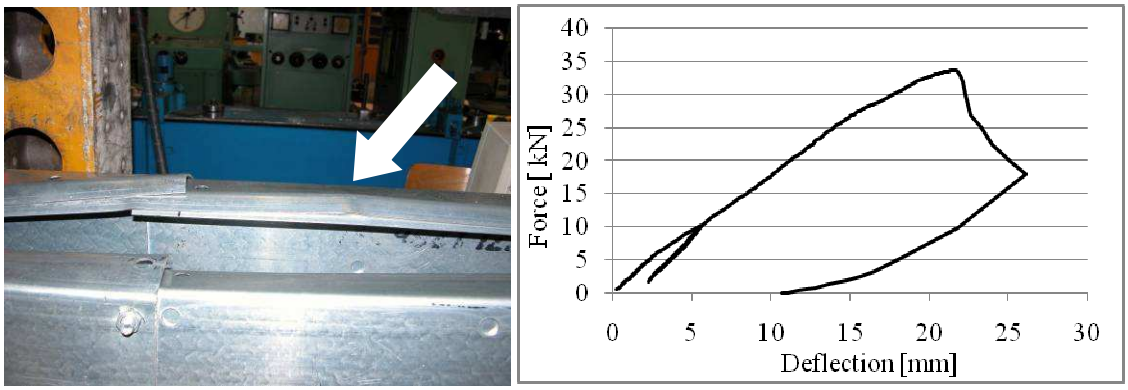

Figure 46. Interaction of plate buckling and distortional buckling (Mode 6)

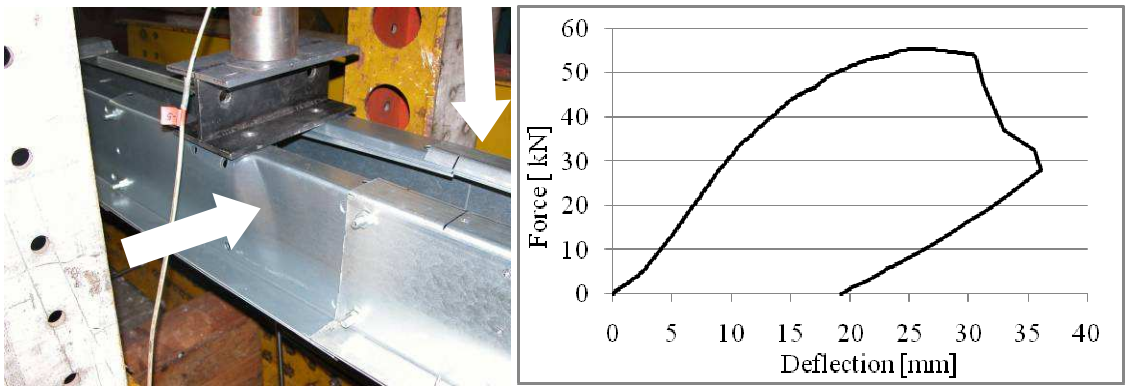

Figure 47. Interaction of distortional buckling and web crippling (Mode 7)

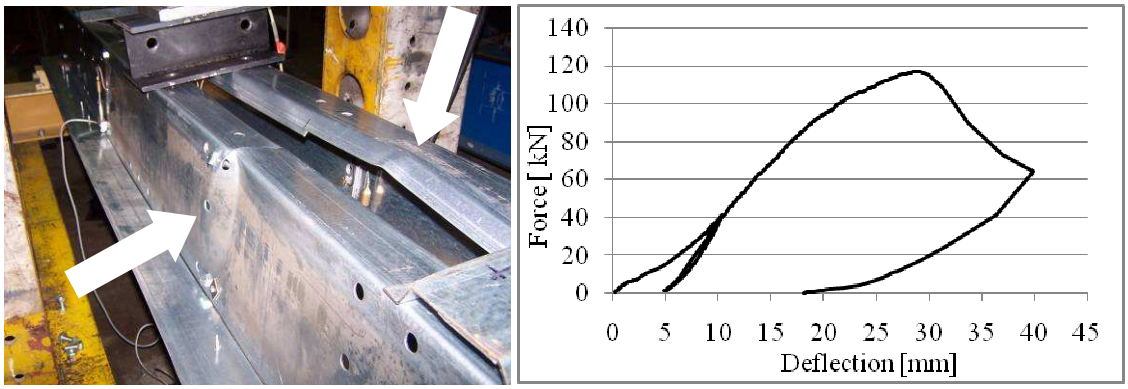

Figure 48. Interaction of plate buckling and lip buckling (Mode 8)

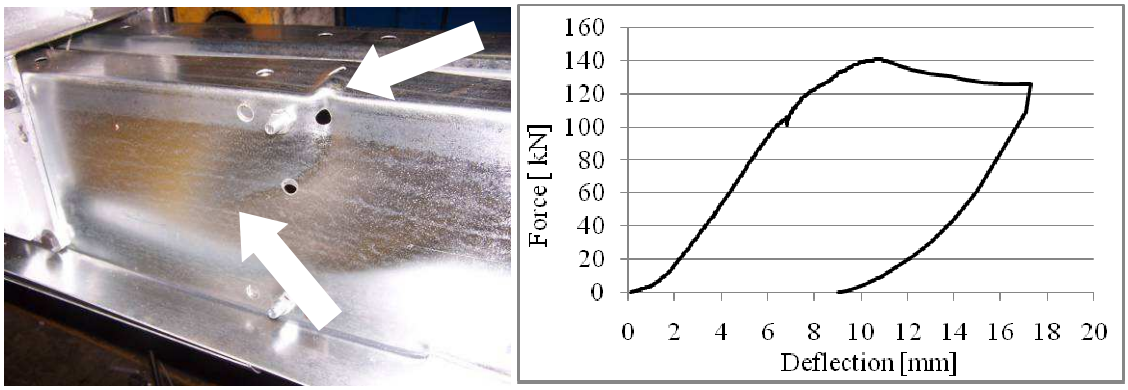

Figure 49. Interaction of plate buckling and shear buckling (Mode 9)

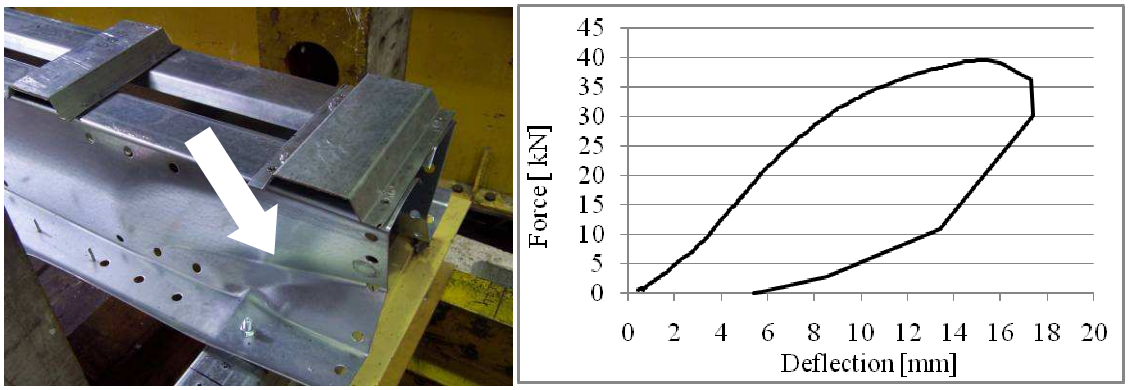

Figure 50. Web crippling at the end support (Mode 10)

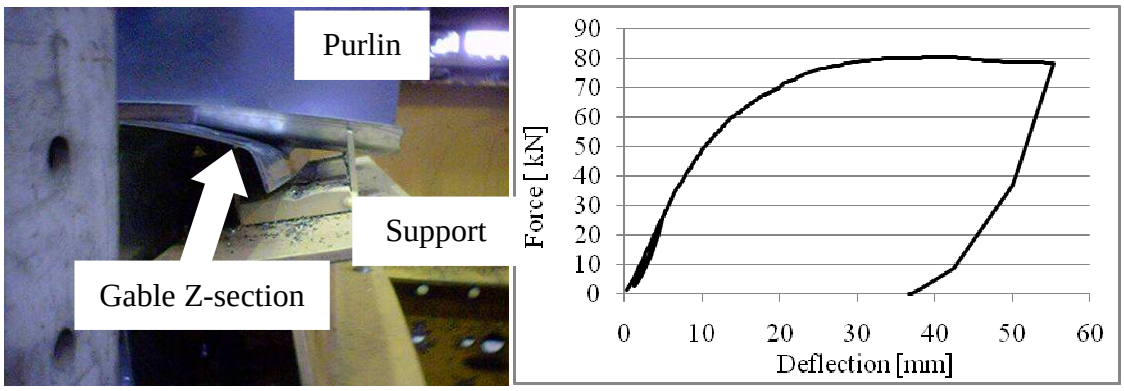

Figure 51. Interaction of web crippling failure of gable Z-section beam (Mode 11)

3.3.2. Results of bending moment and shear force interaction at the end of the overlap

The results of bending moment and shear force interaction are presented in Table 17 with the measured ultimate loads and the observed failure modes. The design values are also presented in the last two columns, the calculation method is presented in Chapter 3.5.

Each test is repeated two times, the average deviation is 1.76 % and the maximum is 4.18 %, which shows good correlation between the test results.

Table 17. Results of bending moment and shear force interaction at the end of the overlap

Test code	P_{test} [kN] 1	2	Failure mode [#] 1	2	$M_{Rd.test.overlap}$ [kNm]	$V_{Rd.test.overlap}$ [kN]
1	17.38	16.80	1	8	7.25	3.63
2	33.67	33.57	6	6	7.13	7.13
3	91.37	94.73	6	1	4.94	19.74
4	23.30	24.34	2	2	10.61	5.30
5	46.39	42.67	1	2	9.91	9.91
6	140.57	137.71	9	9	7.74	30.98
7	39.67	39.34	2	8	16.84	8.42
8	78.22	77.76	6	6	16.62	16.62
9	249.22	258.36	9	9	13.52	54.08
10	27.70	28.13	6	6	11.66	6.06
11	50.81	48.98	6	6	10.01	10.83
12	159.46	168.29	9	9	6.19	35.57
13	39.46	39.17	1	1	15.10	7.85
14	80.67	74.50	6	6	14.31	15.49
15	227.95	231.31	9	9	7.98	45.84
16	59.78	62.02	1	1	24.39	12.68
17	116.90	103.94	8	1	21.24	22.98
18	371.52	371.71	9	9	13.46	77.34

3.3.3. Results of transverse force at the end support

The results of transverse force are presented in Table 18 with the measured ultimate loads and the observed failure modes.

In these cases the average deviation is 1.04 % and the maximum is 1.52 %.

Table 18. Results of transverse force at end support

Test code	P_{test} [kN] 1	2	Failure mode [#] 1	2	$R_{Rd.test}$ [kN]
1	32.21	32.59	10	10	11.98
2	40.18	39.46	10	10	15.44
3	81.74	80.35	11	11	30.09
4	40.87	40.06	10	10	15.30
5	52.73	54.36	10	10	18.62
6	78.00	75.96	10	10	27.91

3.3.4. Results of bending moment and transverse force interaction at the overlap support

The results of bending moment and transverse force interaction are presented in Table 19 with the measured ultimate loads and the observed failure modes in the first five columns.

In these cases the average deviation is 1.40 % and the maximum is 3.16 %.

Table 19. Results of bending moment and transverse force interaction

Test code	P_{test} [kN] 1	2	Failure mode [#] 1	2	$M_{Rd.test.midspan}$ [kNm]	$R_{Rd.test}$ [kN]
1	23.50	23.71	5	5	11.64	10.02
2	37.61	35.98	7	5	10.34	15.61
3	51.46	51.38	3	3	6.26	21.82
4	31.56	32.90	1	1	16.68	14.35
5	55.42	55.97	7	3	16.42	24.80
6	83.66	79.73	3	3	10.44	36.37
7	50.98	51.62	1	6	25.40	21.86
8	85.39	84.70	6	2	23.99	36.24
9	153.19	148.32	3	3	18.44	64.25
10	37.90	37.68	3	3	19.07	16.41
11	56.76	54.96	3	7	16.06	24.25
12	70.97	72.26	3	3	8.92	31.09
13	52.39	52.13	7	3	24.24	20.86
14	80.69	85.10	3	3	21.91	33.09
15	103.70	99.62	3	3	11.65	40.59
16	81.10	86.35	6	4	40.50	34.85
17	127.97	124.58	3	3	34.80	52.56
18	161.66	170.26	3	3	19.83	69.08

3.4 Material tests

Tensile tests are carried out on specimens cut out from each purlin type. Altogether 30 tests are completed (six different sections and 5 specimens from each web). The detailed stress – strain curve, plotted by an MTS 80 hydraulic test equipment, can be found in [39]. The test results are summarized in Table 20 for the 203 mm height purlins and in Table 21 for the 254 mm height purlins. The definition of R_{eH} and $R_{p0.2}$ are detailed in Chapter 2.2.6.

Table 20. Material test results for the 203 mm height purlin

Material test specimen	Specimen thickness	width [mm]	Yield stress $R_{p0.2}$	R_{eH} [N/mm^2]	Ultimate stress [N/mm^2]	Ultimate strain [%]
811	1.53	20.43	-	413	451	37.5
812	1.52	20.42	-	417	460	36.5
813	1.52	20.42	-	414	461	36.5
814	1.52	20.46	-	413	458	38.0
815	1.51	20.34	-	411	459	35.5
821	1.88	20.13	401	-	514	31.0
822	1.88	20.14	403	-	516	32.5
823	1.89	20.19	402	-	515	33.0
824	1.88	20.17	394	-	512	32.5
825	1.89	20.15	398	-	515	30.5
831	2.67	20.50	-	407	460	35.5
832	2.67	20.56	-	411	462	38.0
833	2.68	20.55	-	412	462	36.5
834	2.68	20.48	-	412	461	37.5
835	2.67	20.49	-	414	464	35.0

Table 21. Material test results for the 254 mm height purlin

Material test specimen	Specimen thickness [mm]	width	Yield stress $R_{p0.2}$ [N/mm^2]	R_{eH}	Ultimate stress [N/mm^2]	Ultimate strain [%]
1011	1.71	20.24	-	401	448	37.0
1012	1.71	20.21	-	400	451	38.0
1013	1.70	20.24	-	405	455	38.0
1014	1.70	20.26	-	404	453	36.0
1015	1.71	20.19	-	404	451	36.5
1021	2.00	20.21	435	-	533	35.0
1022	2.00	20.20	446	-	536	34.0
1023	2.01	20.18	443	-	533	32.0
1024	2.00	20.16	431	-	534	30.5
1025	1.99	20.19	443	-	538	31.5
1031	2.64	20.54	-	429	542	31.0
1032	2.63	20.54	-	425	542	30.0
1033	2.64	20.53	-	424	540	31.5
1034	2.64	20.57	-	427	543	31.0
1035	2.65	20.54	-	427	535	34.5

3.5 Evaluation of test results

3.5.1. Evaluation method

The test results of each test series are evaluated to define the standard design resistances according to the Eurocode 3 [60]. The adjusted values R_{adj} of the test results are calculated according to Eq. (1) and (2), where the nominal yield stress is $f_{yb} = 390$ N/mm^2.

The mean, the characteristic and the design values are calculated as:

$$R_m = \frac{R_{adj,1} + R_{adj,2}}{2},\ R_k = \eta_k \times R_m \text{ and } R_d = \eta_{sys} \times \frac{R_k}{\gamma_M} \tag{13}$$

The observed failure is yielding failure so $\eta_k = 0.9$, or it can be between $\eta_k = 0.8...0.9$ if the observed failure is local stability, depending on effects on the global behaviour. In this case $\eta_k = 0.9$ is used because the observed local buckling during the tests was in the elastic range which was followed by postcritical behaviour and the final collapse was due to the developed yield mechanism (means that the local buckling in the elastic range did not cause sudden global failure). The design value is calculated by $\eta_{sys} = 1$ because the test conditions followed the applied solution, and $\gamma_M = 1$ partial factor is applied (according to [59]).

The bending moment and shear force resistance of one section is calculated as

$$M_{Rd} = \frac{R_d \times L_{M/V}}{4} \text{ and } V_{Rd} = \frac{R_d}{4} \tag{14}$$

where $L_{M/V}$ is the M/V ratio at the end of the overlap.

3.5.2. Design resistances of end of overlap and overlap support tests

On the basis of the calculated test based resistances the design values of the interaction of bending moment and shear force at the end of the overlap are shown in Figure 52a. The

interactions of bending moment and transverse force at the overlap support are shown in Figure 52b.

The tendencies of the end of overlap resistances of various sections and thicknesses can be seen clearly. In case of longer span, shear is relatively small, thus, it is reasonable to assume that the measured bending resistances can be considered as pure bending resistances. In other cases the erosive effect of shear (on the bending resistance) can be seen. Since even a relatively small bending has non-negligible effect on the shear resistance, the pure shear resistance cannot be accurately predicted from the performed tests. In case of support resistance tests failure was intended to occur at the support, involving two overlapping cross-sections. The major actions: bending and (concentrated) transverse force. In certain cases, especially tests with longer spans, failure occurred at the end of overlap region, thus, in these cases the measured bending/reaction force values do not represent real failure values.

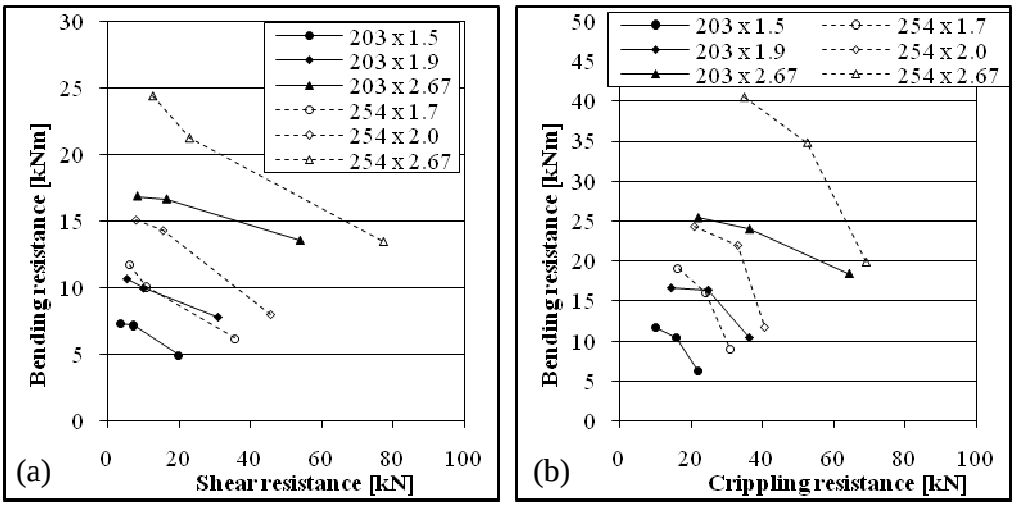

Figure 52. Interaction curves: (a) end of overlap resistance (b) overlap support resistance

3.5.3. Design resistances of end support tests

The test based design results of web crippling are shown in Figure 53. The design values show the same tendencies, the crippling resistance is nearly linearly depending on the plate thickness and it is not dependent on the purlin height.

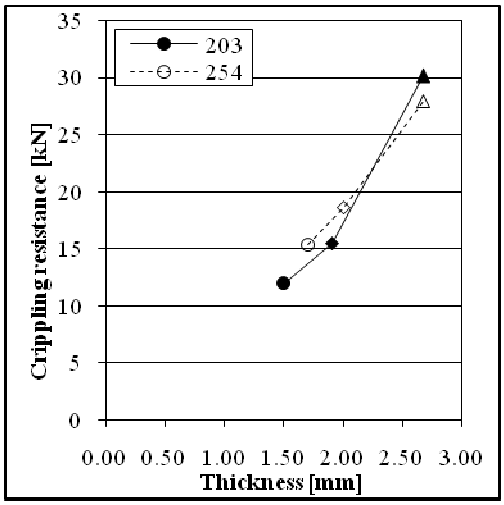

Figure 53. Design resistances of end support test

3.5.4. Overlap stiffness

The overlap stiffness is determined by two ways: (i) the evaluation of relative displacements at the end of the overlap and (ii) the comparison of calculated and measured deflections. A beam model of the test setup is built, where the second moment of inertia of the specimens is used for the whole length and the overlap stiffness is described by a k_s rotational spring, as shown in Figure 54b. The rotational spring k_s is calibrated to reach the same deflection – at the level of serviceability limit state ($M_{SLS} = 0.7M_{Rd.t}$) – as observed during the tests. The results are summarized in Table 22 and shown in Figure 55 for the two section heights. There are two cases where the deviation of the results from the tendencies is significant, which represents the uncertain behaviour of the overlap.

The overlap stiffness can be also defined as the inertia factor of the single section as published in [36]. The α_s inertia factor is the modification factor of the second moment of inertia of the single section in the overlapped region (Figure 54c). This inertia factor is also determined at the level of serviceability limit state. The inertia factor is determined only for the longest specimens according to the span/section ratio of the referred paper.

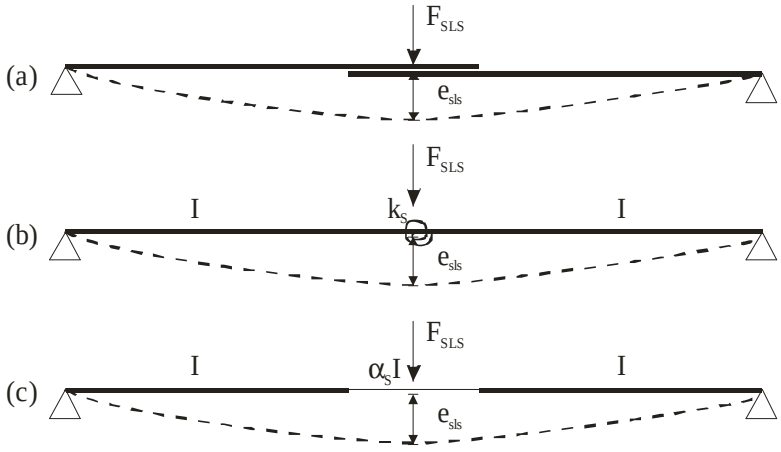

Figure 54. Stiffness definition of the overlap: (a) measured deflection at serviceability limit state (b) rotational spring (c) inertia factor

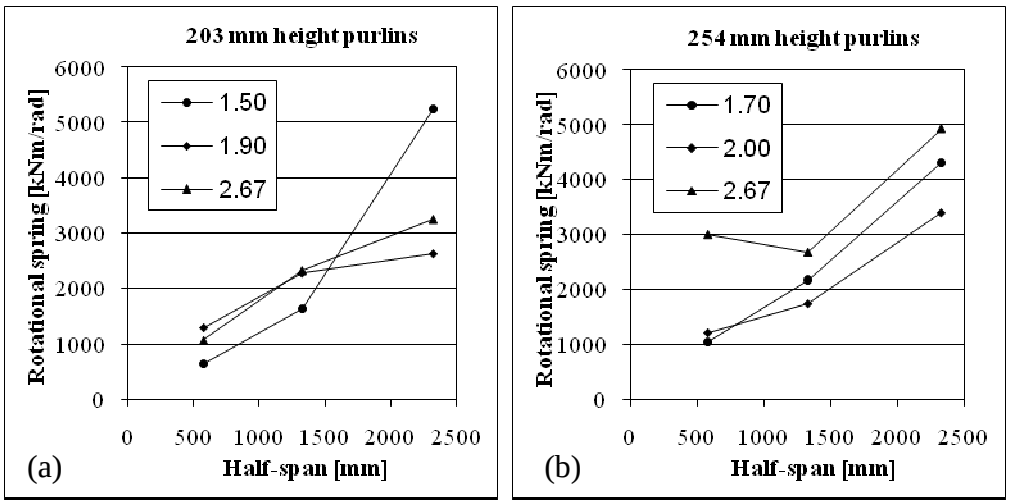

Figure 55. Overlap stiffness: (a) 203 mm and (b) 254 mm height purlin

Table 22. Results of initial overlap rigidities

Test code	Purlin height [mm]	Purlin thickness [mm]	Half-span [mm]	Overlap stiffness	
				k_s [kNm/rad]	α_s
1	203	1.50	2324	5250	0.68
2	203	1.50	1324	1640	-
3	203	1.50	574	650	-
4	203	1.90	2324	2625	0.45
5	203	1.90	1324	2275	-
6	203	1.90	574	1288	-
7	203	2.67	2324	3245	0.40
8	203	2.67	1324	2325	-
9	203	2.67	574	1070	-
10	254	1.70	2324	4300	0.46
11	254	1.70	1324	2175	-
12	254	1.70	574	1050	-
13	254	2.00	2324	3400	0.43
14	254	2.00	1324	1750	-
15	254	2.00	574	1220	-
16	254	2.67	2324	4925	0.39
17	254	2.67	1324	2675	-
18	254	2.67	574	3000	-

The calculated inertia factors are compared to the results of [36]. The paper contains test results for different overlap length/section height ratios and structural details (number and position of bolts). The section height and the span differ from the current tests and the fact that there “perfect-fit” bolts are used. The similar tests, however, can be compared to the results of the paper. The presented research in [36] found that in case of small overlap length/section height ratio the inertia factor is less than 1.

In [36] a prediction formula is proposed for the inertia factor; applying it for the Z254/2.67 test by $\beta = 3.1$ (overlap length/section height ratio); the result is as follows:

$$\alpha = 0.23 \times \beta - 0.18 = 0.533 \tag{15}$$

In the current study it is found that the calculated inertia factor is ~0.45 that shows good agreement, concerning the differences in the bolts.

3.6 Design method development

3.6.1. Calculated resistances for Z-sections

The Eurocode 3 [60] contains the resistances for various failure modes of Z-sections except for the overlapped zone, where the design resistance can be determined only by tests. In Table 23 the pure bending resistances (M_{Rd}) and the pure shear resistances (V_{Rd}) are summarized of a single Z-section for the studied cases. These values are used to compare to the end of overlap test based resistances. The bending moment-shear force interaction curves are calculated according to the Eurocode and shown in Chapter 3.6.2.

The doubled section resistances at the middle of the overlap for bending (M_{Rd2}) and for web crippling (R_{Rd2}) are also shown in Table 23. These values are used to compare to the

overlap support test results. The bending moment-transverse force interaction curves are calculated according to the Eurocode and shown in Chapter 3.6.3.

The web crippling design resistance (R_{Rd}) at the end support is compared to the end support test results and detailed in Chapter 3.6.4.

Table 23. Eurocode design resistances

Purlin height [mm]	Purlin thickness [mm]	Single section M_{Rd} [kNm]	Single section V_{Rd} [kN]	Double section M_{Rd2} [kNm]	Double section R_{Rd2} [kN]	End support R_{Rd} [kN]
203	1.50	8.64	29.23	17.28	28.89	3.30
203	1.90	12.60	46.24	25.20	43.91	6.07
203	2.67	20.20	90.69	40.40	81.54	13.53
254	1.70	14.80	36.53	29.60	33.77	4.05
254	2.00	19.40	50.62	38.80	45.78	6.27
254	2.67	30.40	90.45	60.80	79.15	12.80

3.6.2. End of overlap resistance

Figure 56 shows the test based design results (dot lines) and the Eurocode interaction curves (continuous lines) for the two section heights. Based on the obtained results the following conclusions can be drawn.

The end of overlap failure always occurs in one single section.

As far as bending resistance is considered, the calculated Eurocode values are tendentiously larger by 20-25% than the measured values. This difference can be explained by the following facts. In case of Z-sections with relatively small end-stiffeners (lips), distortional buckling has pronounced role. Earlier test experiences showed that in such cases the Eurocode calculation gives approximately 10% higher resistances than the real resistance as an average (the Eurocode is unsafe), but the difference can reach even 20% [38].

In the evaluation of the test results, the Eurocode 3 [60] procedure is followed. Since the number of repetitions is only 2, the average test results are multiplied by a factor of 0.9. It is reasonable to assume that this 10% reduction is over-conservative, and a more accurate statistical evaluation would lead to a higher test values.

In the carried-out tests holes (in the web and flange) existed just in the region where failure took place. Though there is no evidence on the effect of the holes, it is reasonable to assume that a moderate bending resistance degradation is due to the existence of holes.

Finally, it seems that the overlap has an unfavourable effect on the bending resistance if failure occurs at the end of the overlaps. The number of performed tests is too few to give an exact quantitative assessment on this effect, but it seems it is not more than 5-10% (on the bending resistance).

Based on the test results and the Eurocode methodology a design method is developed for these types of sections and overlap arrangement. Eq. (16) shows the bending moment resistance in the function of shear force. The α and β parameters are chosen to fit the interaction curves to the test based design resistances. The parameters are shown in Table 24 and the modified interaction curves in Figure 57.

$$M^{o}_{V,Rd} = \alpha \times M_{Rd} \quad \text{if} \quad V_{Ed} \le \beta \times 0.5 \times V_{Rd}$$

$$M^{o}_{V,Rd} = \alpha \times M_{Rd}\left[1-\left(1-\frac{M_{f,pl}}{M_{pl}}\right)\left(2\frac{V_{Ed}}{\beta \times V_{Rd}}\right)^{2}\right] \quad \text{if} \quad V_{Ed} > \beta \times 0.5 \times V_{Rd} \tag{16}$$

where $M_{f,pl}$ is the plastic moment resistance of the flanges, M_{pl} is the plastic moment resistance of the cross section and V_{Ed} is the applied shear force, α and β is defined in Table 24.

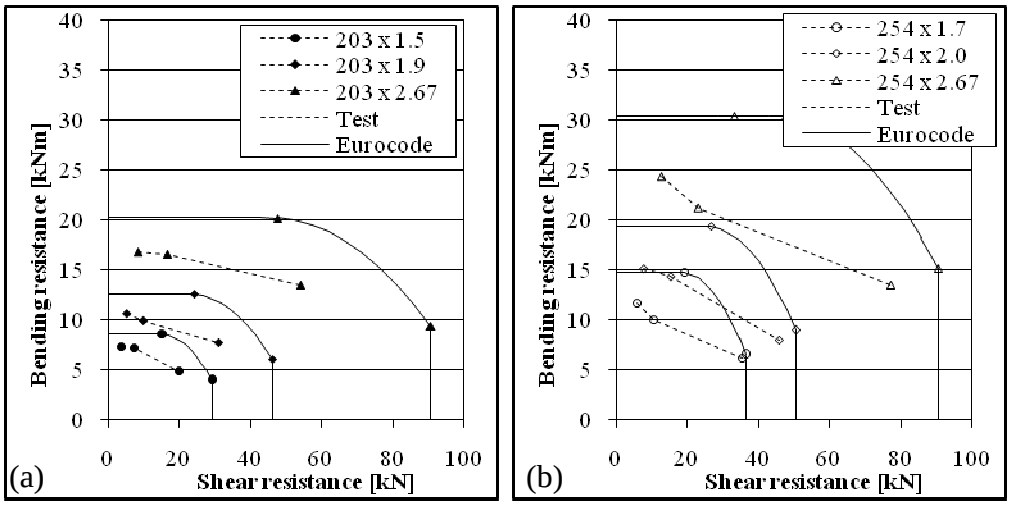

Figure 56. End of overlap resistance: (a) 203 mm and (b) 254 mm height purlin

Table 24. Design parameters

Purlin height [mm]	Purlin thickness [mm]	Design parameters α	β
203	1.50	0.825	0.775
203	1.90	0.787	0.815
203	2.67	0.823	0.755
254	1.70	0.676	1.000
254	2.00	0.738	0.952
254	2.67	0.699	0.920

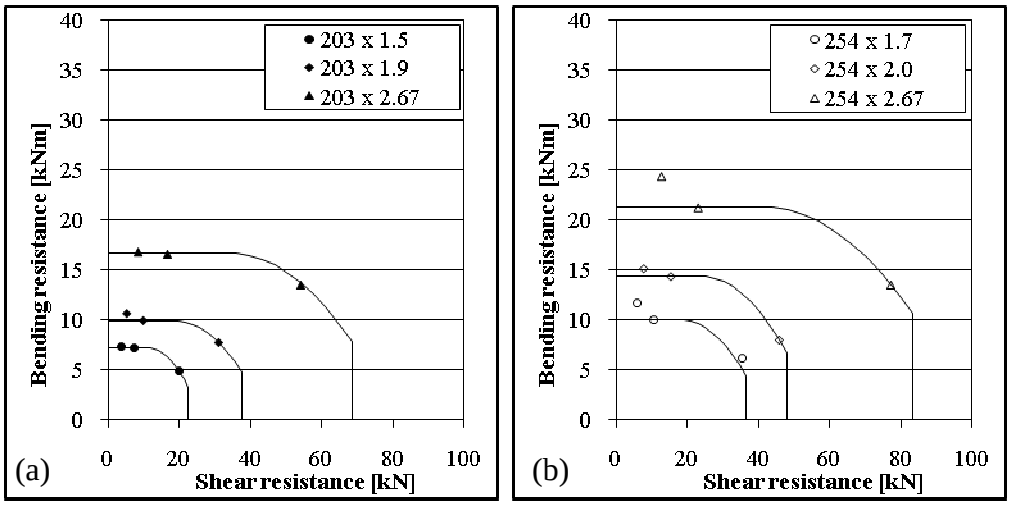

Figure 57. Modified design curves: (a) 203 mm and (b) 254 mm height purlin

3.6.3. Overlap support resistance

Figure 58 shows the test based design resistances (dot lines) and the Eurocode interaction curves (continuous lines) for the two section heights. Based on the obtained results the following conclusions can be drawn.

According to Eurocode calculation, bending and transverse force interaction is weak (in fact: negligible) if the bending moment or the transverse force is smaller that 25% of the resistance value. Since this design rule is based on experimental evidence, and since the measured bending moment and transverse force values in the carried-out tests are surely greater that 25% of the resistances, it is reasonable to conclude that all the measured values are interacted values, i.e. pure resistance values (to bending or to reaction force) are not measured.

In certain cases, especially tests with longer spans, failure occurred at the end of overlap region, too (despite of the reinforcement in that region). These values are marked by the upper arrows in Figure 58. Thus, in these cases the measured bending/reaction force values do not represent real overlap support failure values (the support resistance is higher).

Considering the above fact, it can be concluded that the measured bending moment-transverse force values lay on the Eurocode interaction curve in most of the cases. This means that the applied Eurocode calculation is applicable. The Eurocode resistance values (both bending and reaction forces) can be calculated by a simple summation of the corresponding resistances of the two overlapping sections.

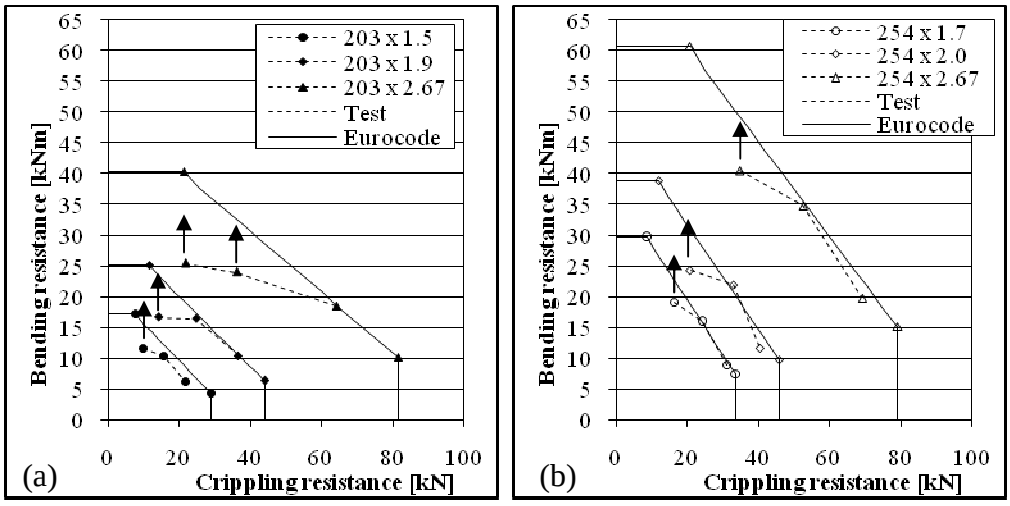

Figure 58. Overlap support resistance: (a) 203 mm and (b) 254 mm height purlin

3.6.4. End support resistance

Figure 59 shows the test based design results (dot lines) and the Eurocode resistances (continuous lines) for the two section heights. The Eurocode resistances calculated with 90 mm support width (upper flange of the gable Z-section) and two forces

According to the results, it can be concluded that the test results are 2.5-3.8 times higher than the Eurocode values. The Eurocode resistances are too conservative due to the fact that it is calibrated to stiff bearing, while here flexible gable Z-sections are applied as support.

The Eurocode design methodology can be modified as it is shown in Eq. (17) to reach closer values to the test based design resistances. By the given modification the results remain on the safe side for the studied arrangements. Further research is needed to develop more general formulations.

$$R_{w,Rd} = \alpha \times k_1 k_2 k_3 \left[6.66 - \frac{h_w / t}{64} \right] \left[1 + 0.001 \frac{s_s}{t} \right] t^2 f_{yb} / \gamma_{M1} \qquad (17)$$

where the proposed modification factor $\alpha = 2.2$; k_1, k_2, k_3 are constants of the Eurocode that are depend on the yield stress, the thickness, the fillet radius and the angle between the flange and web; s_s is the length of the bearing; h_w is the web height and t is the thickness of the purlin.

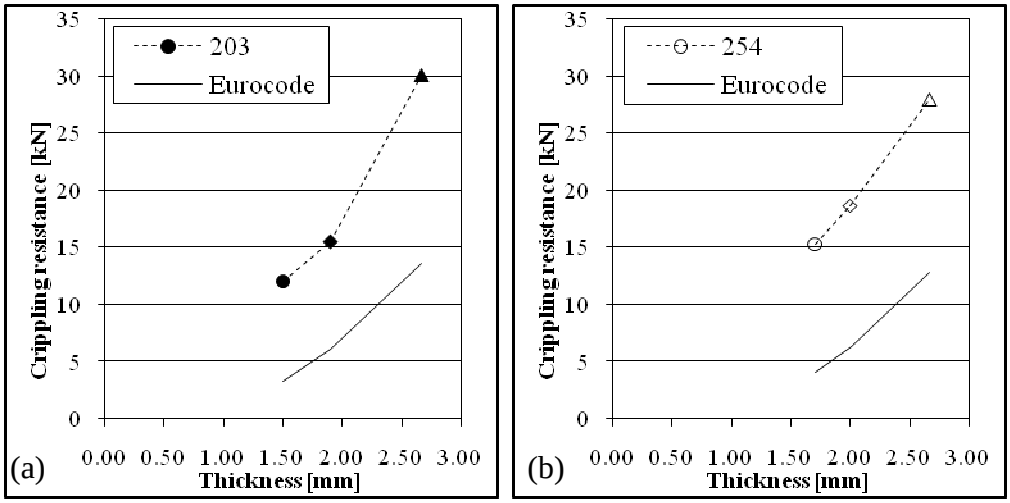

Figure 59. End support resistance: (a) 203 mm and (b) 254 mm height purlin

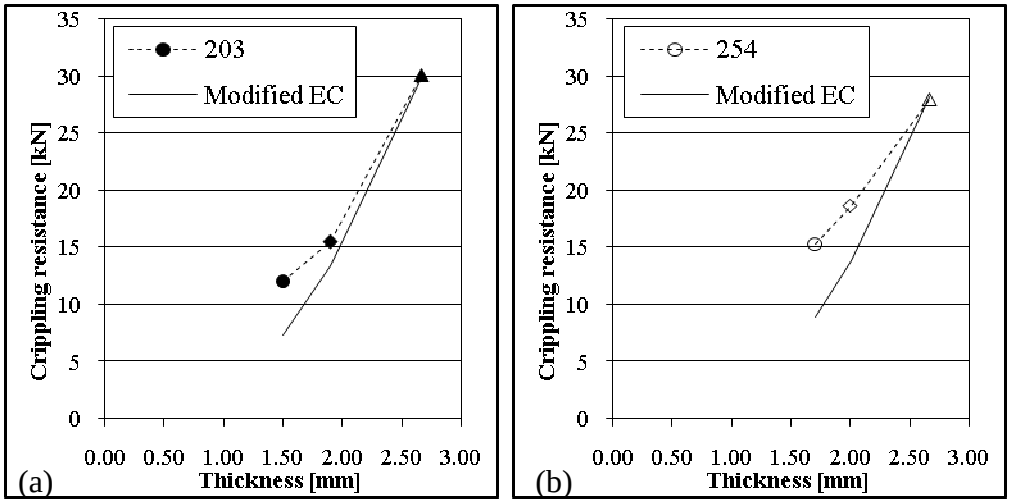

Figure 60. Modified design curves: (a) 203 mm and (b) 254 mm height purlin

3.7 Numerical models of continuous purlins

3.7.1. Introduction

As it is mentioned in the previous studies in Chapter 3.1.2 the finite element modeling of overlap zone can be found in [36]. That model concentrates on the bending moment-shear force interaction and overlap stiffness only. In my research various model levels of the overlap zone are worked out for the specific – experimentally tested – structural arrangements.

In case of complex structural problems and behaviour modes the FE modeling leads to numerical problems as well. In those cases it is practical to tend the model development from

the simplest model to the complex model [41]. This can be carried out by multi-level approaching of the problem.

The multi-level models contains local models such as single section (Figure 61a) and double section (Figure 61b) and global model (Figure 61c), respectively.

The local models are used to analyse the effect of structural and numerical approaching of the problem on the behaviour modes. It is easier to build these models, the run time is less and the analysis is more stable. The local models are used to describe the failure modes and resistances for the following internal forces:

- pure bending moment (single section),
- pure shear force (single section),
- bending moment and shear force interaction (single section and end of overlap model),
- bending moment and transverse force interaction (single and double section).

The results of the local models can be used to determine the bending moment – shear force interaction curves of various sections and the bending moment – transverse force interaction curves.

Parametric studies are carried out to analyse the effect of the following parameters to the behaviour modes and resistances:

- holes in the web and in the flanges,
- round or sharp edge of the section,
- contact model in case of double section,
- equivalent geometrical imperfection.

Based on the experiences, the local models can be joined to a global model which can be used to determine the:

- overlap stiffness,
- end of overlap behaviour and resistance,
- overlap support behaviour and resistance,
- end support behaviour and resistance.

The developed numerical model of the overlaps and supports is to be implemented to the program PurlinFED, presented in Chapter 5.

3.7.2. Shell finite element models

The various FE models of the overlapped joint are developed in Ansys FE program [64].

The Z-section geometry corresponds to the sections applied in the experimental tests. Those sections are produced with same lower and upper flange widths, which mean that in the overlap zone the two sections are tightened together. In the FE model this phenomenon is eliminated, the cross-sections' mid-planes are modeled in the distance of the plate thickness.

In the parametric studies the cross-section is modeled with sharp and round edges, and the bolt holes in the web and in the flanges are modeled as well. The sharp edges can be seen in Figure 61a on the single section and the round corners can be seen in Figure 61b on the double section model. An example of the bolt holes can be seen in Figure 61a, which pattern is similar to the holes at the end of the overlap in the experimental tests.

The SHELL181 shell finite element model of Ansys is applied which is able to follow the material and geometrical nonlinearities during virtual tests. The web, the flanges and the lips are divided into 26, 8 and 4 elements. This small element size is necessary to model the evolving yield mechanism around the edges. The total number of nodes is dependent on the member length; it varies from 5000-35 000.

The ends of the local models are stiffened with constraint equations as it is shown in Figure 61a. The loads and the boundary conditions are applied on the centre of the rigid end cross-

section in case of bending moment – shear force interaction analyses. Kinematic loads are used on the center nodes to generate the pure bending moment, pure shear force and the interaction of them. In case of bending moment – transverse force interaction analyses the bending moment is applied on the center node of the end cross-sections and the concentrated load is applied on the top flange by element pressure. By this method the interaction curves of the investigated experimental test can be produced. Additionally, horizontal supports are applied on upper and lower flange to simulate the supporting effect of the other Z-purlin.

The connection zone can be built up in two ways: (i) compression only beam elements between the purlins and (ii) contact pairs. The contact pairs cannot be used in the instability analysis. Instability analyses are used to define the shape of the equivalent geometrical imperfection. The bolts between the two purlins at the end of the overlap are modeled with constrained equations, where nodal displacements in the three directions are connected together.

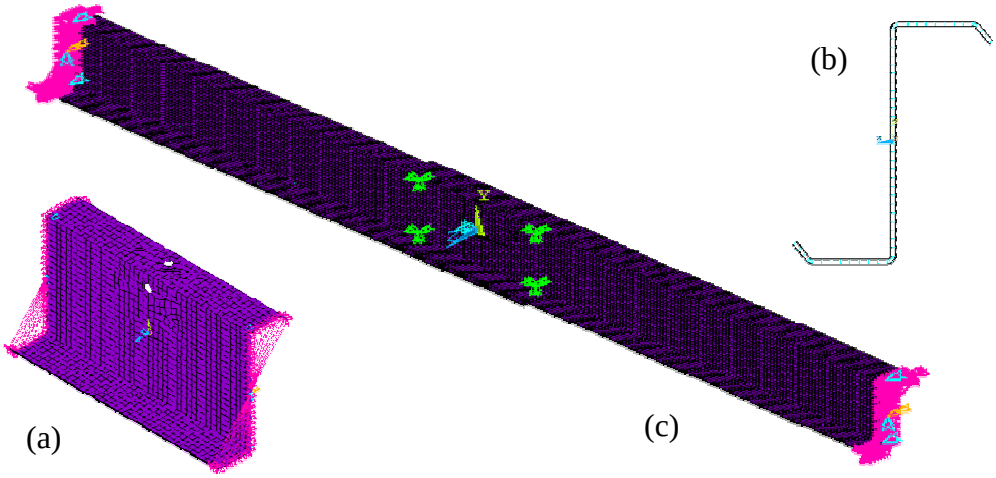

Figure 61. Local models: (a) single section with holes in the web and in the top flange, (b) double section with link elements between the plates and (c) global model

3.7.3. Local models – analysis and results

In the first step linear test analyses are carried out on the local models where the deformations and the internal forces are checked. After that instability analysis is carried out on each single section model by various combinations of the internal forces. The first buckling modes are shown in Figure 62a for bending moment and in Figure 62b for shear force. These modes are applied as equivalent geometrical imperfection for virtual tests.

The material and geometrical nonlinear FE simulation is called virtual test if the following conditions are satisfied:

- the real nonlinear material properties are used, in case of linear elastic – perfect plastic material model the yield stress corresponds to the measured yield stress on coupon test;
- the model contains the real imperfections of the structure: if the real imperfections are not measured it is possible to apply assumed geometrical imperfection to consider residual stresses and geometrical imperfection, where the shape and amplitude is chosen to cause the same behaviour and ultimate load, as experienced in the tests.

Virtual test based parametric studies are carried out on the local models of the single section to test the effect of bolt holes at the position of the failure and the imperfections' amplitude on the behaviour mode and resistance.

The experienced failure mode for bending moment – shear force interaction is yield mechanism of the compressed web-flange edge, as it is shown in Figure 41. The same failure mode of the numerical model is experienced, as it can be seen in Figure 62c and d, sections without and with holes.

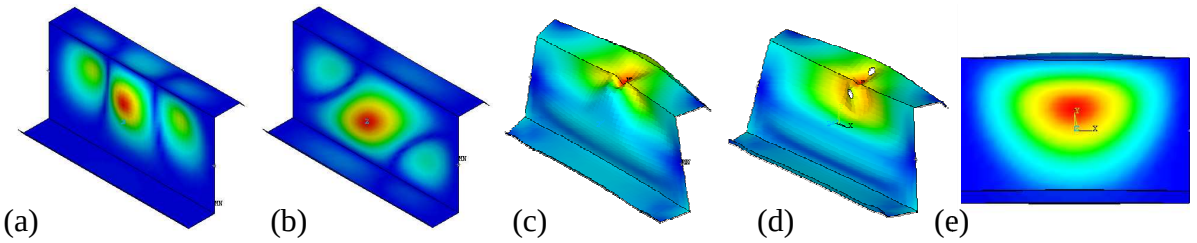

Figure 62. First buckling modes for (a) pure bending moment and (b) pure shear force and plastic plate buckling – yield mechanism on single section (c) without and (d) with hole; and (e) web crippling failure

The imperfection sensitivity is checked on both types of single sections. Three virtual tests are carried out: without imperfection, with geometrical imperfection of the first and the second buckling mode. The amplitude of the imperfection corresponds to the thickness of the element. The bending moment – displacement curves are shown for sections with and without hole in Figure 63. The perfect and the imperfect curves show significant differences. The perfect curve reaches the ultimate load after a partially linear phase and suddenly the load bearing capacity starts to decrease (similarly to a bifurcation curve). The imperfect curves show continuously increasing load bearing capacity after the first yield appears in the cross-section and the limit point occur at higher deformation level. There is increase in the ultimate load compared to the perfect model: the application of the first buckling mode shows 3% increase while the second buckling mode shows 5% increase. The similar behaviour experienced in case of sections with hole, as it is shown in Figure 63. The decrease in the ultimate load is 3% due to the presence of holes.

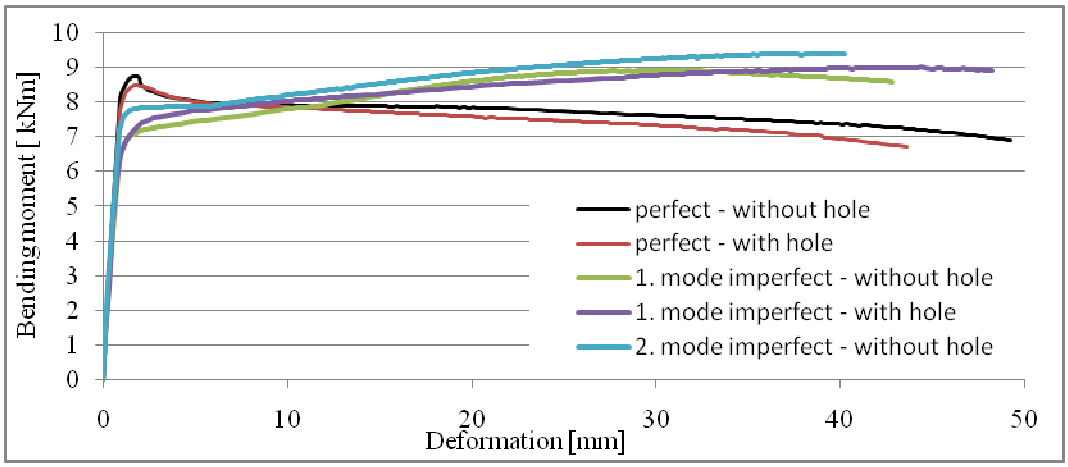

Figure 63. Imperfection sensitivity of single section with and without hole

Parametric studies are carried out on the bending moment – transverse force interaction problem. It can be concluded on the existing results that web crippling is more sensitive to the geometrical imperfections. The imperfection amplitude corresponds to the thickness can cause 30% decrease in the ultimate load. In this case the double section local model is used by the two types of contact algorithms between the two sections. The failure mode of numerical model can be seen in Figure 62e which is similar to the failure mode of the experimental test, as it is shown in Figure 43.

3.8 Virtual test based interaction curves

3.8.1. Bending moment and shear force interaction

The bending moment – shear force interaction curves of the tested cases are produced by a series of virtual tests on the single section local model. The points on the interaction curves from the tests and from the numerical analyses on perfect model are shown in Figure 64a for the Z203 cross-sections. As it is shown previously the imperfect results are within 3-5% of the perfect results. The numerical results are close to the experimental results, the tendencies of the two interaction curves are similar for all examined cross-section. The results show that the difference between the two results is around 10%.

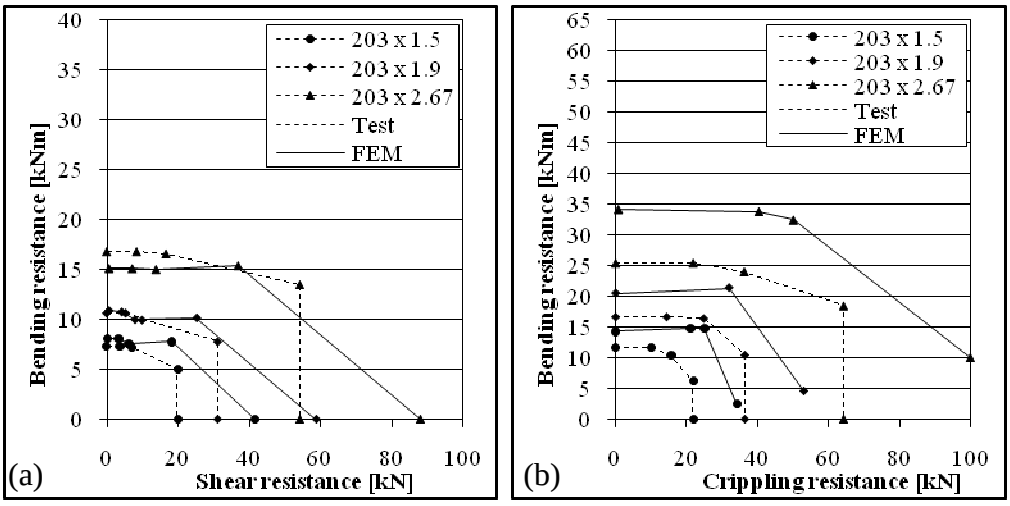

Figure 64. Interaction curves from test and numerical results: (a) bending moment and shear force interaction, and (b) bending moment and transverse force interaction

3.8.2. Bending moment and transverse force interaction

Virtual tests are carried out on the double section model in perfect case and the bending moment – transverse force interaction curve is determined. The results, together with the experimental results, are shown in Figure 64b. In these cases (perfect model) the tendencies of the curves are in good correlation with the experimental results; however the ultimate resistances are about 30% higher than the experimental results. As is it showed in the parametric studies the thickness size imperfection cause about 30% decrease in the ultimate load which are close to the experimental results, but the imperfect analyses are not extended to the full test program yet.

3.8.3. Summary and conclusion

In this chapter the development of the numerical modeling of continuous purlin system and the first results are presented here. It can be concluded that the local models are accurate to model the interaction phenomena experienced in the tests. Similar tendencies in the interaction curves can be observed. In the case of bending moment – shear force interaction the ultimate resistances are within 10%. The model shows the capability to use it to extend the experimental results by virtual tests. Further studies are needed however to analyze the behaviour of the overlap support zone where double sections are applied and extend the numerical program to the full test program. The global model is necessary to determine the overlap stiffness and to analyse the end support behaviour modes and resistance by shell finite element models.

4. Anti-sag system elements

4.1 Introduction

4.1.1. Structural problems

In cold-formed thin-walled roof systems additional bracings are applied in the roof plane – called anti-sag system – to evolve the following effects:

(i) ensure lateral support for the lower flange of the purlins in midbays,
(ii) derive the roof in plane forces to the main frame from the in-plane components of the loads, from the stressed skin forces and from earthquake excitation.

The components of the anti-sag system are shown in Figure 65 and Figure 66:

(i) cold-formed U-section sag channels with large openings in the web,
(ii) adjustable sag channel for irregular purlin spacings,
(iii) peak elements between the two roof planes and
(iv) flying sag system built from tie rod elements to transfer the forces to the main frames.

The design of these special elements due to the special structural arrangements and joints is not covered by standards.

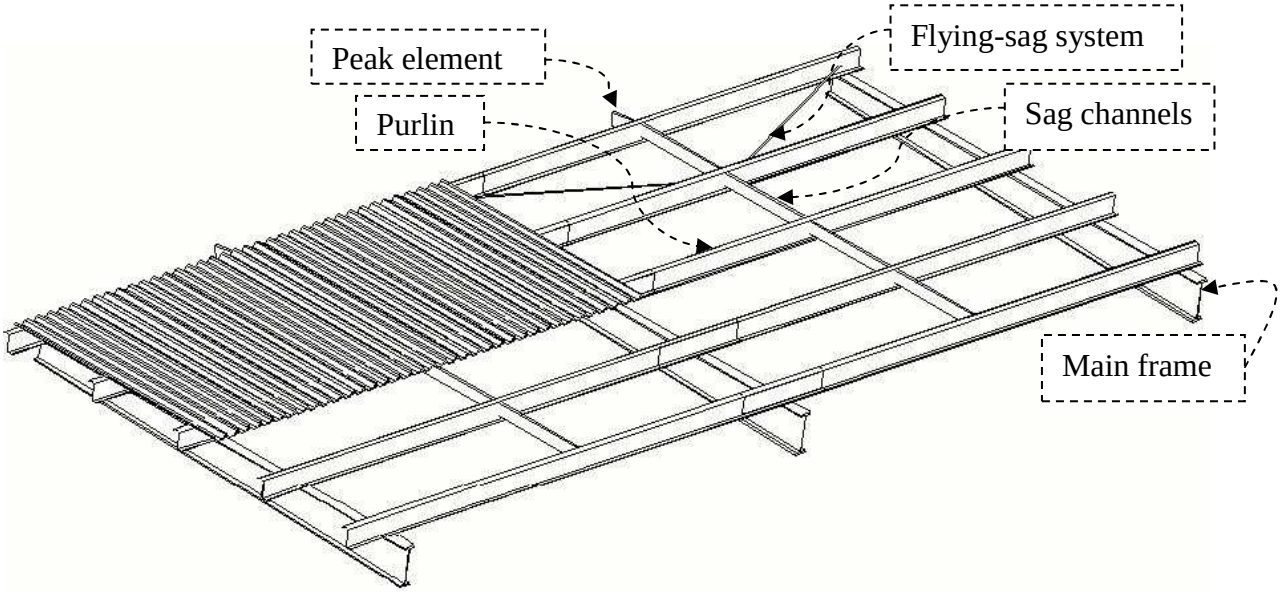

Figure 65. Arrangement of the various components of an anti-sag system

4.1.2. Previous studies and conclusions

In the investigated literature I did not find:

- experimental studies on this special type of supplementary elements of thin-walled cold-formed roof system,
- the behaviour modes and the design resistances of the various components,
- finite element model which can follow the behaviour modes of the presented system.

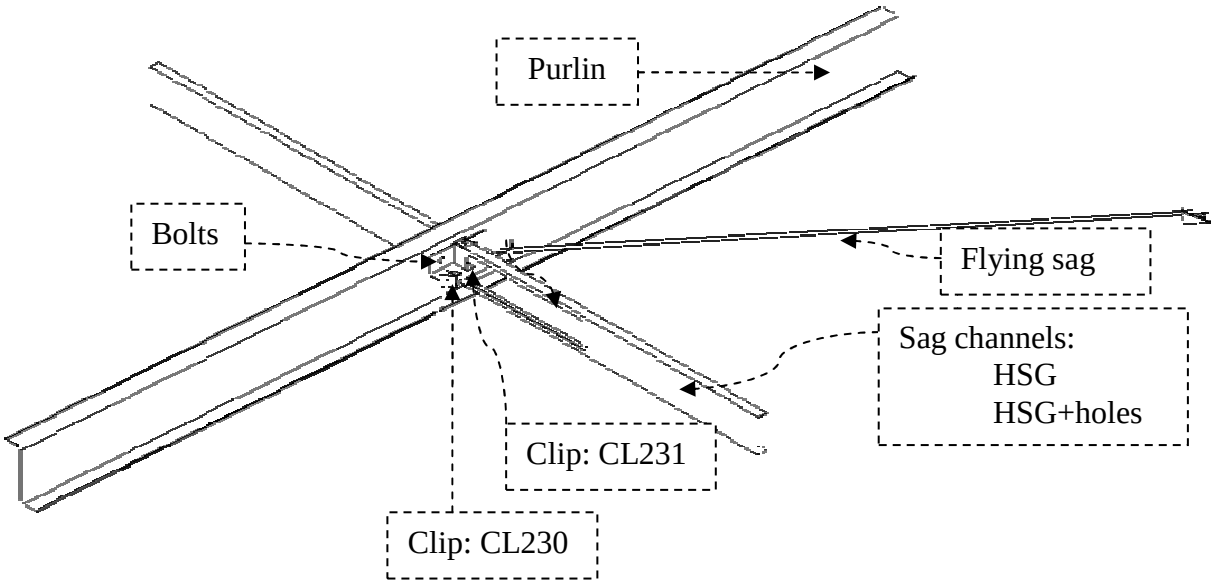

Figure 66. Details of the anti-sag system

4.1.3. Purpose and research strategy

The purposes of the research is to determine the behaviour modes and design resistances of the previously presented supplementary elements of thin-walled roof system (anti-sag systems) by experimental tests and develop a shell finite element model of the main part of the system (sag channel) for further studies.

4.2 Test program

The research is focused on the following details and internal forces:

- sag channels with various length (1350 and 1550 mm) and web (with or without web openings) for compression and tension,
- adjustable piece of the sag channels for compression and tension,
- peak channel tests for compression and tension,
- flying sag system in two arrangements: Case 1 – diagonals in two directions, symmetrical (Figure 70), Case 2 – diagonal in one direction, unsymmetrical arrangement (Figure 70). The flying sag system is tested for tension only.

The tests are completed with the aim to find the experimental behaviour modes and the test resistances; and from these results to derive the test based design resistances by the Eurocode 3 standardized methodology.

The tests are completed in the Structural Laboratory of the Department of Structural Engineering, BME. The test setup corresponds to the standardized structural arrangement of Astron company. In the test program 17 specimens for sag channels; 6 specimens for adjustable piece tests, 12 specimens for peak channels are tested. The flying sag tests are carried out in two steps: the first series contained 16 specimens and the second series with improved structural details contained 21 specimens. The observed behaviour modes are described qualitatively and the main design parameters are determined quantitatively. Altogether 72 tests are carried out.

The mechanical properties of the specimens' base material are determined by 8 coupon tests of the sag channels, 3 tests on the purlin base material and the mechanical properties of the BZD12030 bolts (M12x30, 4.6) are also determined by 3 tests.

The test results are evaluated according to the recommendations of Eurocode 3 and the derived design values are presented.

The test program for five structural arrangements is summarized in this chapter. In the first test series two sag channel types (with and without web openings) and two lengths (1350 and 1550 mm) are tested for compression and tension, respectively. Each test is repeated four times. These are altogether 16 specimens that are summarized in Table 25. The specimens are tested for compression first then for tension. One test (sag channel without holes in the web and with 1550 mm length, test number 17) is repeated for tension test only to see the effect of previous compression test on the tensile resistance. This test showed that the previous compression test on the specimen has no effect on the tensile resistance.

The adjustable piece is tested with three various bolt positions in the adjustable element, as shown in Figure 67:

- bolt position 1: the bolt is close to the middle of the sag channel,
- bolt position 2: the bolt is close to the end of the sag channel,
- bolt position 3: the bolt is in the closest position to the bolt in the web of the sag channel.

The test program is summarized in Table 26. Two elements are used: the adjustable piece CL226 and the modified sag channel HSH.

Three various peak elements are tested at 6% (CL221), 10% (CL222) and 20% (CL223) roof slope; each is repeated 4 times.

The flying sag system is tested in two structural arrangements. The results of the first test series showed failure modes to be avoided in the practice, so new joints are developed for the flying sag system. The test program for the first series is shown in Table 28 and the test program with improved details are shown in Table 29. The modified CL231 clip is called as XCL-C and the reinforcing plate is called as XCL-D in the table. The angle between the purlin and the tie rods are defined as α in the last column of the table.

Table 25. Test program for sag channel tests

Test #		Section	Internal force	L [mm]	t [mm]
1	1	HSG	Compression+Tension	1550	1.5
2	2	HSG	Compression+Tension	1550	1.5
3	3	HSG	Compression+Tension	1550	1.5
4	4	HSG	Compression+Tension	1550	1.5
5	1	HSG	Compression+Tension	1350	1.5
6	2	HSG	Compression+Tension	1350	1.5
7	3	HSG	Compression+Tension	1350	1.5
8	4	HSG	Compression+Tension	1350	1.5
9	1	HSG+holes	Compression+Tension	1550	1.5
10	2	HSG+holes	Compression+Tension	1550	1.5
11	3	HSG+holes	Compression+Tension	1550	1.5
12	4	HSG+holes	Compression+Tension	1550	1.5
13	1	HSG+holes	Compression+Tension	1350	1.5
14	2	HSG+holes	Compression+Tension	1350	1.5
15	3	HSG+holes	Compression+Tension	1350	1.5
16	4	HSG+holes	Compression+Tension	1350	1.5
17	1	HSG	Tension	1550	1.5

Table 26. Test program for adjustable sag channel tests

Test #		Adjustable element and section	Bolt position	Internal force	L [mm]	t [mm]
18	1	CL226+HSH	1	Compression+Tension	1550	1.5
19	2	CL226+HSH	1	Compression+Tension	1550	1.5
20	3	CL226+HSH	1	Compression+Tension	1550	1.5
21	4	CL226+HSH	1	Compression+Tension	1550	1.5
22	1	CL226+HSH	2	Compression+Tension	1550	1.5
23	1	CL226+HSH	3	Compression+Tension	1550	1.5

Table 27. Test program for peak tests

Test #		Section	Internal force	L mm	t mm
24	1	CL221	Compression+Tension	692	1.5
25	2	CL221	Compression+Tension	692	1.5
26	3	CL221	Compression+Tension	692	1.5
27	4	CL221	Compression+Tension	692	1.5
28	1	CL222	Compression+Tension	689	1.5
29	2	CL222	Compression+Tension	689	1.5
30	3	CL222	Compression+Tension	689	1.5
31	4	CL222	Compression+Tension	689	1.5
32	1	CL223	Compression+Tension	682	1.5
33	2	CL223	Compression+Tension	682	1.5
34	3	CL223	Compression+Tension	682	1.5
35	4	CL223	Compression+Tension	682	1.5

Table 28. Test program for flying sag tests

Test #		Clips	Case	$\alpha\,[^\circ]$
36	1	CL230+CL231	1	26.8
37	2	CL230+CL231	1	26.8
38	3	CL230+CL231	1	26.8
39	4	CL230+CL231	1	26.8
40	1	CL230+CL231	2	27.1
41	2	CL230+CL231	2	27.1
42	3	CL230+CL231	2	27.1
43	4	CL230+CL231	2	27.1
44	1	CL230+CL231	1	7.9
45	2	CL230+CL231	1	7.9
46	3	CL230+CL231	1	7.9
47	4	CL230+CL231	1	7.9
48	1	CL230+CL231	2	8.8
49	2	CL230+CL231	2	8.8
50	3	CL230+CL231	2	8.8
51	4	CL230+CL231	2	8.8

Table 29. Test program for flying sag tests with improved joint

Test #		Clips	Tie rod ends	Case	α [°]
52	1	XCL-C, XCL-D	CL230+CL230	1	26.1
53	2	XCL-C, XCL-D	CL230+CL230	1	26.1
54	3	XCL-C, XCL-D	CL230+CL230	1	26.1
55	4	XCL-C, XCL-D	CL230+CL230	1	26.1
56	5	XCL-C, XCL-D	CL230+CL230	1	26.1
57	1	XCL-C, XCL-D	CL230+CL230	2	26.4
58	2	XCL-C, XCL-D	CL230+CL230	2	26.4
59	3	XCL-C, XCL-D	CL230+CL230	2	26.4
60	4	XCL-C, XCL-D	CL230+CL230	2	26.4
61	1	XCL-C, XCL-D	CL230+CL230	1	7.4
62	2	XCL-C, XCL-D	CL230+CL230	1	7.4
63	3	XCL-C, XCL-D	CL230+CL230	1	7.4
64	4	XCL-C, XCL-D	CL230+CL230	1	7.4
65	1	XCL-C, XCL-D	CL230+CL230	2	8.2
66	2	XCL-C, XCL-D	CL230+CL230	2	8.2
67	3	XCL-C, XCL-D	CL230+CL230	2	8.2
68	4	XCL-C, XCL-D	CL230+CL230	2	8.2
69	5	XCL-C, XCL-D	plate+CL230	2	8.2
70	6	XCL-C, XCL-D	plate+CL230	2	8.2
71	7	XCL-C, XCL-D	plate+plate	2	8.2
72	8	XCL-C, XCL-D	plate+plate	2	8.2

4.3 Test arrangements

4.3.1. Setup for sag channel and adjustable piece tests

The test arrangement for sag channel and adjustable piece tests is shown in Figure 68. One sag channel is tested with the typical end detail. Two end elements are used at both ends and two purlins are applied for the proper connection of the sag channels. The length of the end elements is 500 mm. The two purlins are fixed with one bolt at one end to provide rotation ability.

The end sag channels are fixed with four bolts to the end support and to the hydraulic jack. The load is applied by MTS hydraulic jack, the ultimate load is 250 kN (built-in load cell; force or displacement control; min. measuring domain 25 kN with high precision). The maximum displacement of the jack is 150 mm. Displacement controlled load is applied during the tests. The longitudinal displacement is measured by the MTS built-in measurement system. The various bolt positions in the adjustable piece can be seen in Figure 67.

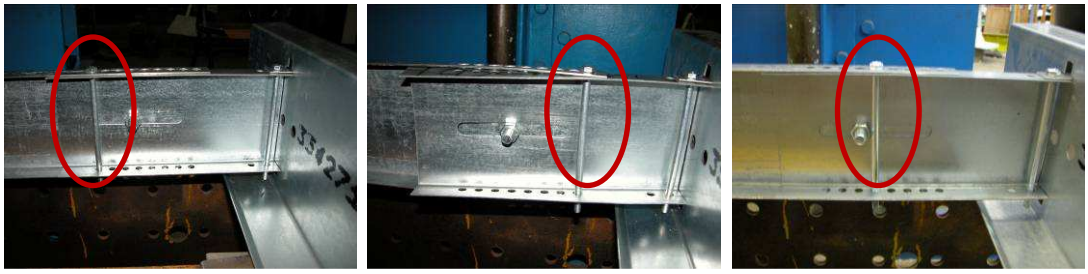

Figure 67. Bolt positions 1, 2 and 3 in the adjustable piece tests

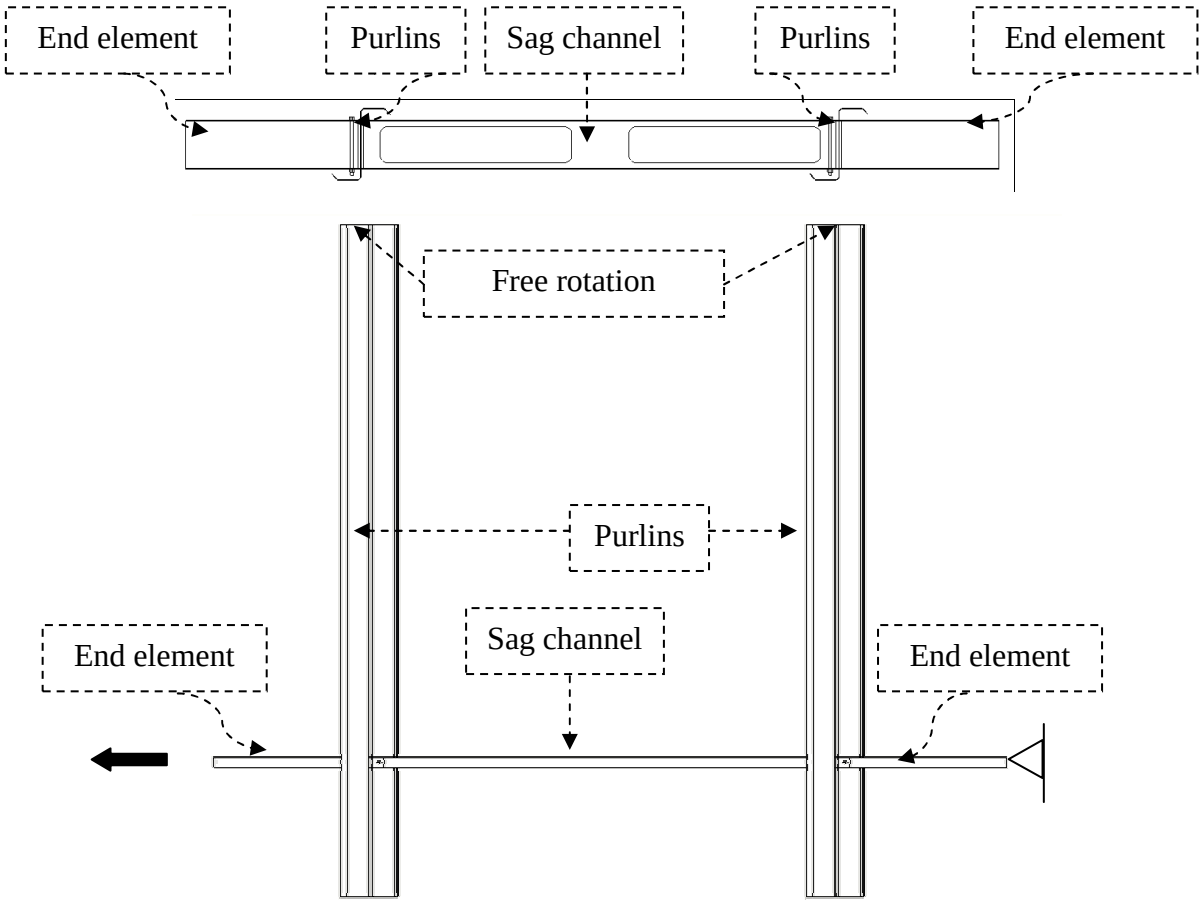

Figure 68. Test arrangement for sag channel and adjustable piece tests

4.3.2. Setup for peak channel tests

The test arrangement for peak channel tests is shown in Figure 69. The structural arrangement is the same as it was in the previous tests; the only difference is the variable slope of specimens. One peak channel is tested with the typical end detail, two end elements are used at both ends and two purlins are applied for the proper connection of the sag channels. The length of the end element is 600 mm. The two purlins are fixed with one bolt at only one end to provide free rotation.

The end sag channels are fixed with four bolts to the end support and to the MTS hydraulic jack. Hinges are applied with horizontal axes at both ends. Displacement controlled load is applied during the tests. The horizontal displacement is measured by the MTS built-in measurement system. The test setup in the laboratory can be seen in Figure 69.

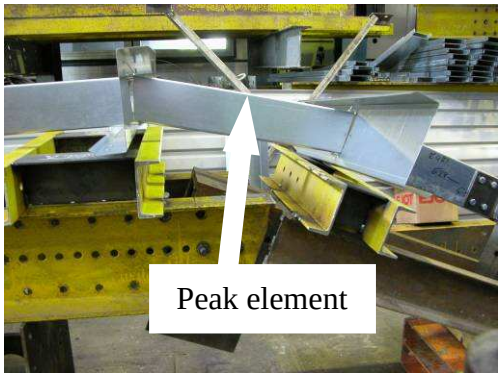

Figure 69. Test arrangement in the laboratory

4.3.3. Setup for flying sag system tests

Two structural arrangements are tested; the first one is where the original joints of the Astron company are applied. After the first test series the observed failure modes required the development of new structural detail (this is presented later on).

The test arrangement of the first series for flying sag system is shown in Figure 70. Two cases are tested in a symmetrical (Case 1) and unsymmetrical (Case 2) arrangement. The tensile force is applied through the sag channel. The two ends of the purlin are not fixed, it can slide on a steel plate. The end of the sag channel can slide, as well. The applied angles of the diagonal can be found in Table 28. The steel quality of the applied bolts is 4.6 except the bolts at the far end of the tie rods where 8.8 bolts are used to avoid the failure there. The details can be seen in Figure 71 and Figure 72.

For Case 2 (one diagonal tie rod) additional lateral support is applied on the lower flange of the purlin to avoid the lateral movement of the purlin due to the unsymmetrical arrangement as shown in Figure 73. The initial friction resistance of the lateral support is 60 N and $0.001 \times F$ during the load history, where F is the applied force perpendicular to the sliding direction. Two different loading equipments are used during the flying sag tests.

Tests 36-43: the load is applied by an MTS hydraulic jack. The load and the displacement are measured by built-in measurement system of the MTS.

Tests 44-51: the load is applied by a 63/40x630 hydraulic jack; force controlled; maximum displacement is 630 mm. In this case the load is measured by load cell and the displacement by inductive transducer.

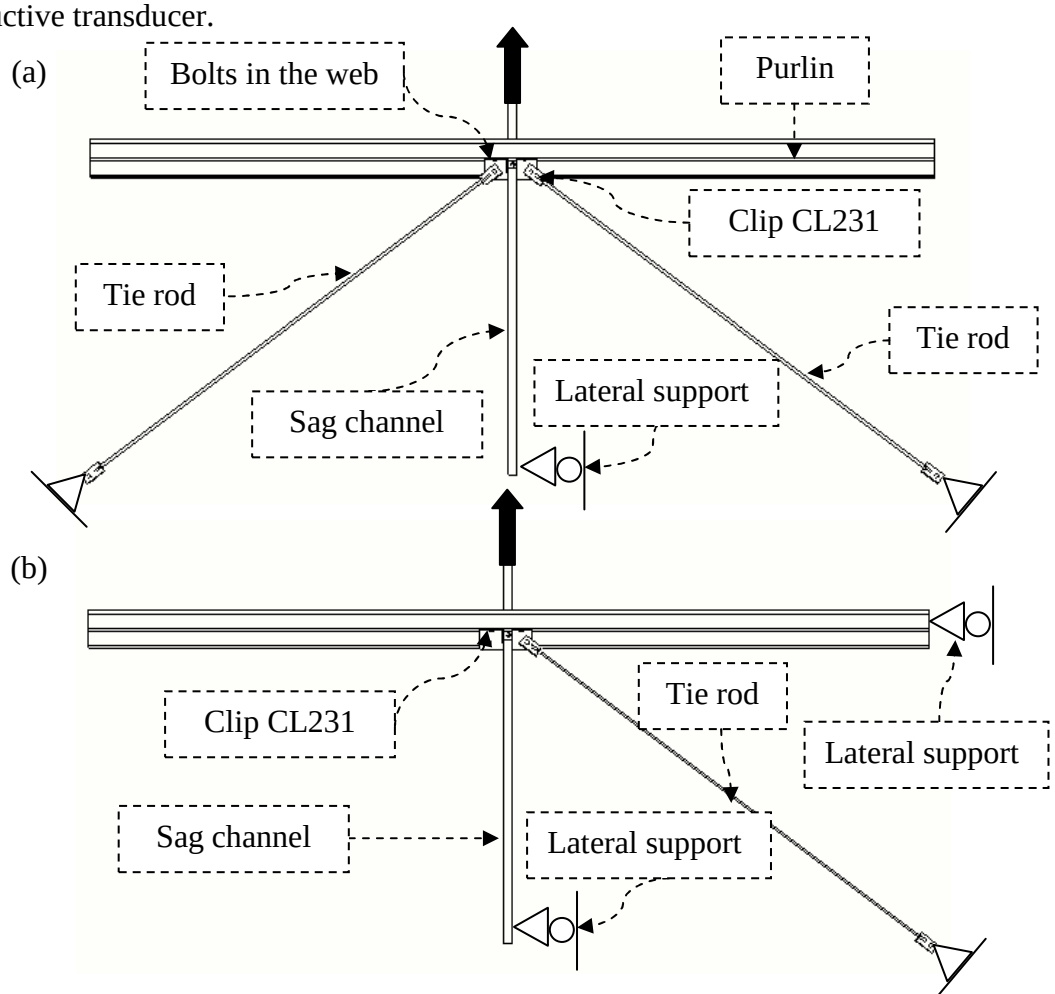

Figure 70. Test arrangement of flying sag system: (a) Case 1 and (b) Case 2

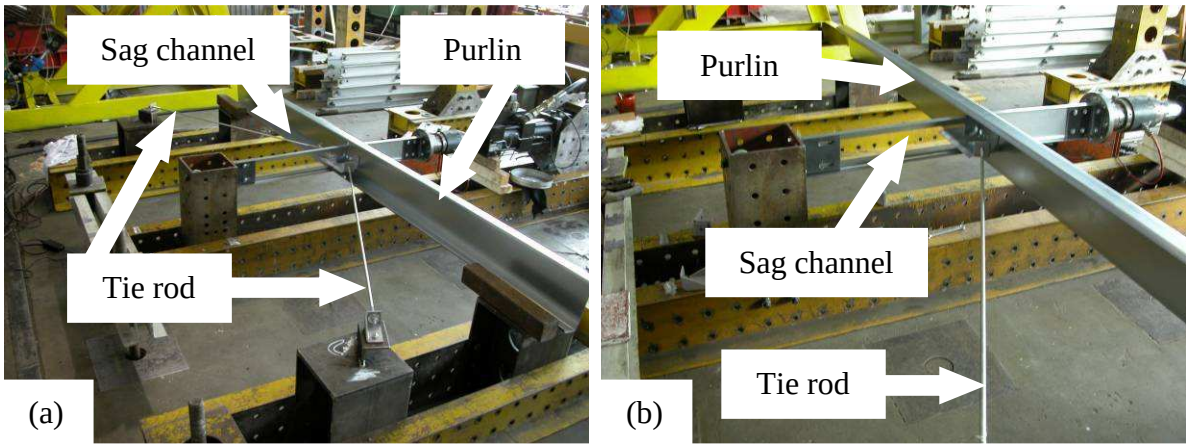

Figure 71. Test arrangement in the laboratory: (a) Case 1 and (b) Case 2

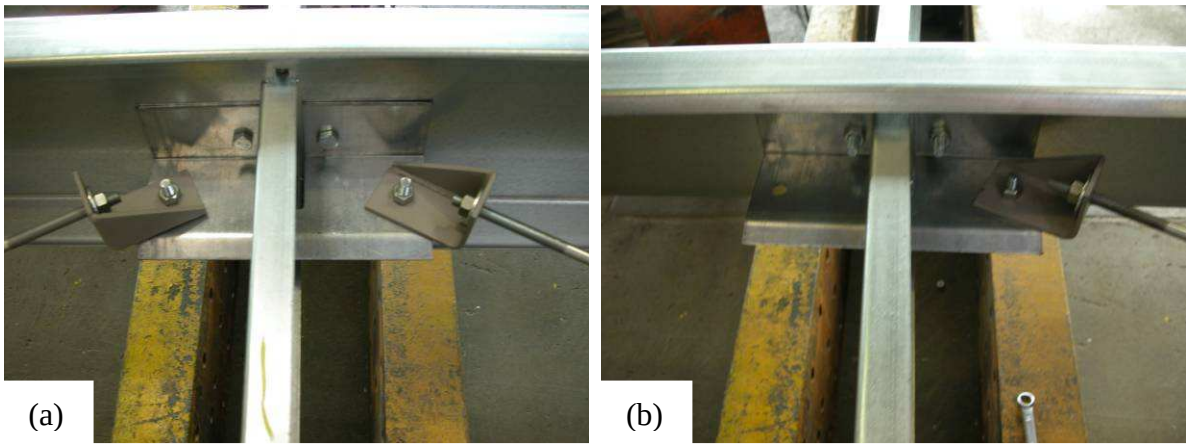

Figure 72. Details of the test arrangement: (a) Case 1 and (b) Case 2

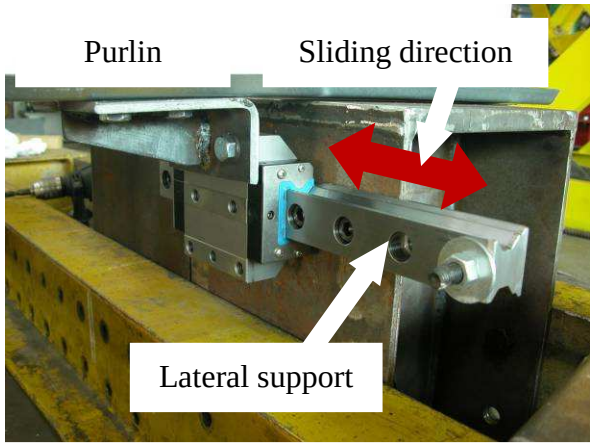

Figure 73. Lateral support in Case 2

After the first test series is completed new structural detail is developed at the sag channel, purlin and tie rod joint. As it is presented in the next chapter the failure mode was the pull-through failure of the bolts in the web of the purlin. To avoid this failure, reinforcing plate is applied at the purlin web, as it can be seen in Figure 74. This figure shows new gusset plates at the end of the tie rods which results in less deformation of the joint.

The other details of the second tests series are the same as in the previous cases. The load is applied with the 63/40x630 hydraulic jack and the force is measured in the sag channel and in the tie rods as well.

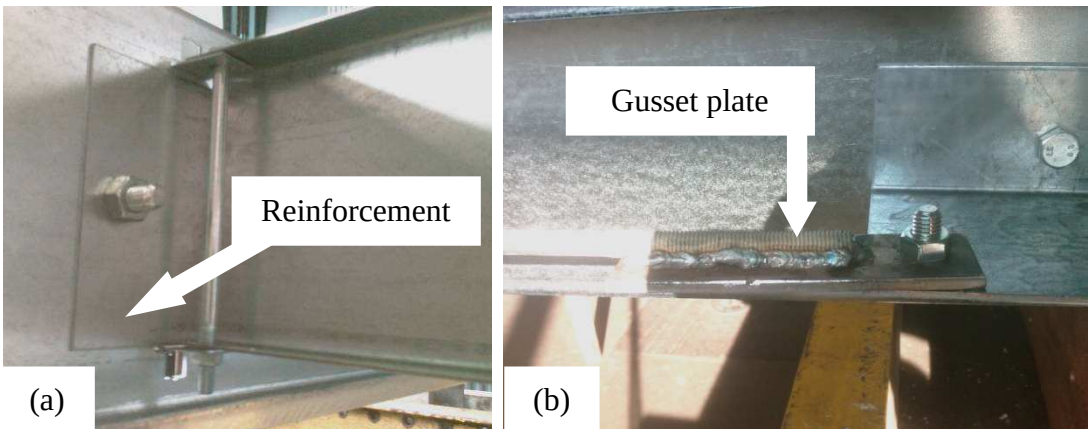

Figure 74. Improvements of the new structural arrangement: a) reinforcement plate, b) gusset plate at the end of the tie rod

4.4 Test results

4.4.1. Failure modes

The results of the sag channel and flying sag system tests are the ultimate loads of the specified failure modes, the ultimate behaviour and the load-deformation curves. In the first step the observed failure modes are presented. After that the test results are summarized for the whole test program. The experienced failure modes for compression and tension are summarized in Table 30-Table 32.

Table 30. Sag channel failure modes for compression

Mode #	Definition
c1)	Flexural-torsional buckling
c2)	Flexural buckling
c3)	Interaction of flexural-torsional buckling and local buckling
c4)	Interaction of global mechanism and flexural buckling
c5)	Local buckling at the web of the sag channel
c6)	Interaction of global mechanism and local buckling

Table 31. Sag channel failure modes for tension

Mode #	Definition
t1)	Bearing failure of the bolted connection

Table 32. Flying sag failure modes

Mode #	Definition
t2)	Pull-through failure of the bolts in the purlin web
t3)	Bolt shear failure in the CL231 clip
t4)	Pull-through failure of the bolts in the CL230 clip
t5)	Tie rod tensile failure

The defined modes are identified by experimental observation of the failure modes which are presented below.

Mode c1): Flexural-torsional buckling

Typical failure mode for the longer (1550 mm) HSG sag channels without holes, Figure 75.

Figure 75. Failure mode c1), c2) and c3)

Mode c2): Flexural buckling

Typical failure mode for the shorter (1350 mm) HSG sag channels without holes, Figure 75.

Mode c3): Interaction of flexural-torsional buckling and local buckling

Typical failure mode for the HSG channels with holes, Figure 75.

Mode c4): Interaction of global mechanism and flexural buckling

Failure mode of the adjustable piece only, if the bolt is close to the end of the sag channel (bolt position 2), Figure 76.

Figure 76. Failure mode c4)

Mode c5): Local buckling at the web of the sag channel

Typical failure mode for peak channel tests, Figure 77. This failure occurs if the end of the sag channel reaches the purlin before the BZD08160 bolt starts to work for compression.

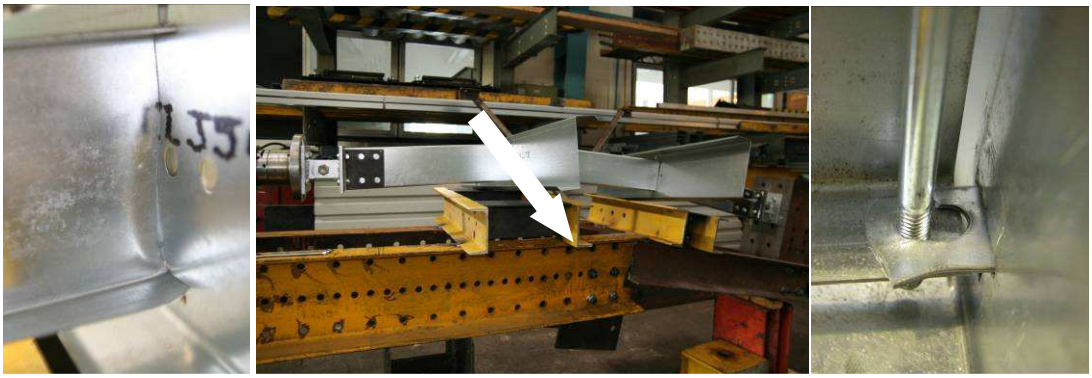

Figure 77. Failure mode c5), c6) and t1)

Mode c6): Interaction of global mechanism and local buckling
Typical failure mode for the peak channel with higher roof slope, Figure 77.
Mode t1): Bearing failure of the bolted connection (BZD08160)
Failure mode of all specimens under tension, Figure 77.
Mode t2): Pull-through failure of the bolts in the purlin web
Typical failure mode for Case 1 with large angle, Figure 78.

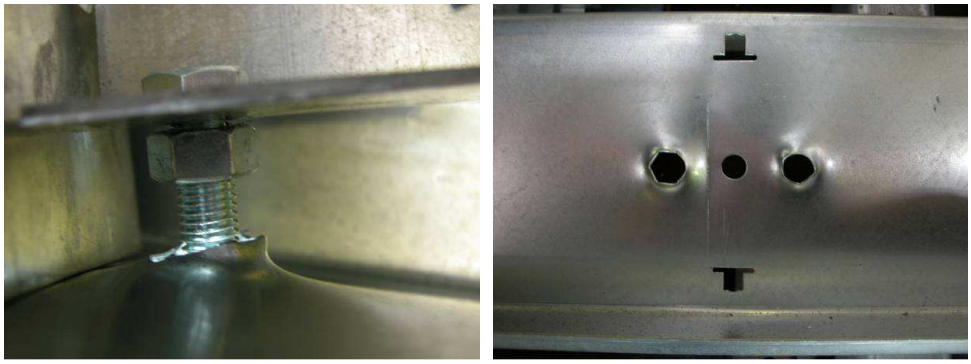

Figure 78. Failure mode t2)

Mode t3): Bolt shear failure in the CL231 clip
Typical failure mode of the flying sag system, the shear failure of the BZD12030 bolts in the CL231 clip, Figure 79. Note that the “shear failure” means a combined tension-shear failure due to the rotation of the bolt axis.

Figure 79. Failure mode t3)

Mode t4): Pull-through failure of the bolts in the CL230 clip
This failure mode is occurred when the sliding support reached the deformation limit which increased the force in the tie rod, Figure 80. This test is not used in the evaluation method because it cannot be occurred in a real structure.

Figure 80. Failure mode t4)

Mode t5): Tie rod tensile failure

This failure mode is occurred when the sliding support reached the deformation limit which increased the force in the tie rod, Figure 81. This test is not used in the evaluation method because it cannot be occurred in a real structure.

Figure 81. Failure mode t5)

Beyond the ultimate failure modes defined above, the following ultimate behaviour modes are observed: (i) crack in the weld of the CL230 clip, (ii) large deformation of the CL230 clip, (iii) large deformation of the tie rod at the end near to the CL231 clip, (iv) deformation of the hole in the sag channel (at the connection to each other). Furthermore, it can be concluded that these connection types are very “soft”. Large deformation is experienced of the system (mainly in the CL231 clip), the maximum displacement in the direction of the sag channel can be ~250 mm. The residual deformation can be significant as well. This behaviour indicates the application of new end gusset plates of the tie rods which results less deformation.

The test result summarized in the next section belongs to the ultimate limit state of the connection. The serviceability limit state is not analysed; these can be studied by the functional requirements of the roof system.

4.4.2. Typical force-displacement diagrams

Force-displacement curves of the four structural details are shown in Figure 82-Figure 85 and described below.

Figure 82 shows a typical axial force - axial displacement curve of the sag channel tests. Compression force is applied first on the specimen. The uploading curve part is marked with 1 in the figure. The specimen is unloaded after 12 kN (~60 % of the ultimate load). The un- and uploading loop is marked with 2. The residual deformation of the system is 10 mm (~50 % of the total displacement), and the second uploading stiffness is more rigid than in the first one due to the slip of the bolted connection in the structure for the first load. After the compression failure (buckling) is occurred and the ultimate load is reached (point 3) the structure is unloaded and the tension load is started. The residual deformation is 10 mm. The stiffness of the first tension part is low due to the re-arrangement of the structural connections (part 4 in the figure). After 10 kN (~60 % of the ultimate load) the tension load is unloaded and uploaded again. The loop is marked with 5. The residual deformation from the point where the load is turned into tension is 15 mm, which is also 50 % of the total deformation for tension. The stiffness of the reloading is higher comparing to the first loading due to the slip of the bolted connection between the sag channels for the first loading. The tension failure is occurred at point 6 in the curve.

The same loading procedure is carried out on the adjustable elements of the sag system, as shown in Figure 83. The stiffness of the adjustable elements for compression and tension is

less than the normal sag channel stiffness because there are more bolted connections in the system.

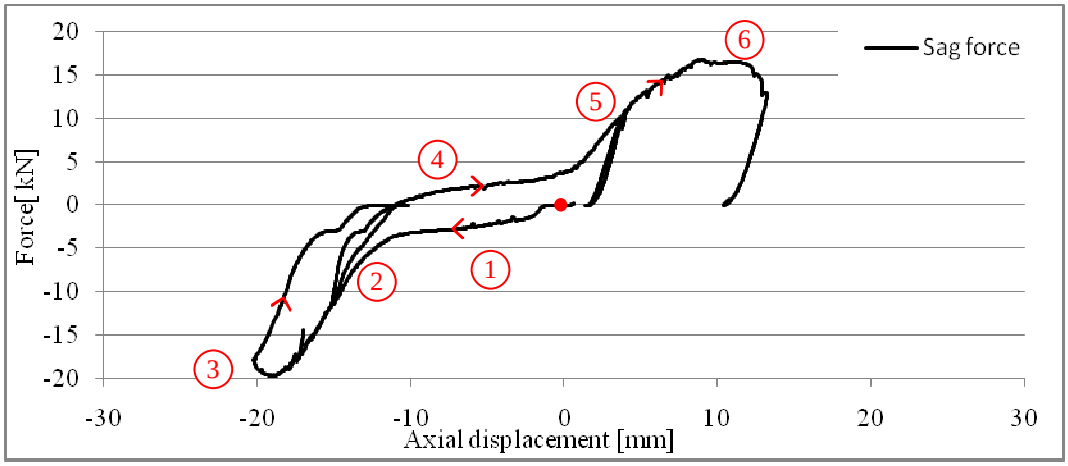

Figure 82. Typical force-displacement curve of sag channel tests for compression and tension

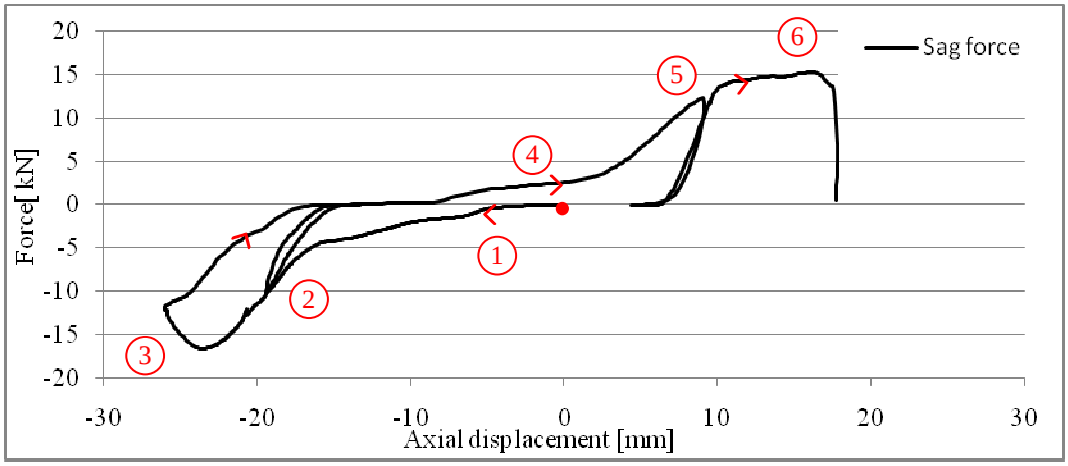

Figure 83. Typical force-displacement curve of adjustable piece tests for compression and tension

The force-displacement curve of the peak element is shown in Figure 84. The behaviour of peak elements for compression is very soft especially in case of large roof slopes (part 1 in the figure). After the local buckling is occurred in the lower flange of the sag channel (point 2) additional load bearing capacity is observed. After failure the load is turned into tension, the global uplift deformation of the structure is turned into downwards movement until the specimen reached the support. This means in this case there is no residual deformation, the specimen moved back to the original position. Tensile failure is occurred at point 4.

The test curves of the flying sag system are shown in Figure 85 for the first test series and for the second test series with improved connection. In the second series the forces in the tie rods are also measured. The first figure shows unloading and uploading loop after 8 kN (~60 % of the ultimate load). Figure 85 shows sudden failure which is not favourable and to avoid this failure type new connection is developed as it is presented previously. The behaviour of the new connection is more ductile and the ultimate load is higher due to the same failure as it is observed in the sag channel tests.

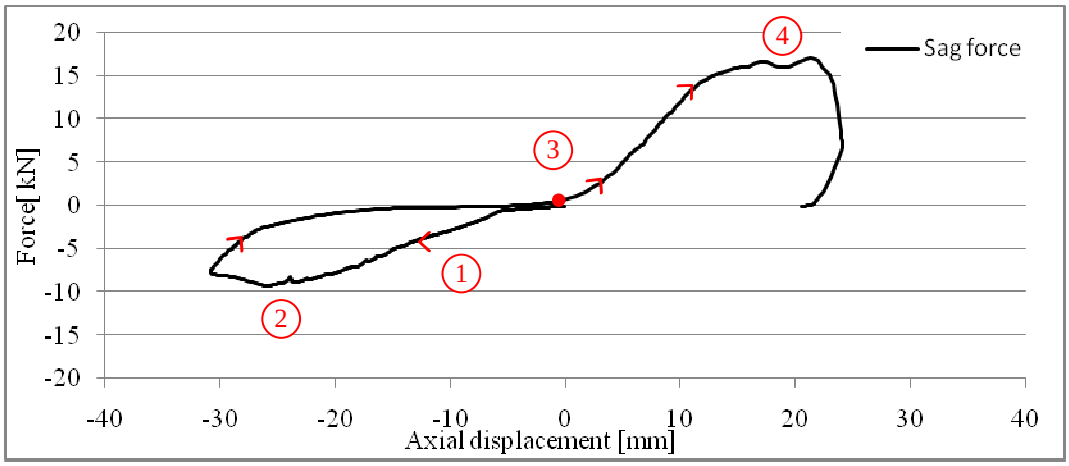

Figure 84. Typical force-displacement curve of peak element tests for compression and tension

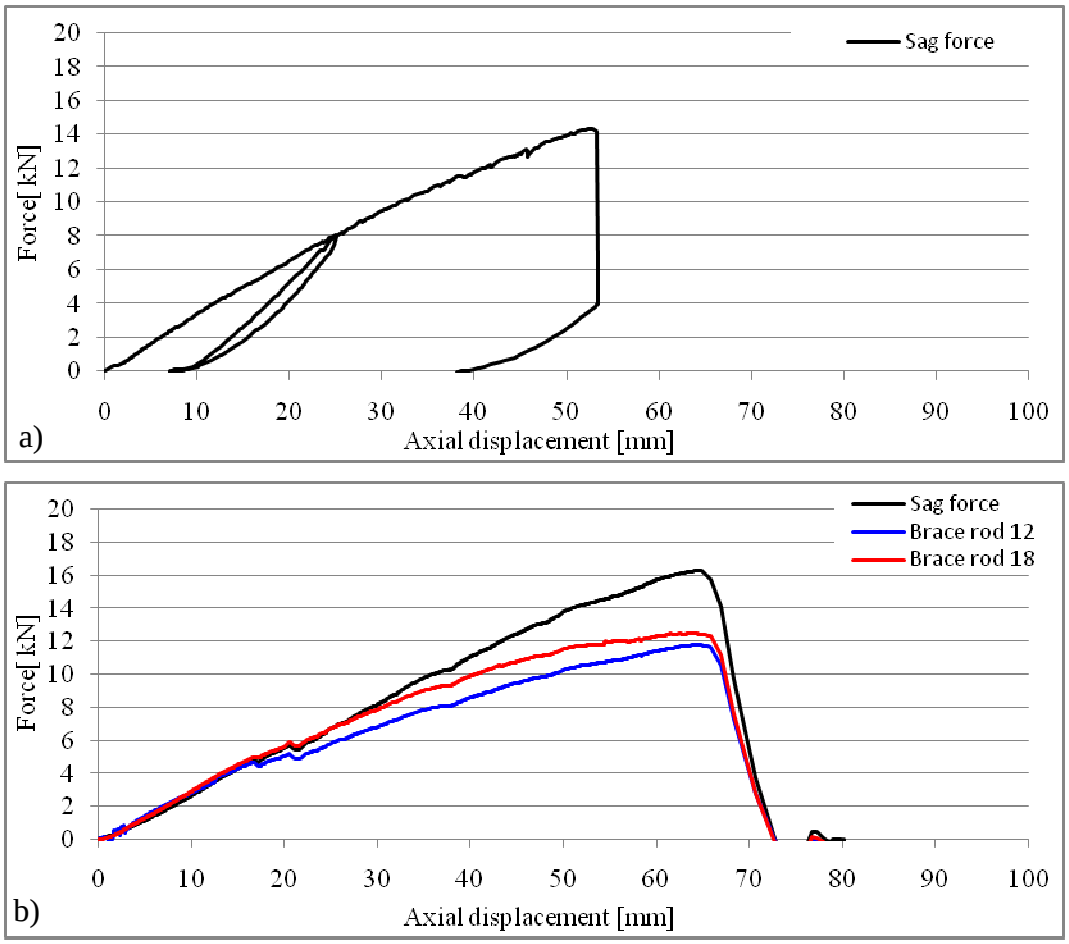

Figure 85. Typical force-displacement curve of the (a) first and (b) second flying sag tests

4.4.3. Test resistances

The test numbers, the test data, the resistances obtained from the tests and the defined failure modes are summarized in Table 33-Table 37.

Table 33. Test results on sag channels

Test #		Section	L [mm]	t [mm]	F^{c}_{Test} [kN]	F^{t}_{Test} [kN]	Failure mode comp.	ten.
1	1	HSG	1550	1.5	-19.72	16.83	c1)	t1)
2	2	HSG	1550	1.5	-18.86	15.54	c1)	t1)
3	3	HSG	1550	1.5	-15.25	17.67	c1)	t1)
4	4	HSG	1550	1.5	-15.11	17.09	c1)	t1)
5	1	HSG	1350	1.5	-26.35	17.01	c2)	t1)
6	2	HSG	1350	1.5	-25.25	18.85	c2)	t1)
7	3	HSG	1350	1.5	-25.59	20.60	c2)	t1)
8	4	HSG	1350	1.5	-25.10	16.56	c2)	t1)
9	1	HSG+holes	1550	1.5	-10.67	18.27	c3)	t1)
10	2	HSG+holes	1550	1.5	-14.35	18.99	c3)	t1)
11	3	HSG+holes	1550	1.5	-13.01	17.82	c3)	t1)
12	4	HSG+holes	1550	1.5	-16.23	16.20	c3)	t1)
13	1	HSG+holes	1350	1.5	-19.01	17.07	c3)	t1)
14	2	HSG+holes	1350	1.5	-11.66	17.16	c3)	t1)
15	3	HSG+holes	1350	1.5	-12.35	15.85	c3)	t1)
16	4	HSG+holes	1350	1.5	-19.27	18.25	c3)	t1)
17	1	HSG	1550	1.5	-	16.53	-	t1)

Table 34. Test results on adjustable test channels

Test #		Section	Bolt position	L [mm]	t [mm]	F^{c}_{Test} [kN]	F^{t}_{Test} [kN]	Failure mode comp.	ten.
18	1	CL226+HSH	1	1550	1.5	-16.63	15.34	c1)	t1)
19	2	CL226+HSH	1	1550	1.5	-16.23	16.51	c2)	t1)
20	3	CL226+HSH	1	1550	1.5	-15.09	17.81	c2)	t1)
21	4	CL226+HSH	1	1550	1.5	-16.03	17.13	c2)	t1)
22	1	CL226+HSH	2	1550	1.5	-18.38	18.54	c4)	t1)
23	1	CL226+HSH	3	1550	1.5	-16.96	18.54	c2)	t1)

Table 35. Test results on peak channels

Test #		Section	L [mm]	t [mm]	F^{c}_{Test} [kN]	F^{t}_{Test} [kN]	Failure mode comp.	ten.
24	1	CL221	692	1.5	-23.81	16.46	c1)	t1)
25	2	CL221	692	1.5	-23.71	17.28	c5)	t1)
26	3	CL221	692	1.5	-19.27	14.81	c5)	t1)
27	4	CL221	692	1.5	-21.08	17.18	c5)	t1)
28	1	CL222	689	1.5	-13.71	17.44	c6)	t1)
29	2	CL222	689	1.5	-13.41	17.34	c6)	t1)
30	3	CL222	689	1.5	-14.32	16.79	c6)	t1)
31	4	CL222	689	1.5	-13.16	15.54	c6)	t1)
32	1	CL223	682	1.5	-9.21	17.07	c6)	t1)
33	2	CL223	682	1.5	-7.94	17.81	c6)	t1)
34	3	CL223	682	1.5	-8.66	18.30	c6)	t1)
35	4	CL223	682	1.5	-7.53	19.63	c6)	t1)

Table 36. Test results on first flying sag system

Test #		Section	Case	α [°]	F^{t}_{Test} [kN]	Failure mode
36	1	CL230+CL231	1	26.8	11.64	t2)
37	2	CL230+CL231	1	26.8	14.32	t2)
38	3	CL230+CL231	1	26.8	13.68	t2)
39	4	CL230+CL231	1	26.8	14.31	t2)
40	1	CL230+CL231	2	27.1	13.95	t3)
41	2	CL230+CL231	2	27.1	13.31	t3)
42	3	CL230+CL231	2	27.1	12.63	t3)
43	4	CL230+CL231	2	27.1	13.48	t3)
44	1	CL230+CL231	1	7.9	9.16	t3)
45	2	CL230+CL231	1	7.9	11.03	t3)
46	3	CL230+CL231	1	7.9	9.76	t2)
47	4	CL230+CL231	1	7.9	11.13	t2)
48	1	CL230+CL231	2	8.8	7.89	t3)
49	2	CL230+CL231	2	8.8	9.16	t3)
50	3	CL230+CL231	2	8.8	7.99	t3)
51	4	CL230+CL231	2	8.8	8.27	t3)

Table 37. Test results on second flying system with improved joint

Test #		Case	α [°]	F^{t}_{Test} [kN]	S^{rod1}_{Test} [kN]	S^{rod2}_{Test} [kN]	Failure mode
52	1	1	26.1	16.31	11.80	12.53	t1)
53	2	1	26.1	17.19	15.42	18.20	t1)
54	3	1	26.1	21.95	16.68	19.86	t1)
55	4	1	26.1	14.04	12.16	14.24	t1)
56	5	1	26.1	14.37	11.89	13.02	t1)
57	1	2	26.4	14.51	-	23.09	t1)
58	2	2	26.4	13.59	-	20.88	t1)
59	3	2	26.4	14.67	0.02	25.30	t1)
60	4	2	26.4	13.28	4.83	30.16	t1)
61	1	1	7.4	13.07	21.75	18.85	t1)
62	2	1	7.4	16.98	17.95	21.06	t1)
63	3	1	7.4	13.22	20.99	18.43	t1)
64	4	1	7.4	15.84	20.37	20.85	t1)
65	1	2	8.2	11.95	10.17	30.53	t1)
66	2	2	8.2	13.65	7.18	40.21	t1)
67	3	2	8.2	12.12	7.94	31.59	t4)
68	4	2	8.2	15.44	9.63	40.00	t5)
69	5	2	8.2	15.21	16.86	39.82	t1)
70	6	2	8.2	14.15	23.79	44.01	t1)
71	7	2	8.2	15.00	14.55	-	t1)
72	8	2	8.2	15.12	16.92	-	t1)

4.5 Material tests

Tensile tests are carried out on specimens cut from various sag channel types, purlins and bolts. The tests are carried out by the AGMI Material Testing and Quality Control Co. Ltd., Hungary.

The results of various sag channel material test are summarized in Table 38. The specimen signs are as follows: SH – sag channels with holes, SP – peak channel element, SF – sag channels without holes and SA – adjustable piece element.

Purlin failure is experienced during the flying sag test; this explains the purlin material tests which are summarized in Table 39.

Bolt failure also experienced in case of flying sag tests. The material test results on BZD12030 bolts are summarized in Table 40. The averages of the 3 measured values are used in the design process for both failure modes.

Table 38. Material test results of sag channels

Material test specimen	The specimen			Yield stress $R_{p0,2}$	Ultimate stress	Ultimate strain
	thickness	thickness without zinc	width			
	mm			N/mm^2		%
SH	1.53	1.49	19.80	444	537	22.5
SP	1.52	1.48	19.72	457	547	15.0
SF	1.54	1.50	19.74	442	537	17.5
SA	1.53	1.49	19.80	450	540	16.5
Average:		1.49	Average:	448		
SAG-2	1.44	1.41	19.60	416	506	21.5
SAG-8	1.45	1.42	19.50	413	509	22.5
SAG-11	1.45	1.42	19.50	410	507	24.5
SAG-18	1.45	1.42	19.60	415	508	20.5
Average:		1.42	Average:	414		

Table 39. Material test results of purlins

Material test specimen	The specimen			Yield stress $R_{p0,2}$	Ultimate stress	Ultimate strain
	thickness	thickness without zinc	width			
	mm			N/mm^2		%
P1	1.54	1.50	20.00	369	489	22.0
P2	1.55	1.51	20.20	361	485	24.0
P3	1.54	1.51	20.30	366	489	22.5
Average:		1.51	Average:	365		

Table 40. Material test results of BZD12030 bolts

Material test specimen	The specimen outside diameter		Ultimate force	Position of failure
	Minimum	Maximum	F_{max}	
	mm		N	
B1	11.57	11.75	44700	bolt thread
B2	11.50	11.74	43200	bolt thread
B3	11.70	11.75	43900	bolt thread
Average:	11.67		43933	

4.6 Evaluation of test results

4.6.1. Evaluation method

The test results of each test series are evaluated to define the standard design resistances according to the Eurocode 3 [60]. In case of four tests the adjusted and characteristic values are calculated for $f_{yb} = 390$ N/mm^2 nominal yield stress as follows:

$$R_{adj,i} = R_{obs,i} / \mu_R \,,\; R_m = \frac{\sum R_{adj,i}}{4} \text{ and } R_k = R_m +/- k \times s \tag{18}$$

where μ_R is calculated according to Eq. (2), and for bolt failure:

$$\mu_R = \left(\frac{F_{u,obs}}{F_u} \right)^{\alpha} \tag{19}$$

$F_{u,obs}$ is the measured ultimate force of the bolt,

F_u is the nominal ultimate force of the bolt,

$\alpha = 1$ if $F_{u,obs} > F_u$, otherwise $\alpha = 0$.

and k is a coefficient from the standard, if the number of tests is 4 then $k = 2.63$,
and s is the standard deviation:

$$s = \sqrt{\frac{\sum_{i=1}^{4} (R_{adj,i} - R_m)^2}{4-1}} \tag{20}$$

The design value can be calculated as follows:

$$R_d = \eta_{sys} \times \frac{R_k}{\gamma_M} \tag{21}$$

$\eta_{sys} = 1$ because the test conditions followed the applied solution and $\gamma_M = 1$ partial factor is applied (according to Eurocode and the National Annexes [59]).

For the bolts the following nominal values are used: tensile stress area: $A_s = 84.3\, mm^2$, ultimate force: $F_u = A_s \times f_u = 84.3 \times 400 = 33720\, N$.

There are 3 cases (tests 17, 22 and 23 in Table 25) where only one test is carried out, in those cases the characteristic value is calculated as follows:

$$R_k = 0.9 \times \eta_k \times R_m \tag{22}$$

where $\eta_k = 0.9$ because the observed failure is yielding failure, which is true for the tension failure and $\eta_k = 0.7$ because the observed failure is overall instability, which is true for the compression failure modes. For Case 2 tests with $\alpha = 8.8^\circ$ where both failure modes are experienced the characteristic value is calculated according to two tests as is shown in Eq. (13), where $\eta_k = 0.9$ is applied because the observed failure is yielding failure. The design resistances are summarized in Table 41. Note that for the adjustable piece (CL226+HSH) the minimum design resistance for compression is shown.

Table 41. Design resistances of various sections for compression and tension

Section	L [mm]	Design resistances compression [kN]	tension [kN]
HSG	1550	-9.64	12.72
HSG	1350	-21.27	11.82
HSG+holes	1550	-6.52	12.92
HSG+holes	1350	-4.14	12.73
CL226+HSH	1550	-9.32	12.16
CL221 - 6%	692	-14.00	11.62
CL222 - 10%	689	-10.67	12.52
CL223 - 20%	682	-5.50	13.30

The design resistances for flying sag systems are summarized in 0. The tensile force in one tie rod is calculated according to the equilibrium equations on the final-deformed-geometry, Figure 86 and Eq. (23)-(26), in case of the first test series. The angle of the tie rods at the failure is calculated from the start angle and the deformation in the direction of the sag channel what is measured during the tests. For Case 2 (where the additional lateral support is applied) the force in the sag channel is reduced by the friction resistance of the support, as shown in Figure 86. The second series of flying sag system contains measured forces in the tie rods in Table 42.

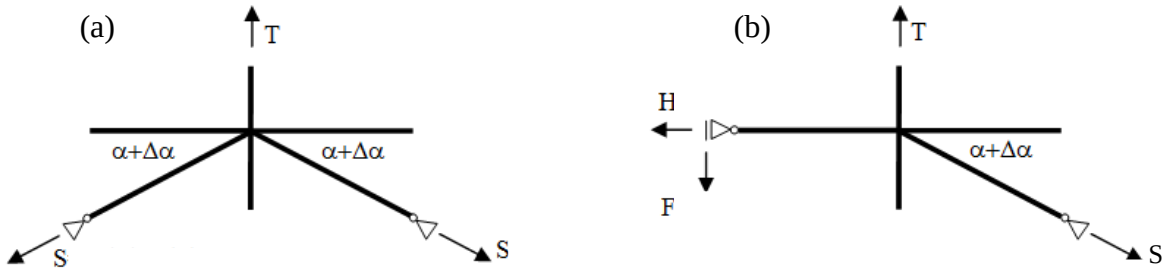

Figure 86. Calculation of the force in the tie rods – (a) Case 1 and (b) Case 2

$$S = \frac{T}{2\sin(\alpha)} \quad \text{for Case 1} \tag{23}$$

$$S = \frac{T - 0.06}{\sin(\alpha + \Delta\alpha) + \cos(\alpha + \Delta\alpha)/1000} \quad \text{for Case 2} \tag{24}$$

$$H = \frac{T}{\tan(\alpha)} \tag{25}$$

$$F = 0.06\ \text{kN} + 0.001H \tag{26}$$

Note: the 0.06 kN is the initial friction force of the lateral support.

Table 42. Characteristic resistances of various configurations of the flying sag tests

Section	Case	α [°]	Failure mode	Characteristic resistances	
				tension force in the sag channel, T [kN] measured values	tension force in one tie rod, S [kN] calculated and measured values
CL230+CL231	1	26.8	t2)	10.02	10.67
CL230+CL231	2	27.1	t3)	9.07	19.00
CL230+CL231	2	8.8	t3)	6.97	15.86
			t2)	9.28	20.76
CL230+CL231	1	7.9	t3)	5.14	20.82
CL230+CL230	1	26.1	t1)	11.22	7.56
CL230+CL230	2	26.4	t1)	11.94	14.09
CL230+CL230	1	7.4	t1)	9.45	15.58
plate+CL230	2	8.2	t1)	12.91	36.87
plate+plate	2	8.2	t1)	13.25	-

4.6.2. Conclusion on the test results

Altogether 72 tests are designed and fulfilled on anti-sag system elements and the failure modes are determined for each element. The various sag channel test (main element, adjustable piece, peak element) showed similar failure modes for tension in the bolted connection of the sag channels, which results close design resistances for tension. The flexural-torsional compression resistances depend and vary according to the member length as it is expected. The various failure modes of the peak elements are also determined.

The first test series of the flying sag system showed large deformation in unsymmetrical cases. The design values correspond to large deformation of the connection, which usually cannot be developed in a real structure. The serviceability limit of this connection type can be determined from the force-displacement curves of those tests, where the design forces belonging to a maximum allowable displacement level.

To reduce the deformation of the system and increase the tensile resistance of the joint new structural detail is developed. The experimental tests of the improved connection certified that the failure mode of the new flying sag system occurs in the sag channel which was the weakest point in the previous tensile details.

In the research the design resistances of the various elements are also determined.

4.7 Numerical model of the sag channel

Shell finite element models of the sag channels are developed under my guidance by student T. Curávy for the Student Scientific Conference [45]. The aim of the study is to model the behaviour modes of the main part of the anti-sag system for compression. The details of the FE model are presented in this chapters. The model results are verified by the experimental tests and the appropriate equivalent geometrical imperfections are determined for virtual tests.

4.7.1. Shell finite element model

The shell finite element model of the sag channel is developed in Ansys FE program [64]. The model geometry corresponds to the real geometry of the sag channel: the large web holes and the end details with bolt holes are modeled, respectively. Two mesh densities are used: around the bolt holes the largest element size is 1 mm while in the undisturbed zone the least

density is 12 mm. The small mesh size is necessary for the proper modeling of the holes and the applicability of the large mesh size is proved by convergence studies. The full model and the details can be seen in Figure 87. The thickness of the model corresponds to the measured values in Chapter 4.5.

Shell finite element called SHELL181 in Ansys is used to be able to follow the material nonlinearities and large displacement during the virtual tests. The number of nodes is ~6000, the number of elements is ~5500 and the total number of DOF's is ~36000.

The end support and load is applied in the center of the bolt holes with constraint equations. The load is applied by force or by displacement according to the analysis method that are detailed later on. This results exact eccentric load application as it was in the experimental tests, however in the model the gap in the bolted connection is not considered.

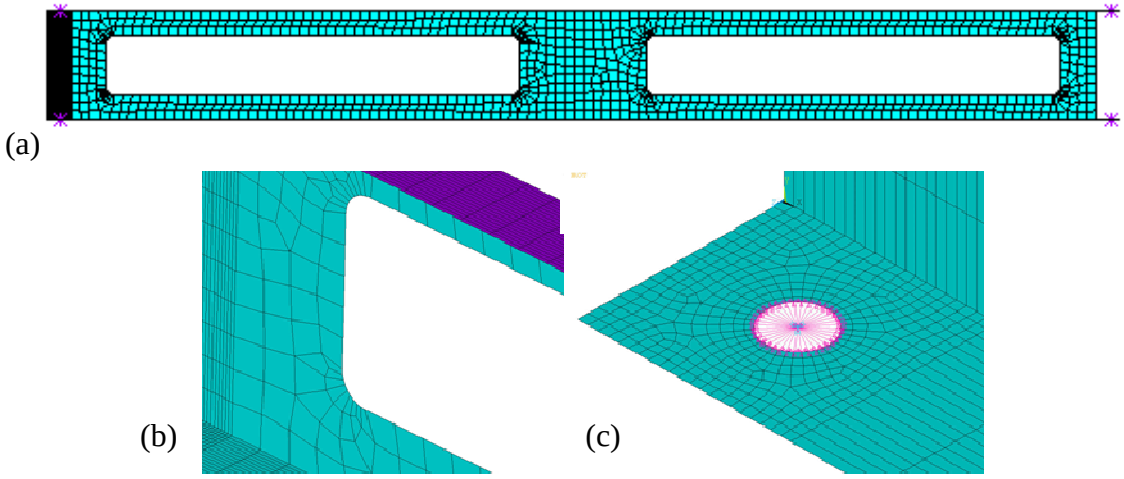

Figure 87. FE model: (a) global mesh, (b) the corner of the web hole and (c) the bolt hole

4.7.2. Results of linear analysis

The model tested by linear analysis for compression. The deformed shape is shown in Figure 88. It can be observed that the eccentric load cause bending about the minor axis of the cross-section.

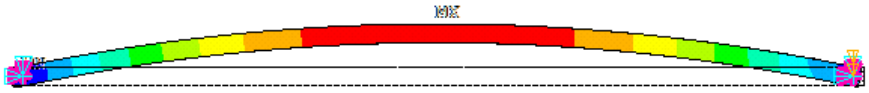

Figure 88. Linear analysis – deformation under compression

4.7.3. Results of instability analysis

Instability analysis is carried out on the shell model and three typical modes can be seen in Figure 89. The first mode is flexural-torsional; the second mode is flexural but the local buckling of the flanges can be observed as well; the third mode is local and contains the deformation of the unrestrained flanges at the web holes. There are other modes with higher critical load factor which are local modes with various patterns in the flanges.

These three buckling modes are used as the shapes of equivalent geometrical imperfection which means that the perfect FE model geometry is modified by the displacements of these modes. Either one mode or combination of several modes is used.

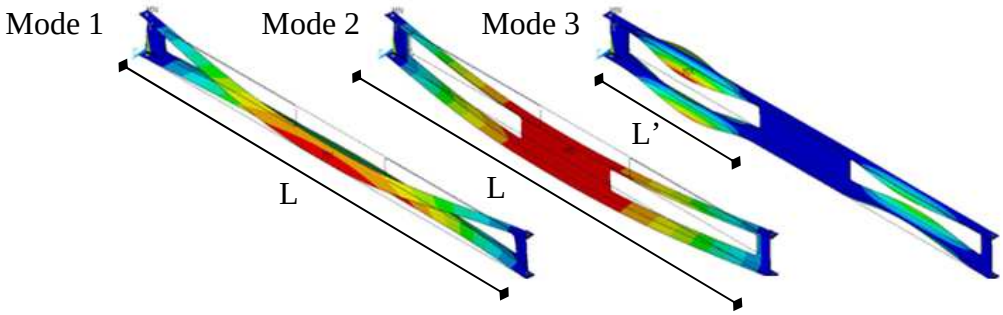

Figure 89. Three buckling modes of the sag channel FE model

4.8 Virtual test on sag channels

The material and geometrical nonlinear FE simulation is carried out as virtual tests. (The definition of a virtual test is presented in Chapter 3.7.3.)

The Eurocode 3 contains suggestion to the size and the distribution of the equivalent geometrical imperfection in [59] and [61] which can be used for welded or hot-rolled sections only. In the current experimental based numerical research the proper imperfections are determined to obtain the same behaviour mode and ultimate load as it was observed during the tests.

4.8.1. Finite element model for virtual test

The FE model is modified according to the requirement of the virtual tests. Linear elastic – perfect plastic material model is applied with the measured yield stress.

The geometry of the FE mesh is modified according to the first three buckling modes presented above. In case of sag channel length 1550 mm with web holes (Test 9-12) in Table 25 the following amplitudes and combination of the modes are applied:

- 1. mode: L/110-L/30,
- 1. and 2. modes: L/150-L/42 and L/150-L/30,
- 1. and 2. and 3. modes: L/150-L/110, L/120 and L’/50,

where L is the member length (1550 mm in this example), L’ is the length of the web hole (532 mm) and the result value is the maximum displacement perpendicular to the longitudinal axis of the sag channel. Altogether 18 virtual tests are carried out to analyse the imperfection sensitivity. The other section types such as sag channel without web holes and member length are also modeled but the results are not presented here.

4.8.2. Virtual test results

The results of the virtual tests are the force - axial displacement curves and the failure modes. In all cases the virtual test failure modes are the same as in the experimental tests. The tests results of the experimental tests of sag channel length 1550 mm with web holes (Test 9-12) are shown in Figure 90. It can be observed that there is a big scatter in the ultimate load of the experimental tests; the ultimate load varies from 10-16 kN.

Various equivalent geometrical imperfections have effect on the stiffness of the compressed member which modifies the gradient of the force - axial displacement curve and it has effect on the ultimate load, too. The stiffness of the FE model is usually higher than in the test due to the lack of exact modeling of the loose bolted connection at the ends. It can be concluded from the parametric studies that the smallest ultimate load from the test can be achieved by L/42 and the largest ultimate load with L/110 imperfection amplitude of the first buckling mode, where L is the member length. These two curves are shown in Figure 90 as well.

The same imperfection amplitudes can be applied on the sag channels with 1350 and web holes (Test 13-16). By the application of the verified imperfection L/42 the ultimate load of the test can be determined within 5%.

The FE model of the sag channel without web holes are verified with the experimental results, too. In those cases the minimum ultimate load of the tests can be determined by the application of L/15 imperfection amplitude of the first buckling mode.

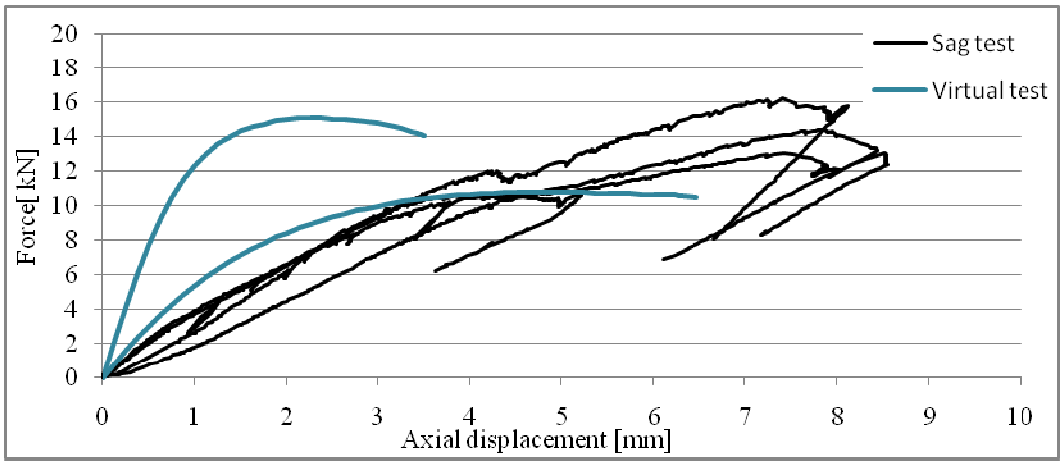

Figure 90. Test results and virtual test

4.8.3. Conclusion on numerical results

The shell FE model of the main part of the anti-sag system is developed and the model results are verified with the experimental tests. Virtual test are carried out on compressed sag members with various length and web holes. By virtual tests the shape and amplitude of the equivalent geometrical imperfections are determined. The size of the imperfection is determined according to the test results to reach the minimum ultimate load of the tests.

The verified numerical model is capable to extend the experimental test program for further lengths and structural arrangements and the results can be used in the test based design procedure to determine design resistances. Furthermore it can be built into the FE model of a roof system.

5. FE and experimental based design methodology of roof systems

5.1 Introduction

5.1.1. Structural and design problems

The structural problems of cold-formed thin-walled roof systems are presented in my research by the experimental and numerical analyses of its various components. The problem of compressed Z-purlins is presented in Chapter 2. The overlap region and end support of continuous purlin system is analysed in Chapter 3. The structural problems of anti-sag elements of the roof system are brought on in Chapter 4.

The restraint effect of the cladding to the purlin leads to new complex structural problems. Various types of cladding systems are exist in the industry that represent rotational and lateral restraint to the purlin which must be handled in the design.

It can be clearly seen that the structural arrangement of cold-formed thin-walled roof systems are very complex, which leads to complicated behaviour modes and require sophisticated design methodology.

5.1.2. Previous studies

The previous studies of the roof system components are presented in the previous chapters. Here only the previous studies of the purlin-cladding interaction and the applied design methods are discussed.

The rotational effect of the cladding system to the behaviour of Z-purlins is analysed by GBT in a simplified way formerly in [43] for engineers. Experimental tests are carried out on analysing the full or partial restraining effect of the sheeting on Z- and ∑-sections in laboratory in [44], or by full-scale site tests in [47]. The effect of the joint elements between the sheeting and the purlin is analysed by small component tests of the region, e.g. in Hungary in [46], as it is proposed in the standard [60]. In parallel with the experimental tests the development of finite element model is started on C- and Z-section purlins together with the sheeting, [49], [48], or by local model of the joint region, [50].

The European standard [60] handle the restraining effect of the sheeting by rotational spring on the top flange of the purlin, and the buckling of unrestrained flange is calculated as a beam on elastic foundation. Papers can be found on the literature with the purpose to refine the spring constants and the design method: [51], [52], [53].

5.1.3. Conclusions on previous studies

On the basis of the existing research studies the following conclusions can be drawn:

- the lateral and rotational restrain effect on the local and distortional buckling modes of Z-purlins is widely analysed in the literature by both analytical and theoretical ways,
- the standard design methods on restrained Z-purlins do not cover all the structural arrangements applied in the industry.

In the investigated literature I did not find:

- research to cover the behaviour of the overlapped region together with the restraining effect,
- finite element model which combines behaviour modes of the overlap region and the cladding system,
- complex algorithm, which can combine numerical model of all components of cold-formed thin-walled roof systems.

5.1.4. Purpose and research strategy

The local purposes of the examined components of roof systems are presented in the previous chapters. The research of compressed Z-sections, continuous purlins and anti-sag elements led to the test based design resistances of each component. Furthermore, shell numerical models are developed of all components and partially the details of nonlinear simulation methods and necessary equivalent geometrical imperfections are verified by experimental tests in all cases.

The global purpose of the dissertation is to develop a complex design method of thin-walled roof systems that is applicable for practical design purpose. Various model and analysis levels are worked out from the beam model to shell finite element models, and from linear analysis to nonlinear simulations on imperfect models. The models of the roof system summarize the experiences on finite element modeling of cold-formed thin-walled members gathered during my research:

- behaviour modes of compressed Z-purlins,
- buckling mode classification and imperfection sensitivity analysis,
- behaviour modes of overlap region,
- rotational restraining effect of various cladding system,
- behaviour modes of anti-sag system.

The basic idea of the complex design method are implemented into an algorithm what controls the various model levels, and automatically can build the shell finite element models and evaluate the results of different analysis levels. The developed algorithm presented in Chapter 5.2. The models are presented in Chapter 5.3 and the design methodologies are detailed in Chapter 5.4.

5.2 Target program for roof design – PurlinFED

A target program, called PurlinFED (Purlin Finite Element Design), is developed in Matlab [65], what can prepare the data for design of roof systems. In this chapter the characteristics of the algorithm are presented. The available design methods are shown in a flowchart in Figure 91.

The developed algorithm is able to model the whole roof system. The input data are the followings:

- section: parametric or standardized C- and Z-sections,
- geometry: spans, purlin distances, overlap lengths, places of purlins, places of anti-sag bars and roof slope,
- material: linear elastic, linear elastic-hardening plastic model,
- cladding: parametric or unique floating or trapezoidal sheeting,
- various surface loads and
- support models.

There are two model levels in the program: a beam model of purlins and a shell finite element model of the full roof system. The details of the shell model are presented in Chapter 5.3. Different analysis can be handled by PurlinFED. Linear analysis is applied on beam model, while instability analysis and nonlinear simulation on imperfect model is carried out on the shell model. The eigenmode classification detailed in Chapter 2.4.3 is also built in the program. The program window can be seen in Figure 92. The three design methods are detailed in Chapter 5.4 and marked with different colors in Figure 91.

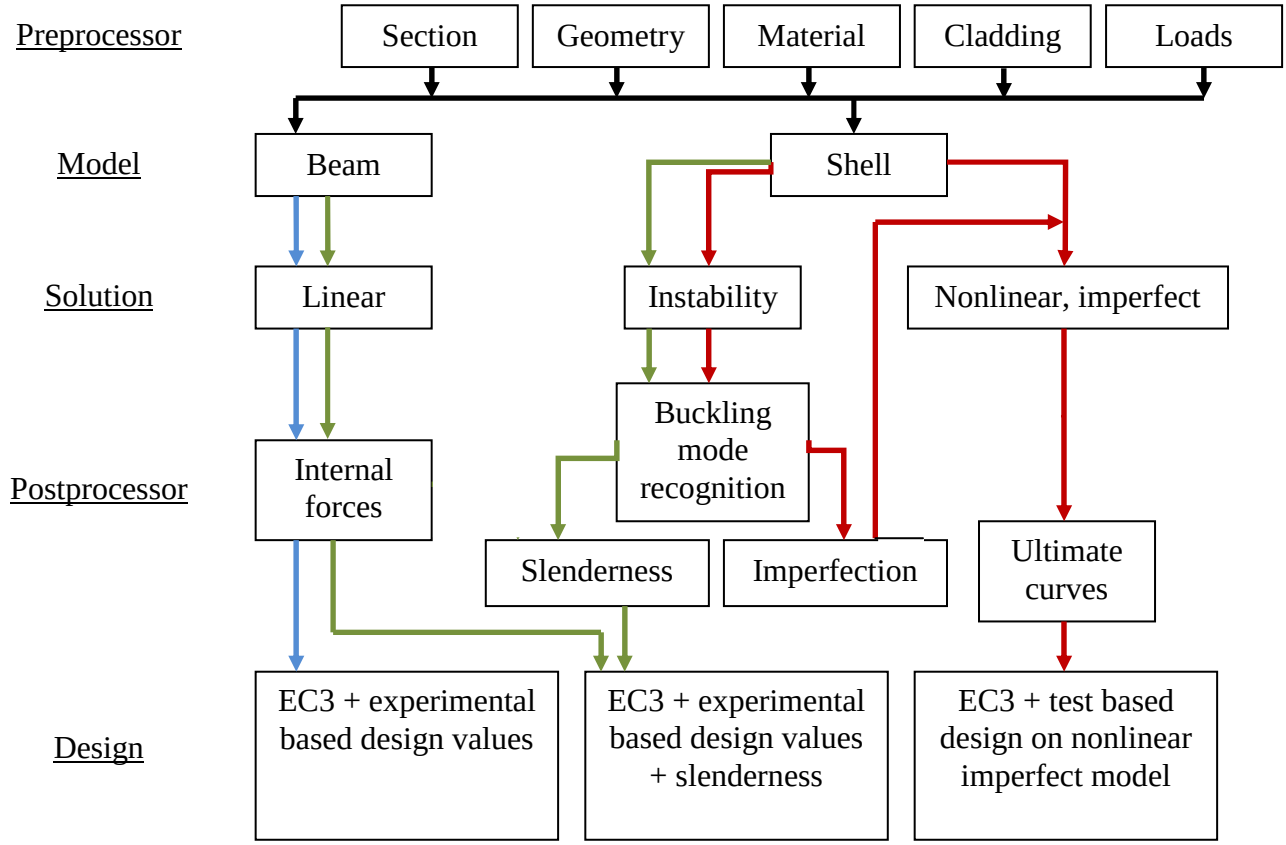

Figure 91. PurlinFED algorithm

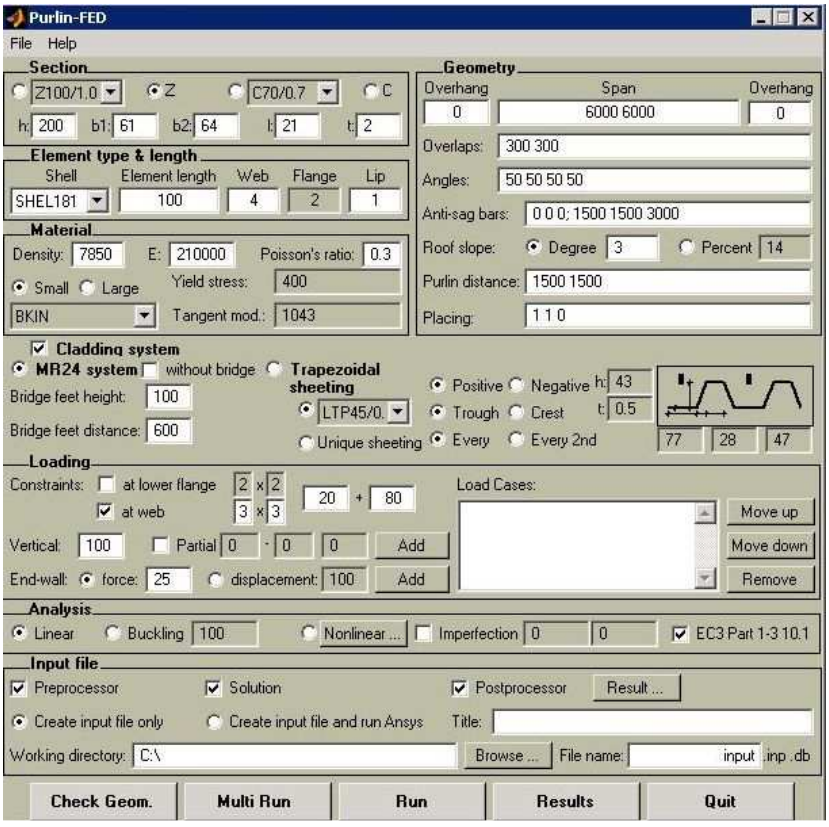

Figure 92. PurlinFED program window

5.3 Finite element model of roof system

Shell numerical models are developed in Ansys [64] general purpose finite element software. The Matlab based PurlinFED program generates the input file on Ansys Parametric Design Languages.

There are two types of roof systems, which can be modeled: trapezoidal sheeting (Figure 11), and floating cladding system. The typical segment of the roof system consists of three purlins, which are modeled by 4-node-shell elements. The webs of purlins are divided equally into four parts; both flanges into two parts and both lips consist of one element in the cross section, as it can be seen in Figure 93. The length of elements in longitudinal direction is 50 mm to get nearly square mesh in the web and a maximum 1/3 aspect ratio in the lip. Other mesh densities can be applied as well. In the double span model the overlap over the middle support is modeled by shell elements with double thickness. More advanced model of the overlap region of the two purlins is developed based on the experimental results in Chapter 3. Supports are applied on the lower flange, as in the experimental tests. However it is remarked that the more detailed support conditions have influence on the critical load factor and design resistance [56].

The specialty of the MR24 cladding system floating roof is the roof panels connection to each other with seams. In the FE model roof panels are modeled with shell elements. The seams are modeled with eccentric beam elements to consider its bending stiffness. The other specialty is the bridge system, where the bridge feet are modeled with shell elements, connected to the top of the purlin flange and to the roof panels. Over the purlin, in longitudinal direction beam elements are running with the cross-section of the bridge, which are also connected to the bridge feet and to the roof panels. The system contains transverse anti-sag bars and angels to support the lower flange of the main girder in horizontal direction. Angles can be modeled as simple horizontal support while the anti-sag bars as coupled nodes on each purlin webs connected to horizontal spring elements. More advanced model of the sag channels is developed based on the experimental results as detailed in Chapter 4. These spring elements model the supporting effect of the other – not loaded – part of the roof. The full model of the typical roof section consists of about 10000 elements depending on the structural arrangement.

5.4 Design methodology

In the typical roofs of steel industrial type buildings cold-formed purlins, as secondary structures, are used to support the load-bearing elements of the cladding system. The main characteristics of the behaviour of the typically used C-, Z- or ∑-sections are coming from the coupled plate and distortional buckling and lateral torsional global buckling modes. These phenomena are highly influenced by the structural arrangements of the purlin and cladding system [44]. The lateral and torsional supporting effect of the cladding to the purlin is influenced by several structural parameters what can be hardly considered without experimental studies.

In the existing design codes the application rules use semi-empirical formulations with significant simplifications. It is proved that the purlin design method of Eurocode 3 [60] is conservative and benefits can be gained by improving the analysis model [56].

5.4.1. Design method based on beam model

The design method proposed by the Eurocode 3 is built in the PurlinFED program. The internal force distribution is calculated on a self-developed beam model. The rotational restraint of the cladding system is taken into account by the application of the Eurocode 3 procedure [60].

The more sophisticated design method – use the research results of the dissertation – is under development. The determined inertia factors in the overlap zone by the overlap tests (Chapter 3.5.4) to be implemented in the internal force calculation of the beam model. This modification takes into account the real distribution of the internal forces. The design of the end of overlap and end support resistances are based on the proposed design methods in Chapter 3.6.

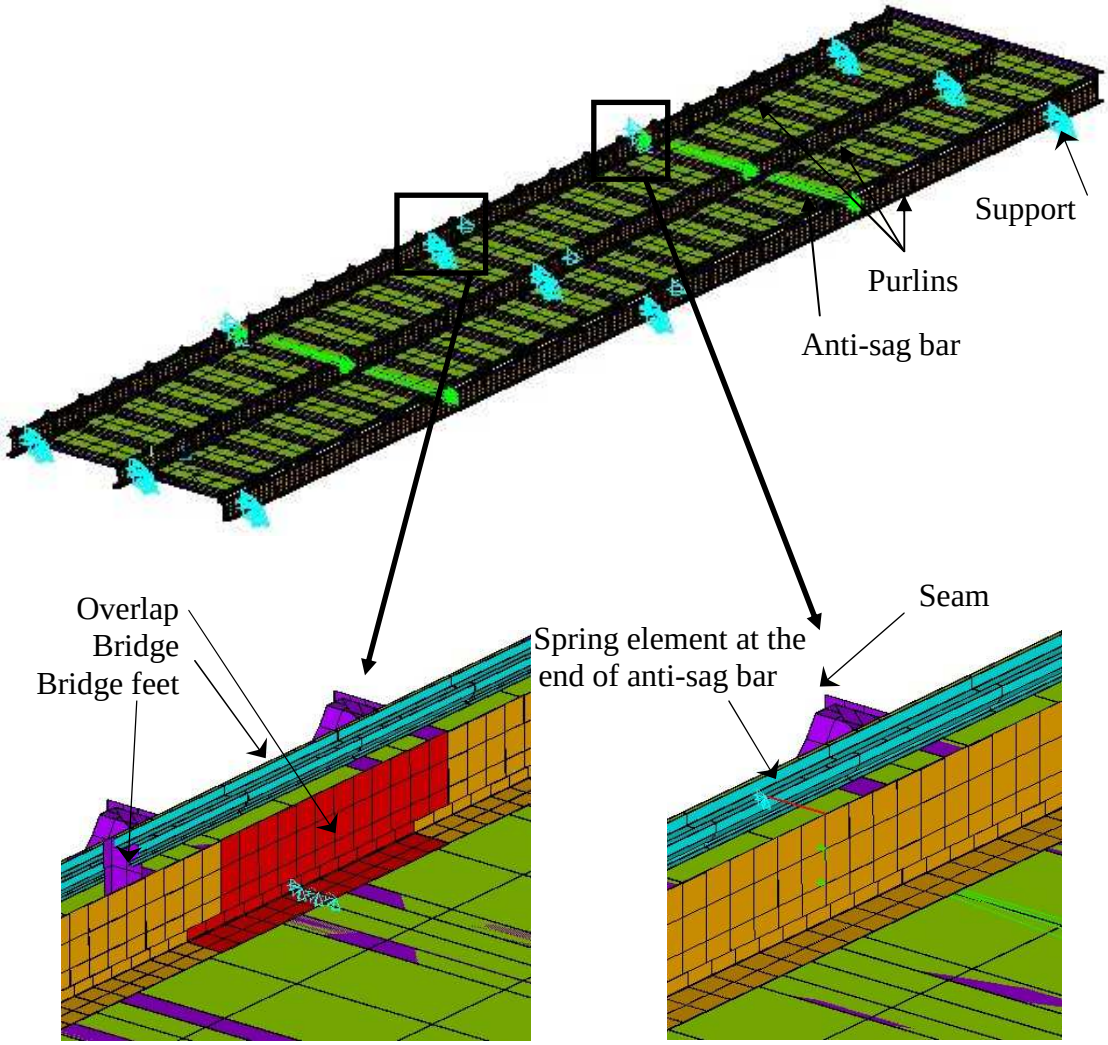

Figure 93. FE model details of the floating roof

5.4.2. Design method based on shell finite element buckling modes

In this case the same procedure is used as detailed previously, except that the calculation of rotational effect of the cladding system is based on the shell FE model. The full model of the roof systems takes into consideration the real rotational rigidity of the cladding system. The slenderness of lateral torsional buckling can be determined by instability analysis of the shell FE model. The automatic buckling mode classifications – detailed in Chapter 2.4 – help to choose the pure lateral torsional buckling mode. The reduction factor for stability checking is calculated from the numerically determined slenderness.

5.4.3. Design method based on nonlinear simulation on imperfect model

The most complex design method is the nonlinear simulation of imperfect shell finite element models. In the Eurocode 3 [61], design methods can be found, which details the application of shell finite elements, the size of the equivalent geometrical imperfections, the material models and other details of the modeling for welded and hot-rolled sections. In this case the nominal yield stress has to be applied and the ultimate load can be directly compared to the design loads. The problem of the Eurocode 3 1-3 standard for cold-formed sections is that there is no equivalent geometrical imperfection is specified, experimentally verified imperfection sensitivity analysis is needed what is presented in the previous chapters for the same cases.

To illustrate the applicability of the proposed algorithm, the results are compared qualitatively to the ultimate behaviour of a special purlin-cladding system studied by a full-scale experimental program [47]. The details of the experimental research are not presented here, only two failure modes are illustrated by photos and the FE model.

In the nonlinear analyses four failures types occur, as they are presented in Figure 94. The first failure is the upper flange elastic distortional buckling. This mode occurs if the upper flange is slender due to the high lip or flange width to thickness ratio, or to the long lateral supporting distance (1200 mm) Figure 94a.

If the upper flange is supported laterally in smaller distances (600 mm) but slender enough to initiate the buckling, plastic distortional buckling occur, as in case of structural arrangement, Figure 94b.

If both the upper flange supporting is efficient and the flange slenderness is small, the distortional buckling cannot be occurred. In this case the phenomenon is plastic failure with high horizontal displacement of the lower flange, as it can be seen in Figure 94c.

The local failure mode is the web buckling at the end of the overlap near to the middle support. If the length of the overlap is relatively small (300 mm), the shear becomes dominant.

The experienced failures of the full-scale tests are presented in Figure 95. By the qualitative comparison of the results it can be concluded that the full FE model of the roof system built up by PurlinFED is can follow the behaviour of a full-scale experimental test.

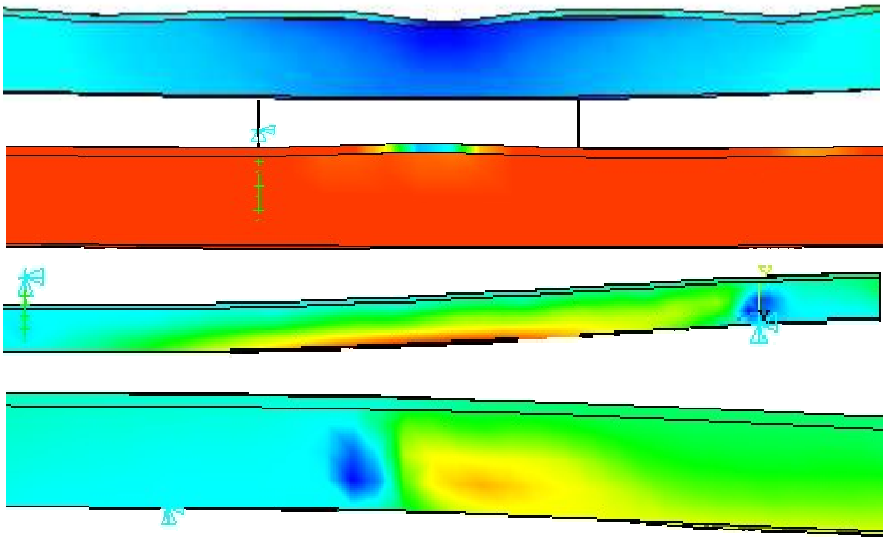

Figure 94. Simulated failure modes: (a) upper flange distortional buckling, (b) upper flange distortional buckling with plastic defomations, (c) lower flange deformation with high tension stress, (d) web buckling at the end of overlap

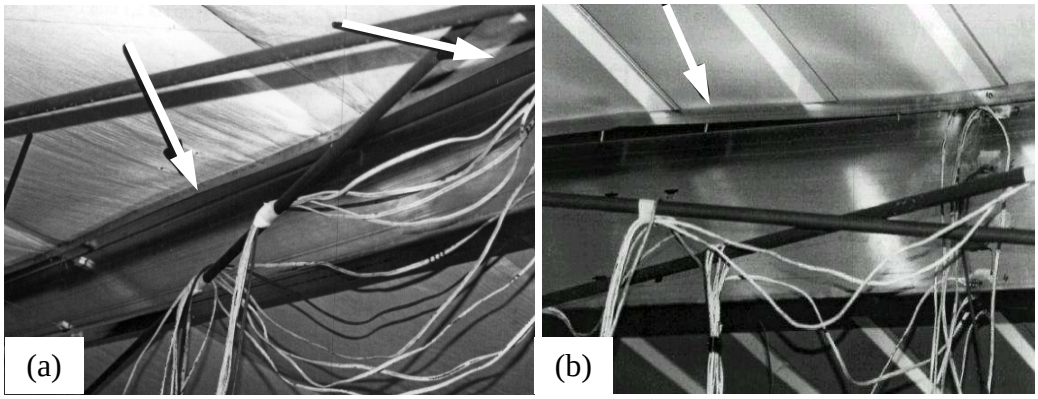

Figure 95. Observed failure modes: (a) elastic distortional buckling and (b) plastic distortional buckling

5.5 Conclusions and further studies

The illustrative example of the proposed algorithm showed that it is able to model the real behaviour of a full roof-cladding system. The FE models of other complex details of the system are already exists and they are also able to model the real behaviour of purlins, purlin joints and anti-sag system elements. It can be concluded from the research results that shell finite element models of all components of a thin-walled roof system are developed and the complex model can be build with the PurlinFED algorithm and this algorithm helps in the evaluation of the results as well.

Further numerical benchmark tests and parametric studies are needed to calibrate the proposed design method and to compare the results to the Eurocode proposals. The final aim of the research program is to improve the accuracy of the standards design method and to develop a user friendly advanced design tool for engineers.

6. Summary and conclusions

6.1 New scientific results

6.1.1. The theses of the PhD dissertation in English

The presented research and its scientific results can be summarized as follows:

Thesis 1

I worked out and completed an experimental test program on compressed cold-formed thin-walled cold-formed Z-section members by different lateral support conditions and load introduction, which are not analysed previously.

a) I experimentally defined the local, distortional and global behaviour modes of single Z-section members under compression.
b) I defined the behaviour modes of compressed Z-section members laterally restraint by trapezoidal sheeting.
c) I analysed the behaviour of overlapped zone of short double Z-section members under compression.

Based on the experimental results I defined the test based design resistances of the studied compressed Z-section members.

Thesis 2

I developed a shell finite element model to be able to follow the behaviour of compressed Z-section members. By the model I completed an imperfection sensitivity analysis by geometrical and material nonlinear analysis. The equivalent geometrical imperfection was chosen according to the buckling modes of the model. I determined the effect of various types of buckling modes to the stiffness, the ultimate load and the ultimate behaviour of the structure. The classification of the buckling modes was performed by two ways:

a) I worked out a method for the classification of the eigenmodes of shell finite element models, based on the geometrical definition of the buckling modes. The algorithm of the proposed method is built in a computer program developed for the FE analysis of cold-formed thin-walled roof systems.
b) I performed a parametric study on classification of eigenmodes of thin-walled C- and Z-section members by base functions of the constrained Finite Strip Method. I determined the participation of local, distortional and global buckling modes in case of various support conditions and mesh density and I proved the applicability of the method.

Thesis 3

I worked out and completed an experimental test program on various components of a continuous Z-purlin system. The specialty of the structural arrangement of the overlapped joint can be described as follows: (i) the width of the two flanges are the same, so the connection is prestressed and tight, (ii) the diameter of the holes of the bolts between the two purlins are significantly higher than the diameter of the bolts, and (iii) there is no bolt at the middle of the overlap in the web. I determined and characterized the behaviour modes and the test based design resistances for the following cases:

a) I determined the test based design resistance of the end of overlap for various bending moment and shear force ratios. Based on the results I worked out a Eurocode 3 based design method for bending moment shear force interaction at the end of overlap.

b) I determined the test based design resistances of the middle of the overlap for various bending moment and transverse force ratios. Based on the results I proved that the Eurocode 3 design method is applicable for the overlap region.
c) I determined the test based design resistances of the end support of a continuous purlin system. Based on the results I proposed the modification of the Eurocode design method.

I developed shell finite element model of the applied overlap joint and I characterized the behaviour modes of the end-of-overlap and overlap support zones by the applied numerical studies.

Thesis 4

I worked out and performed an experimental test program for anti-sag elements of a cold-formed thin-walled roof system. I characterized the behaviour modes and determined the test based design resistances of the following components:

a) Cold-formed thin-walled U-shape sag channel under compression and tension. Two configurations are analysed: web with or without large openings.
b) Adjustable piece element of the sag channel under compression and tension. I characterized the behaviour modes of the adjustable elements for various bolt positions.
c) Peak element of the sag channel under compression and tension in case of various roof slopes.
d) Flying sag systems in symmetrical and unsymmetrical structural arrangements.

I developed a shell finite element model of the sag channel. I characterized the failure modes of the model and determined the equivalent geometrical imperfection by virtual tests.

Thesis 5

I worked out the bases and the algorithm of a complex design methodology of cold-formed thin-walled roof systems. The design method joins together the (i) test based design resistances of the components that have no standardized background and (ii) the Eurocode 3 based nonlinear simulation on imperfect shell finite element models. The developed algorithm – called PurlinFED – contains three design levels for roof systems:

a) beam model extended with the experimentally determined overlap rigidity and proposed design methods for end of overlap and end support,
b) beam model extended with the shell finite element based buckling analysis, where the slenderness are determined from the full FE model of the roof system that contains the real rotational support provided by the cladding system to the purlin, and
c) shell finite element model, where material and geometrical nonlinear simulations are carried out on imperfect model, the imperfections are based on the buckling modes of the purlin, which is classified by the built in buckling mode recognition algorithm.

6.1.2. The theses of the PhD dissertation in Hungarian

Az ismertetett kutatás és annak tudományos eredményei a következőképpen foglalhatók össze:

1. tézis

Megterveztem és végrehajtottam egy kísérleti programot eddigiekben nem vizsgált hidegen alakított vékonyfalú Z-szelvényű nyomott elemek vizsgálatára különböző oldalirányú megtámasztási viszonyok és speciális erőbevezetés esetén:

a) Kísérleti úton meghatároztam oldalirányban megtámasztatlan Z-szelvényű elemek lokális, torzulásos horpadás, illetve globális stabilitásvesztési módjait.
b) Meghatároztam egyik övén trapézlemezzel megtámasztott Z-szelvényű nyomott elemek viselkedési módjait.
c) Rövid, dupla Z-szelvényű próbatestek segítségével elemeztem az átlapolás környékének viselkedését nyomó igénybevételre.

A kísérleti eredmények alapján meghatároztam a vizsgált nyomott Z-szelvényű elemek tervezési ellenállását.

2. tézis

Nyomott Z-szelvényű elemek viselkedésének modellezésére felületszerkezeti végeselemes modellt dolgoztam ki. A felületszerkezeti modellen anyagi- és geometriai nemlinearitás figyelembevételével imperfekció érzékenységi vizsgálatsorozatot hajtottam végre. A helyettesítő geometriai imperfekciót a modell sajátalakjai alapján vettem fel és meghatároztam azok hatását a szerkezet viselkedésére: merevség, teherbírás és tönkremeneteli mód. A sajátalakok elemzését kétféleképpen hajtottam végre:

a) Módszert dolgoztam ki a felületszerkezeti végeselemes modell sajátalakjainak osztályozására az alap kihajlási és horpadási alakok geometriai definíciója alapján. A javasolt módszer algoritmusát beépítettem egy vékonyfalú tetőszerkezetek modellezését végző saját fejlesztésű számítógépes programba.
b) Paraméteres vizsgálatsorozatot hajtottam végre vékonyfalú C- és Z-szelvények felületszerkezeti végeselemes modelljének sajátalakjainak osztályozására végessávos bázisfüggvények segítségével. Az osztályozás segítségével meghatároztam a lokális, a torzulásos horpadás és globális kihajlási alakok részarányát különböző megtámasztási viszonyok és hálósűrűség esetén, és bizonyítottam a módszer alkalmazhatóságát.

3. tézis

Megterveztem és végrehajtottam egy kísérleti programot folytatólagos Z-szelemenek különböző komponenseinek vizsgálatára. Az átlapolt kapcsolatot az alábbi speciális szerkezeti kialakításban vizsgáltam: (i) a Z-szelemenek övszélessége azonos, ezért az átlapolást összefeszítéssel kell kialakítani, (ii) a két szelement összekapcsoló csavarok lyukátmérője jelentősen nagyobb a csavarátmérőnél, illetve (iii) az átlapolás közepén a gerincben nincs csavar. Erre a szerkezeti kialakításra meghatároztam a viselkedési módokat és a tervezési teherbírás értékeket az alábbiak szerint:

a) Meghatároztam az átlapolás végének tervezési ellenállását különböző nyomaték és nyíróerő arányok esetén. Az eredmények alapján az átlapolás végének nyomaték és nyíróerő interakciójának számítására Eurocode 3 alapú méretezési eljárást dolgoztam ki.

b) Meghatároztam az átlapolás közepének tervezési ellenállását különböző nyomaték és reakcióerő arányok esetén. Az eredmények alapján igazoltam, hogy az Eurocode 3 szabványos méretezési eljárása alkalmazható az átlapolás közepének méretezésre.
c) Külön vizsgálati programot dolgoztam ki egy szélső támasz feletti Z-szelemen beroppanásának vizsgálatára. A kísérletek alapján meghatároztam a viselkedési módjait és tervezési ellenállás értékeket. Az eredmények alapján javaslatot tettem az Eurocode 3 alapú méretezési eljárás módosítására.

Kidolgoztam az alkalmazott átlapolás csomópont felületszerkezeti végeselemes modelljét és a végrehajtott numerikus vizsgálatokkal jellemeztem az átlapolás végének és a támaszkörnyezet viselkedési módjait.

4. tézis

Megterveztem és végrehajtottam egy kísérleti programot könnyűszerkezetes tetőszerkezetek kiegészítő elemeinek a vizsgálatára. Meghatároztam a vizsgált elemek viselkedési módjait és a tervezési ellenállásait az alábbiak szerint.

a) Hidegen alakított vékonyfalú U-szelvényű szelemenkifüggesztő elem nyomásra és húzásra, kétféle konfigurációban: nagyméretű kivágással a gerincben, illetve kivágás nélkül.
b) Állítható szelemenkifüggesztő elem nyomásra és húzásra, különböző csavarpozíciók esetén.
c) Taréj eleme a szelemenkifüggesztő rendszernek nyomásra és húzásra különböző tetőhajlások esetén.
d) A szelemen kifüggesztő rendszer rúdjai húzásra, szimmetrikus és nem szimmetrikus elrendezésben.

Kidolgoztam a nyomott szelemenkifüggesztő elem felületszerkezeti végeselemes modelljét. Jellemeztem a modell tönkremeneteli módjait és meghatároztam virtuális kísérletekkel a helyettesítő geometriai imperfekcióit.

5. tézis

Kidolgoztam az alapjait és az algoritmusát könnyűszerkezetes tetők összetett méretezési módszerének. A méretezési módszer összekapcsolja a (i) kísérleti alapú ellenállásokat, amelyekhez nincsen szabványos háttér és (ii) az Eurocode 3 alapú imperfekt modellen alapuló nemlineáris szimulációt. A kifejlesztett algoritmus – PurlinFED – három különböző méretezési szintet tartalmaz tetőszerkezetekre vonatkozóan:

a) rúdmodell kiegészítve a kísérleti úton meghatározott átlapolás merevségekkel és a javasolt méretezési eljárásokkal az átlapolás végére és a szélső támaszra vonatkozóan,
b) rúdmodell kiegészítve héj végeselemes alapú stabilitásvizsgálattal, ahol a karcsúságot a teljes tetőszerkezet végeselemes modelljéből határozható meg, ami figyelembe veszi a burkolat valós megtámasztó hatását a szelemenre,
c) héj végeselemes modell, ahol az anyagi és geometriai nemlineáris számítás imperfekt modellen alapul, az imperfekciókat a sajátalakokból származnak, melyeket a beépített osztályozó algoritmus segítségével választhatók ki.

6.2 Application of the results

6.2.1. Direct applications of the results

The different test based design values and interaction curves of the overlapped connection are directly used in the daily design practice of Lindab and Astron companies. The results are built in the purlin design program developed by the team of F. Werner in Bauhaus University

Weimar, Germany. The stiffness characteristics of the overlap zone are also implemented. The test based design values of the various elements of the anti-sag system is also implemented in the Astron design methodology.

6.2.2. Indirect application of the research method

The research methods (experimental test – test based design – nonlinear simulation on shell finite element models) used in my research are also applied on other structural systems in the last years, as follows.

The global stability analysis of the Pentele bridge in Dunaújváros: experimental analyses are carried out on the M=1:34 scale model of the bridge in the Structural Laboratory of the Department of Structural Engineering. Design method of arches for in-plane and out-of plane buckling are verified by the experimental tests. The results are used on beam and shell finite element models of the bridge model and the real bridge. The global stability of the arch in the erection and final stages are designed by the global finite element models of the bridge [67]-[75]. This global model is used to determine the vibration characteristics of the bridge for dynamic calculations (wind and earthquake).

Global shell finite element model is developed for the M0 highway bridge also to check the stress distribution at various locations of the steel deck plate [76].

The test based design values of horizontal bracing system connection to the column base are also determined by nonlinear finite element models [77] for Butler company.

Large numbers of numerical simulations are executed on shell finite element models of steel frames to check existing buildings by advanced design method [78].

6.3 Further research

In general the presented results are parts of the ongoing research on modern roof systems. Regarding the compressed Z-section members the design method and the application of numerical models in the advanced design has to be furthermore studied. The classification of the eigenmodes of compressed members by the cFSM base functions has to be extending to special members with holes, to be able to apply more generally. Further research is needed to develop a method where the base functions comes from the FE method and it can be used for members with variable height and special support conditions, respectively.

Experimental and numerical researchers completed on overlapped connections of continuous purlins for specific structural arrangements. The developed FE model can be the basis of new design method of the overlap zone, which can be implemented in the standard design methodology.

In case of the research of full roof systems the developed algorithm has to be extended to new structural details, and benchmark and parametric studies should be completed to prove the applicability of the design method. After that the advanced design method can be implemented into the design practice and can be applied to improve the structure and optimize purlin-roof systems.

6.4 Main publications on the subject of the thesis

International journal paper: [31]
Papers in edited books: [55]
International conference papers: [25], [26], [28], [30], [54], [56]
Conference papers (abstract and presentation only): [27], [29], [41], [42]
Research reports: [39], [40], [57], [58]

References

Previous Hungarian studies

[1] Csellár, Ö., Halász, O., Réti, V. (1965). "Thin-walled steel structures", *Technical Publisher*. (in Hungarian)

[2] Tomka, P. (1985). "Load capacity of cold-formed Z-sections", *Periodica Polytechnica*, Vol. 29, No. 3-4, 199-208.

[3] Verőci, B. (1986). "Experiments on steel trapezoidal sheets", *Proceedings of the 2nd Regional Colloquium on Stability of Steel Structures*, Tihany, Hungary. II/317-325.

[4] Horváth, L., Verőci, B. (1995). "An advanced method for the design of first generation profiled sheets", *International Colloquium on Stability of Steel Structures*, Hungary, Budapest, Vol. II., 145-152.

[5] Dunai, L. (2007). "Innovative steel and composite structures", *Doctor of Hungarian Academy of Sciences Thesis*.

Z/C thin-walled members in compression

[6] Polyzois, D., Charnvarnichborikarn, P. (1993). "Web-flange interaction in cold-formed steel Z-section columns", *Journal of Structural Engineering*, Vol. 119, No. 9, 2607-2628.

[7] Davies, J.M., Leach, P. (1994). "First-order generalised beam theory", *Journal of Constructional Steel Research*, Vol. 31, 187-220.

[8] Schafer, B.W., Ádány, S. (2006). "Buckling analysis of cold-formed steel members using CUFSM: conventional and constrained finite strip methods", *Eighteens International Specialty Conference on Cold-Formed Steel Structures*, Orlando, USA, 39-54.

[9] Silvestre, N., Camotim, D. (2002). "First-order generalised beam theory for arbitrary orthotropic materials", *Thin-Walled Structures*, Vol. 40 (9), 755-789.

[10] Silvestre, N., Camotim, D. (2002). "Second-order generalised beam theory for arbitrary orthotropic materials", *Thin-Walled Structures*, Vol. 40 (9), 791-820.

[11] Silvestre, N., Camotim, D. (2004). "Distortional buckling formulae for cold-formed steel C and Z-section members Part I – derivation", *Thin-Walled Structures*, Vol. 42, 1567-1597.

[12] Silvestre, N., Camotim, D. (2004). "Distortional buckling formulae for cold-formed steel C and Z-section members: part II – validation and application", *Thin-Walled Structures*, Vol. 42, 1599-1629.

[13] Ádány, S., Schafer, B.W. (2006). "Buckling mode decomposition of single-branched open cross-section members via finite strip method: Derivation", *Thin-Walled Structures*, Vol. 44, 563-584.

[14] Ádány, S., Schafer, B.W. (2006). "Buckling mode decomposition of single-branched open cross-section members via finite strip method: Application and examples", *Thin-Walled Structures*, Vol. 44, 585-600.

[15] Ádány, S., Schafer, B.W. (2008). "A full modal decomposition of thin-walled, single-branched open cross-section members via the constrained finite strip method", *Journal of Constructional Steel Research*, Vol. 64, 12-29.

[16] Ádány, S. (2004). "Buckling mode classification of members with open thin-walled cross-sections by using the Finite Strip Method", *Research Report*, Johns Hopkins University, (available at http://www.ce.jhu.edu/bschafer)

[17] Bakker, M.C.M., Peköz, T. (2003). “The finite element method for thin-walled members – basic principles”, *Thin-Walled Structures*, Vol. 41, 179-189.
[18] Schafer, B.W., Peköz, T. (1998). “Computational modeling of cold-formed steel: characterizing geometric imperfections and residual stresses”, *Journal of Constructional Steel Research*, Vol. 47, 193-210.
[19] Garstecki, A., Kakol, W., Rzeszut, K. (2002). “Classification of local-sectional geometric imperfections of steel thin-walled cold-formed sigma members”, *Foundations of Civil and Environmental Engineering*, Vol. 1, 87-96.
[20] Dubina, D., Ungureanu, V., Szabo, I. (2001). “Codification of imperfections for advanced finite analysis of cold-formed steel members”, *Third International Conference on Thin-Walled Structures*, Cracow, Poland, 179-186.
[21] Nagahama, K., Camotim, D., Batista, E. (2002). “Local buckling, post-buckling and mode interaction finite element analysis in cold-formed steel members”, *Sixth International Conference on Computational Structures Technology*, Prague, Czech Republic, Paper No. 99, 235-236.
[22] Schafer, B.W., (2006). “Review: The Direct Strength Method of Cold-formed Steel Member Design”, *International Colloquium on Stability and Ductility of Steel Structures*, Lisbon, Portugal, Vol I. 49-66.
[23] Dunai, L., Joó, A.L., Jakab, G. (2002). “Lindab-OM research report BME_8IIb”, *Research report*, Department of Structural Engineering Budapest University of Technology and Economics
[24] Lendvai, A. (2004). “Optimization of thin-walled cold-formed hat section”, Diploma work (in Hungarian)
[25] Dunai, L., Jakab, G., Joó, A.L. (2004). “Experiments on C/Z-profile compression members”, *Fourth International Conference on Coupled Instabilities in Metal Structures*, Rome, Italy, 429-438.
[26] Joó, A.L., Dunai, L. (2004). “Geometric imperfections of Z-profiles for numerical models”, *Fourth International Conference on Coupled Instabilities in Metal Structures*, Rome, Italy, 97-106.
[27] Joó, A.L., Dunai, L. (2003). “Geometric imperfections of thin-walled Z-members”, *Ninth National Conference on Applied Mechanics*, Miskolc, Hungary, 27-29. (in Hungarian)
[28] Ádány, S., Joó, A.L., Schafer, B.W. (2006). “Approximate identification of the buckling modes of thin-walled columns by using the CFSM modal base functions”, *International Colloquium on Stability and Ductility of Steel Structures*, Lisbon, Portugal, 197-204.
[29] Joó, A.L., Ádány, S. (2007). “Classification of buckling modes of thin-walled compressed columns by finite strip base functions”, *Tenth National Conference on Applied Mechanics*, Miskolc, Hungary. (in Hungarian)
[30] Ádány, S., Joó, A.L., Schafer, B.W. (2008). “Identification of FEM buckling modes of thin-walled columns by using CFSM base functions”, *Fifth International Conference on Coupled Instabilities in Metal Structures*, Sydney, Australia, 265-272.
[31] Joó, A.L., Ádány, S., (2009). “FEM-based approach for the stability design of thin-walled members by using cFSM base functions”, Periodica Polytechnica (accepted for publication).

Continuous purlins

[32] Yu, C., Schafer, B.W. (2007). "Simulation of cold-formed steel beams in local and distortional buckling with applications to the direct strength method", *Journal of Constructional Steel Research*, Vol. 63, 581-590.

[33] Yong-Lin, P., Put, B.M., Trahair, N.S. (1999). "Lateral buckling strengths of cold-formed Z-section beams", *Thin-Walled Structures*, Vol. 34, 65-93.

[34] Ho, H.C., Chung, K.F. (2006). "Structural behaviour of lapped cold-formed steel Z sections with generic bolted configurations", *Thin-Walled Structures*, Vol. 44, 466-480.

[35] Zhang, L., Tong, G. (2007). "Moment resistance and flexural rigidity of lapped connections in multi-span cold-formed Z purlin system", *Thin-Walled Structures*, doi:10.1016/j.tws.2007.10.010.

[36] Chung, K.F., Ho, H.C., Wang, A,J. (2005). "An investigation into deformation characteristics of lapped connections between cold-formed steel Z sections", *International Journal of Steel Structures*, Vol. 5, No. 1, 23-32.

[37] Ho, H.C., Chung, K.F. (2006). "Analytical prediction on deformation characteristic of lapped connections between cold-formed steel Z sections", *Thin-Walled Structures*, Vol. 44, 115-130.

[38] Ádány, S., Yu, C., Schafer, B.W. (2005). "Local and distortional buckling resistance of cold-formed steel beams: EC3 in the light of (i) experimental research and (ii) other design codes", *Fourth European Conference on Steel and Composite Structures*, Maastricht, The Netherlands, 1.2-109 – 1.2-116.

[39] Dunai, L., Joó, A.L., Kaltenbach, L., Kálló, M., Kachichian, M., Tóth, A., Futó, T. (2007). "Astron purlin tests – Experimental study", *Research report*, Department of Structural Engineering, BME, p. 193.

[40] Dunai, L., Joó, A.L., Ádány, S., Futó, T. (2007). "Astron purlin tests – Comparative study of test results", *Research report*, Department of Structural Engineering, BME, p. 19.

[41] Joó, A.L. (2007). "Numerical modeling of Z-purlin overlapped connection", *Sixteenth Inter-Institute Seminar for Young Researchers*, Vienna, Austria, p. 22.

[42] Joó, A.L., Dunai, L. (2007). "Experimental analysis of Z-purlin overlapped connection", *Twenty-fourth Danubia-Adria Symposium on Developments in Experimental Mechanics*, Sibiu, Romania, 169-170.

Roof systems

[43] Heinz, D.A. (1994). "Application of generalized beam theory to the design of thin-walled purlins", *Thin-Walled Structures*, Vol. 19, 311-335.

[44] Chung, K.F., Quinton, D.St. (1996). "Structural performance of modern roofs with thick over-purlin insulation – experimental investigation", *Journal of Constructional Steel Research*, Vol. 40, No. 1, 17-38.

[45] Curávy, T. (2007). "Experimental and numerical analysis of sag channels", Student Scientific Conference, BME (supervisor: Joó, A. L.), (in Hungarian).

[46] Kachichian, M., Dunai, L. (2001). "Experimental study on the lateral stiffness of sliding connection of purlin-cladding system", *Scientific Publications of the Department of Structural Engineering, BME*, 77-82.

[47] Kachichian, M., Dunai, L., Kaltenbach, L., Kálló, M. (1999). "Experimental study on the interaction of steel sheeting and Z-purlin", *Sixth International Colloquium on Stability and Ductility of Steel Structures*, Timisoara, Romania, Eds. Dubina, D., Iványi, M., Elsevier Publisher, 509-516.

[48] Laine, M., Tuomala, M. (1999). “Testing and design of gravity-loaded steel purlins restrained by sheeting”, *Journal of Constructional Steel Research*, Vol. 49, 129-138.
[49] Lucas, R.M., Al-Bermani, F.G.A., Kitipornchai, S. (1997). “Modeling of cold-formed purlin-sheeting systems – Part 1: Full model”, *Thin-Walled Structures*, Vol. 27, No. 3, 223-243.
[50] Lucas, R.M., Al-Bermani, F.G.A., Kitipornchai, S. (1997). “Modeling of cold-formed purlin-sheeting systems – Part 2: Simplified model”, *Thin-Walled Structures*, Vol. 27, No. 4, 263-286.
[51] Sokol, L. (1996). “Stability of cold formed purlins braced by steel sheeting”, *Thin-Walled Structures*, Vol. 25, No. 4, 247-268.
[52] Jiang, C., Davies, J.M. (1997). “Design of thin-walled purlins for distortional buckling”, *Thin-Walled Structures*, Vol. 29, No. 1-4, 189-202.
[53] Vraný, T. (2006). “Effect of loading on the rotational restraint of cold-formed purlins”, *Thin-Walled Structures*, Vol. 44, No. 12, 1287-1292.
[54] Joó, A.L., Dunai, L. (2002). “Numerical studies on the ultimate behaviour of steel cold-formed purlins”, *Sixth International Conference on Computational Structures Technology*, Prague, Czech Republic, “Computational Steel Structures Technology”, Eds. Topping, B.H.V., Bittnar, Z., Civil-Comp Press, 247-248 (on CD-ROM: ISBN 0-948749-81-4, 14 pages).
[55] Joó, A. L., Kachichian, M., Dunai, L. (2002). “Experimental and numerical analysis of Z-purlins”, *Scientific Publications of the Department of Structural Engineering, BME*, 55-64. (in Hungarian)
[56] Joó, A. L., Ádány, S., Dunai, L. (2002). “On the Eurocode 3 design method of cold-formed Z-purlins”, *Third European Conference on Steel Structures*, Coimbra, Portugal, 625-634.
[57] Joó, A.L., Dunai, L., Kaltenbach, L., Kálló, M., Kachichian, M., Curávy, T. (2007). “Astron sag channel tests – Experimental study”, *Research report*, Department of Structural Engineering, BME, p. 19.
[58] Joó, A.L., Dunai, L., Kaltenbach, L., Kálló, M., Kachichian, M., Curávy, T. (2007). “Astron flying sag system tests – Experimental study”, *Research report*, Department of Structural Engineering, BME, p. 41.

Standards

[59] EN 1993-1-1 (2004). *Eurocode 3: Design of steel structures – Part 1-1: General rules and rules for buildings.*
[60] EN 1993-1-3 (2005). *Eurocode 3: Design of steel structures – Part 1-3: General rules. Supplementary rules for cold-formed members and sheeting.*
[61] EN 1993-1-5 (2005). *Eurocode 3: Design of steel structures – Part 1-5: Plated structural elements.*
[62] American Iron and Steel Institute (1996). *AISI Specification for the Design of Cold-Formed Steel Structural Members.* American Iron and Steel Institute. Washington, D.C.
[63] Standards Australia (1996). *Cold-formed steel structures. AS/NZS 4600:1996.* Australia.

Computer programs

[64] ANSYS Release 6.0, Rainbow Technologies, Inc. (2002). *Ansys 6.0 Online Documentation*.

[65] Matlab Version 6.1.0.450 Release 12.1 (2002). The MathWorks, Inc., *Matlab Online Documentation*.
[66] CUFSM: Elastic Buckling Analysis of Thin-Walled Members by Finite Strip Analysis; CUFSM v3.12, 2006. http://www.ce.jhu.edu/bschafer/cufsm

Other publications of the Author

[67] Honfi, D., Joó, A.L., Dunai, L., Ádány, S. (2005). "Parametric study on the structural versions of the Danube bridge in Dunaújváros", *Scientific Publications of the Department of Structural Engineering*, BME, 9-18. (in Hungarian)
[68] Joó, A.L., Dunai, L. (2005). "Strength of an arch bridge model: experiment and design methods", *Fourth European Conference on Steel and Composite Structures*, Maastricht, The Netherlands, Eds. Hoffmeister, B., Hechler, O., Druck und Verlaghaus Mainz Publisher, Vol. B, 4.7-49 – 4.7-56.
[69] Joó, A.L., Dunai, L., Kálló, M., Kaltenbach, L., Köröndi, L. (2005). "Experimental analysis of a Nielsen-type bridge model", *Materials Engineering*, Vol. 12, No. 1, 1-6.
[70] Mihálffy, A., Joó, A.L., Dunai, L., Szatmári, I. (2005). "Fatigue analysis of orthotropic bridge decks", *Scientific Publications of the Department of Structural Engineering, BME*, 65-76. (in Hungarian)
[71] Joó, A.L., Dunai, L., Kálló, M., Kaltenbach, L., Köröndi, L. (2005). "Experimental analysis of the model of the Dunaújváros Danube bridge", *Scientific Publications of the Department of Structural Engineering*, BME, 19-30. (in Hungarian)
[72] Dunai, L., Joó, A.L. (2004). "Ultimate behaviour of arch-bridge model: results of experimental, numerical and design analysis", *Scientific Publications of the Department of Structural Engineering*, BME, 31-40. (in Hungarian)
[73] Joó, A.L., Hegedűs, I. (2004). "Vibration analysis of the Dunaújváros Danube bridge", *Scientific Publications of the Department of Structural Engineering*, BME, 57-64. (in Hungarian)
[74] Dunai, L., Joó, A.L., Kaltenbach, L., Kálló, M. (2004). "Model test of a new Nielsen-type Danube bridge", *Fifth International Conference on Bridges Across the Danube*, Novi-Sad, Serbia & Montenegro, 351-360.
[75] Joó, A.L., Dunai, L., Kálló, M., Kaltenbach, L., Köröndi, L. (2004). "Experimental analysis of a Nielsen-type bridge model", Twenty-first Danubia-Adria Symposium, Pula/Brijun, Croatia, 30-31.
[76] Jakab, G., Joó, A.L., Dunai. L. (2004). "Stress analysis of the main girder of the M0 highway bridge", *Scientific Publications of the Department of Structural Engineering*, BME, 103-112. (in Hungarian)
[77] Joó, A.L. (2002). "Numerical analysis of steel bracing and main-frame connections", *Fourth International Ph.D. Symposium in Civil Engineering*, Munich, Germany, 299-304.
[78] Dunai, L., Joó, A.L., Kovács, D., Futó, T. (2006). "Resistance of Astron frames by FE simulation - Technical background documentation", *Research report*, Department of Structural Engineering, BME, p. 17 + p. 370 appendix.